Alma Mater Studiorum – Università di Bologna

---

Corso di dottorato in
ingegneria Biomedica, Elettrica e dei sistemi

**Settore scientifico disciplinare: ING-IND/31**

# DESIGN OF SUPERCONDUCTING MAGNETS FOR POWER APPLICATIONS

**Candidato:** Umberto Melaccio

**Coordinatore Ph.D.** Prof. Michele Monaci

**Supervisore** Prof. Antonio Morandi

---

XXXIII - 2021

## Acknowledgment

I like to remember that science has weird ways to create gratification for who lives for it, apparently methodical individuals working without knowing who will take benefit of their work. But still from the inside it appears as an organic machine in which every single part moves to reach step by step with passion something new. This period has been useful for me to know all the these people collaborate for the same purpose.

First of all, I want to thank Prof. Antonio Morandi to mentor me in this path, always supporting me in the difficult periods and pushing me to do better and allowing me to experience the better out of this phase of my life. All around in my department I see Prof. Pierluigi Ribani, with who I've always great and stimulating conversation, his wisdom is always available for who seeks a tip and my office mates Andrea Musso and Arturo Popoli with who I've shared most part of the time in this place in between fun and duty, lunches and meetings.

The idea to start this PhD came out of my internship at Frascati, as a small work among the big projects they were dealing with. So, I want to thank Simonetta Turtù and Alessandro Anemona and the people of the superconductivity group at ENEA, which represents the best well assorted group of researchers I've met, always ready to welcome me and give me a small desk to work.

Furthermore, the second part of the thesis is based on my activities during the abroad period of the last year, made possible by Prof. Minwon Park, Dao Ban Quon, Din Min Chao and all the guys of the CAPTA at Changwon University, that made me part of their life coming out the other part of the world. The period in South Korea made me growing fast, facing a new world with new work prospective and life attitude, with my great friend Ryan Nord who made possible to create the best memories I have about this period.

It is really important to thank my father, my mother who keep me motivated to stay focused on my goals; I am going to translate all I wrote for them. And my brother, it does not matter where my place will be, there always will be.
Living in Bologna gave me the opportunity to know a long list of amazing people. There are so many that I could fill a separate book with names, all my friends and flatmates who made me think to the place where I lived as my home and a special place is for my second family, the Pretenders, with who I have shared all my laughter and tears of the last three years with a peculiar bond with each of them.

## Abstract

A three-year research project, called DRYSMES4GRID, was recently funded by the Italian Minister of Economic Development, Italy. The project is aimed to demonstrate the feasibility of cost-competitive SMES based on magnesium diboride ($MgB_2$) with a cryogen-free cooling by means of the manufacturing and the testing of a demonstrator with an objective rating of 500 kJ/200 kW. This rating is deemed suitable for disclosing the critical technological aspects of all components in view of practical applications. Both the developed methodology and the design results are reported in detail. The preliminary design, concerning the definition the geometry of the coil and the reference $MgB_2$ conductor based on the functional requirements of the system (stored energy and deliverable power), is first discussed. The detailed design of the coil, aimed at producing the information and the technical drawings needed for the manufacturing of the coil, is then presented. Assumptions concerning the general layout, support material and electrical insulation are described. The mechanical behavior of the coil during cool down and successive energization up to the nominal transport current is analyzed and the compatibility of stress and strain with allowable limits of the conductor is verified. Distribution of electrical stress on the coil during the switching of the power electronic converters is also calculated for the proper design of electrical insulation. Modelling assumptions, as well as material properties used for the calculation, are reported. Results of quench analysis are also presented showing that the maximum hot spot temperature reached when the coil is discharged is within the design value. Evaluation of the thermal load due to radiation, conduction through the supports, current leads and AC loss is presented. Attention is devoted at explaining the assumptions and the criteria used of the calculation of the AC loss during charge/discharge operation of the SMES coil at actual power rate. Thermal analysis is finally carried out both in steady state condition (SMES operating at the nominal DC current) and in dynamic condition (charge and discharge of the SMES) for calculating the distribution of temperature all over the coil. Thermal fluxes are calculated and their compatibility with the capacity map of the cryo-coolers is checked.

The same methodology has been applied on another superconducting application in order to design the SC coil of a Saturated Iron superconductive Fault Current Limiter (SI-SFCL) at Changwon National university, South Korea. The SI-SFCL consists of three main parts: one magnetic iron-core, one normal conductive primary coil (CPC), and one superconducting secondary coil (SSC). This paper thesis also deals with the design options for the coil system of the SI-SFCL and confirms their operating characteristics through a numerical approach. A 3D finite element method model was built to analyze the electromagnetic characteristics and operational features of the SI-SFCL. The design of the SSC was based on the terms of shape, wire types, required fault current limit and protection aspects. The bobbin was designed based on material selection, cost, structural design, and the effects of the SI-SFCL on the fault current limit.

The results obtained through this study can be applied to large-scale SI-SFCL development studies for HVDC power systems.

# Contents

## List of figures

# 1 Superconductors in the Power Grid

This chapter gives a comprehensive description of the ways in which superconductors can impact—and are impacting—the electric power grid.
Also gives an overview of the electric power grid, the major challenges it faces in the future, and its major components: overhead lines, underground cables, transformers, electric generators, reactive compensators, voltage regulators, circuit
breakers, and fault current limiters. It describes briefly the status and prospects for superconductor power equipment: alternating and direct current cables, fault current limiters, transformers, rotating machinery, and superconductor magnetic
energy storage. Overall, although challenges related to cost, reliability, standardization, and utility industry acceptance remain, prospects for broad commercialization of superconductor power grid technology are increasingly promising.

## 1.1 Introduction

The electric power grid can be conceived as a network of impedances interrupted by circuit breakers and switches. Material devices like power lines, cables, transformers, and rotating machines can be modelled with an equivalent circuit made of these basic elements. The ambition to make this network smart calls for the introduction of modern sensor and communication technology to manage bidirectional flows of electricity and information, tracking the grid operation and the current flow. New devices are being introduced to provide such control, and superconductors can play a major role.
Most of the grid is designed to carry alternating current (AC) power, with voltage and current that oscillate sinusoidally at 60 Hz in the United States and 50 Hz in Europe and which are conventionally described in terms of the root-mean-square (rms) voltage and current. A linear load in the circuit does not change the shape of the waveforms but changes the relative timing between voltage and current (*phase)* due to its inductance or capacitance. The power factor of an AC power system is defined as the ratio of the real power absorbed by the load to the apparent power flowing in the circuit and is a dimensionless number between -1 and 1. The complex power $S$ is the product of rms voltage $V$ times rms current $I$ and its magnitude is the apparent power. The real power or active power $P$ is expressed in watts (W) and its magnitude is expressed as the product of the apparent power and the cosine of the power factor. The power is delivered in three phases, each separated by one-third of a cycle. Most AC electric power in the United States is generated at rms voltages up to about 22 kV by electric generators, is then “stepped up” to rms voltages of 138 kV, 345 kV, or higher for transmission across long distances, then “stepped down” to lower voltages for local distribution until finally it can be safely used in the factory, or in the home at rms 120 or 208 V. we call rms voltages below about 1 kV low voltage (LV), rms voltages between 1 and 35 kV are medium voltage, rms voltages

from 35 to 66 kV are sub-transmission voltage rms voltages from 66 to 345 kV are high voltage. [1]
All the concepts of the electric power grid and its components were developed by the end of the of the nineteenth century, using conventional copper and aluminum wires coupled with magnetic iron alloys in transformers and generators. Utilities have always faced many challenges such as maintaining reliable service while matching generating capacity and changing loads, trying to avoid power system disruptions, adapting to a changing mix of energy sources and coordinating independent power producers. But new challenges are coming out which require more than just a growth in the grid [2]:

- *Load growth and siting barriers*, demand for electric power has been estimated increasing more than 20% in 2035, and possible massive electric vehicle could rise these numbers. The growth is concentrated in the urban areas so that becomes difficult to address all the needed power. this challenge can be met by superconductor technology, also considering that much of the transmission and distribution infrastructure in grids are going to end their useful specified design life and will need to be replace.
- *Environmental and safety issues*, the increasing attention to pollution and climate change creates an opportunity for superconductor power equipment if it could be designed to be sufficiently efficient. The problem of use of flammable oil as coolant especially in transformers with the high risk of oil leak contamination, fire, and explosion is another real challenge. Superconductor devices cooled by liquid nitrogen, eliminates this problem. Furthermore, renewable energy sources far from the major loads require more efficient distance transmission of power such as direct current (DC) superconductor cables. One special renewable energy challenge arises in offshore wind power. Offshore wind is typically stronger and steadier than on land, providing a potentially huge and reliable new source for clean renewable energy. Higher power ratings, in the range of 10MW or more could reduce construction costs and maintenance, and this solution can be achieved with compact superconductor generators.
- *Reliability and power quality*. The increasing dependence on microprocessor control makes the grid more sensitive to glitches of even microsecond duration. The current faults from short circuits in the grid also increase in urban grids. Superconductor fault current limiters (SFCLs) can address this problem.

The key for the penetration of superconductor equipment is the higher performance it offers, inaccessible to conventional technology but another challenge is making them cost competitive as well.

## 1.2 Superconductors in magnet

Superconductivity is a phenomenon that causes the electrical resistance in certain materials to reduce to zero, below a certain critical temperature $T_c$. This allows for a high density of resistanceless current to flow inside the coil windings. Superconductors can be divided into two groups: type-I and type-II. The two groups distinguish themselves in their behavior in

magnetic field. When a magnetic field is applied to a type-I superconductor below the critical temperature it generates a current on its surface to fully shield the magnetic field. This phenomenon is called the Meissner-Ochsenveld effect. When the magnetic field is increased further, beyond the critical field $B_c$ the currents are no longer able to shield the magnetic field causing the material to lose superconductivity.

In a type-II superconductor, however, beyond the first critical field $B_{c1}$ (much lower than $B_c$ in type-I) the magnetic field is allowed to penetrate the material through so-called vortices. This phenomenon is called the Abrikosov effect. The resulting mixed state, with normal conductivity inside the vortices surrounded by material in the superconducting state, is stable and thus allows superconductivity to be maintained up to very high upper critical magnetic fields, making type-II superconductors crucial for practical applications. It is energetically favorable for the vortices in a type-II superconductor to be located on micro-structural defects in the material, an effect called flux pinning. The critical current density is interdependent with both magnetic field and temperature.

The type-II superconductors are subdivided further into LTS and HTS, based on whether or not their critical temperature exceeds the boiling point of liquid nitrogen temperature. In magnet applications superconductors are always paired with a good resistive conductor that can temporarily take over the current under fault conditions. The most common LTS conductor is the alloy Niobium-Titanium (Nb-Ti) which is a ductile superconductor and widely used for practical applications. The critical temperature is 9.2 K and the upper critical field is 14.2 T at absolute zero temperature. In higher magnetic field application, the triniobium-tin ($Nb_3$-Sn) is used, with a critical magnetic field of 30 T and a critical temperature of 18.3 K. This is a brittle compound, so it is necessary to wind the magnet first and than react in a furnace. The HTS have very different characteristics and at present there are two available types: *Bismuth Strontium Calcium Copper Oxide (BSCCO)* which has a critical temperature of 95 K and upper critical field of about 200 T and *Rare earth Barium Copper Oxide (YBCO)* which has a critical temperature of 93 K and an upper critical field of about 168 T. Both require a complex and very challenging manufacturing techniques.

The $MgB_2$ takes place, depending on its critical temperature, in between LTS and HTS. Its critical temperature is 39 K, so that the choose of this material is generally connected to its physical properties (critical temperature, field and current) but also to its mechanical properties (resistance to mechanical stress and deformability). Another relevant factor is the cost of the material and the possibility to operate without cryogenic liquids.

## 1.3 Elements of electric power grid

### 1.3.1 Overhead lines and underground cables

The main elements of the electric power grid are the long-distance links, overhead or underground. These cables consist of long conductors arranged in an appropriate configuration to handle the voltage, current and mechanical stress. Overhead lines, with aluminum wires suspended from wooden or metal towers are more common. Their cost is low so that will be tough for superconductor links to replace them[1].
Underground cables consist of a central conductor made of multiple cooper wires surrounded by a high voltage dielectric and a second cylindrical coaxial conductor wound helically.
The conventional technologies are the most used but with the increasing power demand, further improvements are needed, as detailed here:

- *Higher efficiency*, about 8% of annual average power is lost in wasteful resistive heating between generation and loads. Superconductors offer a way to lower losses and reduce the environmental impact.
- *Voltage reduction*, because safety issue is desirable to decrease the voltage but at a given power, decreasing voltage corresponds to increasing current which is possible with superconductors.

AC cable are very advanced HTS grid application, similar to conventional underground cables, they assemblies of multiple HTS wires surrounded by layers of high voltage dielectric, a screen of HTS wires, a cryostat and an external jacket. Cooled by liquid nitrogen pumped from a closed cycle refrigeration system at one or both of the cable ends, they have sophisticated high-voltage terminals where the transition is made from superconductor wires to copper leads, and also from liquid nitrogen to room temperature. The superconductor cables present many advantages over conventional ones, such as:

- *Power capacity*, thanks to the high current carrying capacity of superconductor wires, typically 2 - 4 kA.
- *Ease of installation*, the screening layer eliminate emf which could disturb nearby communication cables. They can be placed clos to other cables without interference.
- *Fault current limitation*, another important option in HTS cable design is to introduce fault current limiting functionality directly into the cable. This is particularly valuable, enabling substation-to-substation links at distribution voltage in urban environments where fault currents are already nearing their acceptable limit. Without the limiting feature, such links would reduce the grid's residual impedance and dangerously increase the magnitude of fault currents.

- *Low impedance*, Low inductive impedance of HTS cables originates from their compactness and tight containment of magnetic field in the narrow shell between the inner conductor and the screening layer. When such cables lie in parallel with conventional cables in a grid, they will take on more load and unload an otherwise overloaded conventional circuit. This allows the current flows to be much finer controlled.

### 1.3.2 Power transformers

Transformers are static devices that transfer electrical energy from one circuit to another by the phenomenon of electromagnetic induction without any change in frequency. They can link circuits that have different voltages, which is one of the enabling factors for the universal use of the alternating current (AC) system for the transmission and distribution of electrical energy. Hence, transformers ensure that various components of the power system, viz. generators, transmission lines, distribution networks and loads, can all be operated at their most suitable voltage levels. As transmission voltages are increased to higher levels in some parts of a power system, transformers again play a key role in interconnecting the different parts of the system at different voltage levels. Transformers are therefore vital links between the generating stations and the points of utilization in any system.

The transformer is an electromagnetic conversion device in which the electrical energy received by its primary winding is first converted into magnetic energy, which is re-converted into electrical energy in other circuits (secondary winding, tertiary winding, etc.). Thus, the primary and secondary windings are not connected electrically, but coupled magnetically. A transformer is termed either a step-up or a step-down transformer depending upon whether the secondary voltage is higher or lower than the primary voltage. Transformers can be used to either step-up or step-down voltage depending upon the need and application; hence, their windings are referred as high-voltage/low-voltage or high-tension/low-tension windings instead of primary/secondary windings. A transformer operates based on the principle of electromagnetic induction (Faraday's law). In a typical core-type transformer, two solenoidal coils, called the primary and secondary, separated by a dielectric insulator, are wound coaxially around a yoke consisting of a soft (easily magnetized) magnetic material, such as iron. An AC rms current $I_{1,rms}$ and voltage $V_{1,rms}$ in the primary are then transformed to an AC current $I_{2,rms}$ at voltage $V_{2,rms}$ in the secondary, with the voltages in proportion to the ratio of turns in the primary and secondary coils. Total power P is conserved except for small resistive and magnetic losses; thus, current is reduced as voltage is increased and vice versa.

Large power transformers that convert between transmission and distribution voltages are located in carefully protected and enclosed substations, along with the related switchgear, and reactive compensation, which control grid operation. Substations are the key nodes in the electric power grid. Because current in a link with resistance *R* generates Joule heating loss $I^2R$ and *R* increases in proportion to distance, long-distance transport of power with high current can be highly inefficient. By using transformers to convert AC power to high

voltage and low current for long-distance transport and then to transform the power back to lower voltage and higher current for local use more efficient power transport is achieved. With the introduction of superconductors the wire resistance is brought near to zero so that much higher currents can be tolerated in long distance low voltage links. Furthermore, the superconductors used for transformers can have some advantages:

- *Reducing AC losses*, is not so easy to reduced losses below the conventional transformers level highly optimized. In cables, the dominant AC magnetic fields generated by the currents are parallel to the surface of the helically wound tapes, which helps keep losses to a minimum, while the magnetic fields near the ends of transformer coils are directed perpendicular to the tape surface, generating large losses that rise in proportion to the width of the tape. Many attempts have been done in order to reduce the AC losses [3]-[5].
- *Compactness and low inductance*, the high-power density, thanks to the high wire current density can allow a reduction of volume. It leads also to lower inductance depending on the volume.
- *Fault current limiting*, it is possible to introduce current limiting functionality directly within the transformer with a major cost advantage.

### 1.3.3 Electric generator

Another important element in the power grid is the electric generator. It produces electrical energy converting mechanical energy from the rotation of a rotor which can be driven by different energy sources, such as turbine, combustion of fuels, hydropower and wind power. Typically, rotating permanent magnets or coils generate a rotating magnetic field that induces a voltage in the stator connected to the grid.

The main goal about this technology is to improve its efficiency; given the amount of energy that it produces, even a small percentage of improvement can be a significant saving. Also the reduction of the dimensions could have a major impact especially in offshore wind turbine generators and in the field of transportation.[6]

Large generators can be really advantageous as HTS application as well as dynamic synchronous condenser: these are generators without power source but which can supply reactive power for mitigation of voltage dips and sags in the grid. The usual design of HTS rotating machinery considers a rotor with HTS coils and a stator with conventional copper coils connected to the grid. This configuration presents some advantages:

- *Enhanced efficiency*, because the rotor coils operates essentially DC, their AC losses are low and can be handled with small cryo-cooler like Gifford-McMahon refrigerator coupled with a gaseous helium loop.
- *Reduced size and weight*, as previously discussed, high HTS wire current density enables more compact designs. In shipboard and other transportation environments, these advantages are obviously important, but they are also valuable in small generation stations.
- *Reduced vibration and noise*, the smaller size eliminates the torques during the change of direction of the magnetic field.

### 1.3.4 Circuit breakers and FCLs

Under the normal operating conditions in the grid, the current *I* is determined by the generalized Ohm's law or Kirchoff's equation, $I=V/(R+jX)$ where *V* is the voltage , *R* is the resistance and *X* is the impedance. For efficient operation the grid impedance is kept small compared to the resistance. However, if the load impedance is short-circuited the grid current can increases drastically in a current fault event. Where the value of current is about *1 kA*, a fault current can reach tens of thousands of amperes, burning out grid equipment. Circuit breakers, and the switchgear in which they are packaged, are an essential element of the grid; they are necessary to stop fault currents, as well as to isolate segments for repair or service and to introduce new installations [7]. The problem is that as the grid grows, its net impedance decreases, and so the effective fault current increases. An FCL is needed to introduce a large inductance instantaneously when the current becomes too high.

### 1.3.5 Electric energy storage

With the increasing introduction of intermitting renewable energy sources such as solar and wind power, the need of energy storage is increasing. So far, the main energy storage techniques have converted electrical energy in potential energy (pumped hydro storage), high pressure (compressed gas storage), or chemical energy (batteries). More direct means of electrical energy storage are in capacitor and super capacitor banks, or in the magnetic field of a coil.

*SMES (*superconducting magnet energy storage) development is mainly focused on application requiring injections of real power and controlling frequency oscillations. Here the high critical and irreversibility fields of HTS materials offer a distinct advantage.

## 1.4 Superconducting magnet energy storage (SMES)

There are two main ways to store electric energy: capacitor (or super capacitor) and inductors. The electric components have generally inductance which is function of geometry and magnetic permeability. An inductor is made from a coil , but a simple wire can also have inductance, and it represents an indication of the object ability to store energy. The inductance is the tendency of an electric conductor to oppose a change in the electric current flowing through it measured in Henry and provides a simple method of calculating voltage when the current changes according to the equation:

$$V = L\frac{dI}{dt} \qquad (0.1)$$

The store energy is given by:

$$E = {}^{1}/_{2}\, LI^{2} \qquad (0.2)$$

It can be seen from the above equation that the energy stored is a function of the square of the current it also follows that in order to store large amounts of energy it is an advantage to have high currents. While the energy is stored there are losses in the conductor given by:

$$Q = RI^{2} \qquad (0.3)$$

Where R is the electrical resistance. Since the current is high in order to store energy the resistance must be as low as possible. Superconductors satisfy both the requirements. Not only can carry high currents but, for DC currents, it has no intrinsic resistance. SMES are magnet in which the energy is stored in form of magnetic field, which is maintained by current that flow ideally persistently.

These devices can provide high power density in the range of 10 - $10x10^{5}$ kW/kg but unfortunately the specific energy density is very low. It is not possible to simply raise the *B* magnetic field to increase the store energy indefinitely; In the first place the critical current ($I_c$) of the superconductive wire is function of *B* and reduces as *B* increases. Furthermore, another limiting factor is the stress experienced by the superconductor itself, caused by the magnetic pressure. This pressure causes a stress in azimuthal direction (hoop stress) which in each turn places a tensile stress, influencing the performance of the wire.

A complete SMES system comprises three primary subsystems: (1) the superconducting coil and its corresponding support structure, (2) the Power Condition Systems (PCS), which is used to transfer the AC line power source back and forth to the superconducting storage magnet, and (3) the cryogenic refrigeration system that is used to initially cool and ultimately maintain the superconducting magnet at its operating temperature.

This technology is applicable to power quality rather than energy storage; the specific power which is due to rapid discharge can be as high as 20 MW/kg [8].

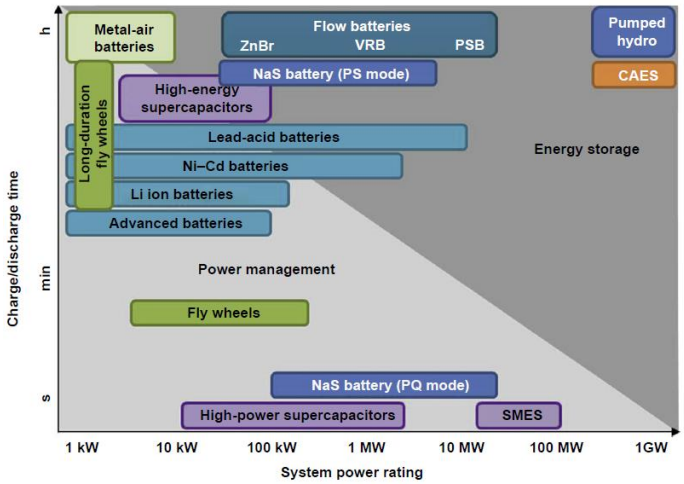


Fig. 0.1 Power/energy range of electric devices

As shown in the Fig. 0.1 SMES can be used for power quality and bridging power, preventing voltage sags. Also, the typical power is of the order of tens of megawatt, making SMES ideal for load levelling in power critical application. It is ideal also for stationary application where high power is required for short time, such as UPS and power quality management.

### 1.4.1 Power electronics converter for SMES

The types of inverter commonly used for the power conversion unit between SMES and AC power system are:

- Current- source inverter (CSI);
- Voltage-source inverter (VS);

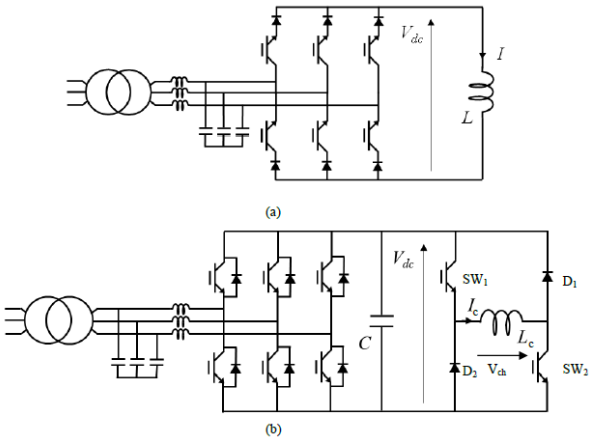


Fig. 0.2 basic concepts of inverter

basic schemes of these inverters are represented in Fig. 0.2. it seems that a CSI is more appropriate for this application since SMES is also a current source. But, there are applications where VSI can improve the effectiveness and capability of the overall system [9].

#### 1.4.1.1 Current-source inverter

A CSI consists of a power electronics block with a large inductance on the DC side, and a capacitor on the AC side. While the inductor maintains constant DC current, AC capacitors provide a stiff AC bus for supplying the fast-changing current pulses needed for commutations. The DC current is maintained in one direction, and the power direction can changed by reversing DC voltage.

By this configuration, independent control of real and reactive power in a wide range and fast response can be achieved by using turn off devices. A fast response and wide range power controllability are essential for the stabilizing mode of SMES.

The operating principle consisting of thyristor or turn-off devices controlled by a firing circuit: positive gat signal initiates the current conduction at prescribed time to maintain the desired average voltage across the coil.

#### 1.4.1.2 Voltage-source inverter

A VSI consists of turn-off device based converter, a DC link capacitor, and inductance on the AC side. The large capacitance ensures that the voltage is unipolar. An inductive interface is needed to keep the DC link capacitor not short-circuited. It should be noted that the VSI must have bidirectional valves to allow current flow in both the directions. Furthermore, there is no need for reverse voltage capability of the turn-off devices, since the DC voltage does not reverse.

The Ac output voltage can be controlled by varying the width of the voltage pulses, and the amplitude of the DC bus voltage.

The VSI and the chopper are linked by a DC link capacitor that behaves as a stiff, but controllable DC voltage source providing the desired characteristics. The state of charge of the capacitor is regulated by SMES which continuously inject of extract current from the DC bus by means of a PWM controlled chopper.

The implementation of CSI is more complex than that of VSI, particularly because of the potential over-voltage problems due to stray inductances and the need for AC side capacitive filter.

Two switching devices (SW1 and SW2) in the DC-DC chopper are switched on and off simultaneously and creating the voltage across the SMES. Changing the duty cycle of their switching pattern can control the DC component of this voltage.

### 1.4.2 Cryogenic cooling system

SMES are cryogenic devices, whose temperature must be low enough to ensure non-dissipative operation of the superconductors. The cold source is determined by several factors, principally the required temperature and the amount of heat losses, and are mainly:

- Gas/fluid flow, currently used in cable in conduit, where a cryogen, typically helium, is forced to circulate in the cable at the operating temperature of 1.5-10 K.
- Immersion in liquid bath, commonly used with helium if the operating temperature is 4.2 K or Nitrogen if the temperature is 77 K.
- Conduction, known as cryogen free, this system uses a refrigerator with a cold head in application with operating temperature above 15 K.

In the design of the cryogenic system other factor must be considered; the *n* value of the superconductor which leads to higher electric field in HTS increasing the idling losses. The other factor is the specific heat of the conductors which are lower at low temperature; this leads to a low thermal inertia and poor thermal stability. Instability event (e.g. vibration) can produce hot spot and thermal runaway or quench. Thus, especially LTS, needs additional material (copper) for stability.

# 2 The drysmes4grid project

## 2.1 Introduction

The DRYSMES4GRID project, aiming at demonstrating the feasibility of SMES technology based on $MgB_2$ with cryogen free cooling, was launched in 2017 by the Italian Minister for Economic Development. The aim of the project is to demonstrate the feasibility of 500 kJ / 200 kW SMES (Superconducting Magnetic Energy Storage) in the short/medium term at competitive cost based on Magnesium Diboride ($MgB_2$). This rating is deemed suitable for disclosing the critical technological aspects of all components in view of practical applications. A further goal of the project is the assessment of the technical and economic benefits that the SMES can bring to real-world electric grids.
The project is coordinated by Columbus Superconductors SpA, based in Genoa, Italy with the design, development. Production and commercialization of $MgB_2$ tapes and wire as main activities. Further partners are the University of Bologna, Italy, RSE SpA (Research on Energy System, Milan, Italy), ICAS S.C. r. l. (Italian Consortium for Applied Superconductivity, Rome, Italy) and CNR – SPIN (Institute for Superconductors, oxides and other innovative materials and devices, Genoa, Italy). This thesis work was carried out in the frame of the DRYSMES4GRID project. The main activity, the contribution of the partners and the time-line of the project are summarized in Fig. 2.1

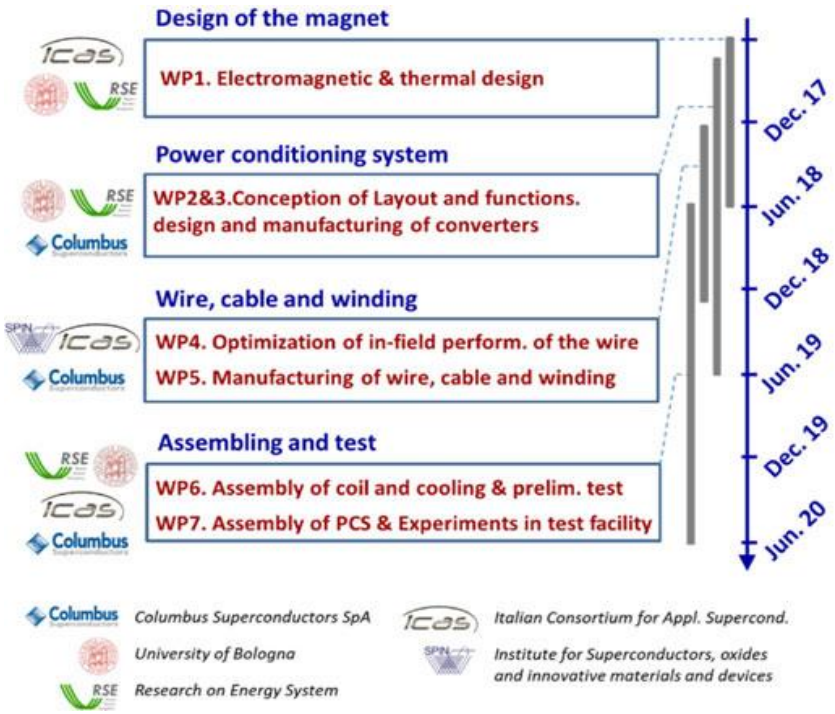

Fig. 2.1 Main activity and the time-line of the DRYSMES4GRID

## 2.2 State of art of SMES system and future development

Amongst the superconductors available at an industrial level and at competitive costs (less than 1 Euro/kAm) there are LTS (low temperature superconductors). The critical temperature of these materials (above of which the superconducting state is not allowed) varies between *9 K* and 19 K. for this reason such superconductors are used with cooling systems using liquid Helium, whose temperature is *4,2 K.* Some of these materials are also used in various applications of superconducting magnet energy storage (SMES). The main advantages of superconducting storage compared to the classic methods are a high speed response (*1-5 ms)* a high power density (up to *107 W/m3*), high efficiency (*95%*), a long useful life (*>30* years) and low environmental impact. Among the major full-scale SMES applications it is possible to mention the two unit of *10 MW / 19 MJ* operating at the Chubu Electric Power Company Network for the protection of a semiconductor manufacturer, extremely sensitive to voltage disturbances. Despite the high performances of SMES technology, its market penetration is not still complete due to:

- high cooling power due to the extremely low operating temperature (*4,2 K);*
- high cost and complexity of the refrigeration equipment with liquid Helium.
- losses in stand-by phase in the DC/DC power converters connected to the magnet.

In order to reduce the first two disadvantages, a possible solution is the use of HTS (high temperature superconductors) lately available on an industrial level. These conductors are characterized by very high critical temperature (*90 -110 K*). This temperature makes conduction cooling (cryogen-free) possible. the feasibility of HTS SMES has been demonstrated through some demonstrative applications (up to *800 kJ / 175 kW*). However, the cost of these materials is so high that it does not allow the economic competitiveness of the system.

To exploit the potential offered by the SMES storage system, it is crucial the role of converters to connect the system itself to the grid. Furthermore, the topological characteristic of such converters can influence the efficiency of the system. In fact, although the round-trip efficiency of a consecutive charge and discharge cycle is very high, in stand-by phases, the current flows permanently through the DC/DC converters, causing non-negligible losses. These losses deteriorate the long-term efficiency of the system, especially when power is not constantly exchanged with the grid (power quality applications). The project is aimed also to demonstrate the feasibility of this system with high efficiency and performance and with competitive costs. The main advantage of this technology is the simplification of the cryogenic part. The critical temperature of $MgB_2$ is *39 K,* therefore it can operate with sufficient performance it the temperature range of *15-20 K,* and it can be cooled by conduction rather than by helium bath, thus avoiding the disadvantages in terms of complexity and safety of liquid helium system.

The $MgB_2$ superconductor is typically used for biomedical applications and represents a low-cost alternative to HTS superconductors (its cost per kAm is 10 to 20 times lower). The disadvantage is the lower magnetic field that can be reached in the operating temperature range. This means that for the same amount of energy to be stored, larger

windings are required and greater amount of superconductor. However, thanks to the low cost of the material, this does not compromise the competitiveness of the SMES system.
Plus, an increase in performance of the material can be obtained by optimizing its productive process. Using nano-sized boron powders (produced by one of the partners of the project), high field performance of $MgB_2$ can be achieved by increasing the pinning.
The optimization of the material will also have the purpose of reducing the intrinsic electromagnetic losses of the superconductor, relevant in SMES applications given the extremely fast charge and discharge cycle. In order to minimize AC losses, wires and tapes are furtherly optimized (reduced filaments diameter, low conductivity matrix, non-magnetic insulation). Also important is the optimization of the cooling system, which will ensure the operation of the superconductor at temperature between *16 K* and *24 K*.
In order to minimize the overall cooling power thermal vacuum insulation and multilayer material (MLI) and innovative cryocooler are adopted.

## 2.3 Impact on the power grid

The integration of the SMES is a efficient tool to satisfy needs that can occur at both the grid and user level. A SMES system can delivers complementary features compared to other storage system (batteries) and also allows the creation of hybrid system (energy intensive + power intensive). extremely performing. This combination can provide temporary surplus of power without an over-dimensioning of the system.
The benefits that a SMES system can offer to the electric system are:

- Power quality enhancement, the SMES is able to compensate the interruption and voltage dips. For such applications, power in the order of MW and discharge duration of few seconds are required. Moreover, the SMES is useful for disconnectable customers.
- Great penetration of distributed generation, SMES is a technology that can control power flow reliability in presence of rapid fluctuation. In this case represents a perfect device to integrate non-programmable resources. Thus, the system can be dimensioned according to the average power whereas SMES ensures the power during the peaks to the load.
- Stabilization of micro-grids and off-grid system, a power reserve of the order of a few MW is needed for the reliable operations of those system which are not interconnected with an extended electric grid.
- Leveling of impulse load, many industrial plants and equipment operate in cyclic conditions, but the power absorbed in short part of the cycle reaches peaks considerably greater than the average value.

## 2.4 Goals of the project

The goal of the project is to create a demonstrator of such a scale to highlight all aspects necessary for the concrete development of the SMES technology. The most specific aspect is to verify the adoption of a new material for this context. The Magnesium Diboride has the advantage to be available in sizes and costs of industrial interest to achieve an economically more convenient technology. Therefore, other aspect will be pointed out, such as:

- Development of design and optimization methods (ad numerical implementation) necessary for the executive project of the demonstrator and also usable for the design of full-scall devices;
- Grid studies that analyze the advantages deriving from the introduction of SMES (in hybrid system or in stand-alone system) with networks of real interest according to the position of the device in presence of Distributed Generation (DG). Digital simulations, control logics test and hardware validation will be implemented;
- Design of full-scale devices for significant applications will be evaluated as well as impact on the electric system users, market prospective and future developments.
- Test of the demonstrator in the RSE test facility.

# 3 Electromagnetic and mechanical design of the magnet system

The outcome of the design activity of the $MgB_2$ coil are dealt with in this thesis. Both the developed methodology and the design results are reported in detail. The preliminary design, concerning the definition the geometry of the coil and the reference $MgB_2$ conductor based on the functional requirements of the system (stored energy and deliverable power), is first discussed. The detailed design of the coil, aimed at producing the information and the technical drawings needed for the manufacturing of the coil, is then presented. Assumptions concerning the general layout, support material and electrical insulation are described. The mechanical behavior of the coil during cool down and successive energization up to the nominal transport current is analyzed and the compatibility of stress and strain with allowable limits of the conductor is verified. Distribution of electrical stress on the coil during the switching of the power electronic converters is also calculated for the proper design of electrical insulation. Modelling assumptions, as well as material properties used for the calculation, are reported. Results of quench analysis are also presented showing that the maximum hot spot temperature reached when the coil is discharged is within the design value.

## 3.1 Operative requirements of DRYSMES4GRID system

The aim of DRYSMES4GRID project is to build and test in a relevant facility a 500 kJ / 200 kW SMES demonstrator made of Magnesium diboribe with a cryogen-free cooling system. The project addresses the engineering aspects necessary for the concrete development of the technology, in particular: winding technology, stability of the magnet during charging and discharging, electrical insulation tightness, temperature uniformity, reduction of refrigeration power. A further element of the system is the power conditioning system (PCS), which is the set of converters used to transfer the energy of the magnet to the network operating under alternating current conditions and vice versa. the PCS controls the charging and discharging of the coil thus controlling the power supplied / absorbed by the network. The preliminary layout chosen for the power conditioning system (PCS) is shown in Fig. 3.1.

The magnetic energy contained within the magnet is released through a two-quadrant chopper that keeps the voltage across the DC bus constant (750 V dc); The SMES can provide active power to the load during network unavailability (UPS operation) or it can act as an active filter for harmonics compensation and reactive power regulation during normal operation [10]. The SMES is also equipped with a protection system, integrated in

the PCS, which avoids the risk of damage to the magnet caused by extraordinary conditions attributable to thermal, electrical or mechanical disturbances. Protection is achieved through a quench detection system and an external resistor for emergency discharge. The functional requirements and main parameters of the SMES system are reported in Table 3.1. In particular, voltage of *Vdc = 750 V* is chosen for the DC bus and, moreover, a voltage of *1 kV* is chosen as the withstand voltage of the electrical insulation this value is typical for conduction-cooled magnets. This voltage is also typical for electronic converters with power levels in the order of MW.

Table 3.1

MAIN CHARACTHERISTIC OF SMES SYSTEM

| | |
|---|---|
| AC voltage – grid side | *400 V rms* |
| AC voltage – inverter side | *250 V rms* |
| bus DC voltage | *750 V* |
| discharge time | *2.5 s* |
| deliverable power | *200 kW* |
| Deliverable energy | *500 kJ* |

For a SMES system, the stored magnetic energy *E* and the instantaneously exchanged power *P* can be expressed as:

$$E = \frac{1}{2} LI^2 \tag{3.1}$$

$$P = \frac{dE}{dt} = LI\frac{dI}{dt} = VI \tag{3.2}$$

Where *I* and *L* are the current and the inductance of the coil. Also the relationship between volumetric energy *E* [$J/m^3$] and magnetic flux density (*T)* is given by:

$$E = \int \frac{B^2}{2\mu_0} d\tau \tag{3.3}$$

the SMES current during the delivery of this power cannot be less than $I_{min}$ in order to be able to always deliver the power required. A non-negligible amount of unused residual energy is stored in the magnet, causing an over dimensioning of the coil.

$$I_{min} = P/V_{dc} = 266{,}6\ A \quad (3.4)$$

$$E_{min} = \frac{1}{2} L I_{min}^2 \quad (3.5)$$

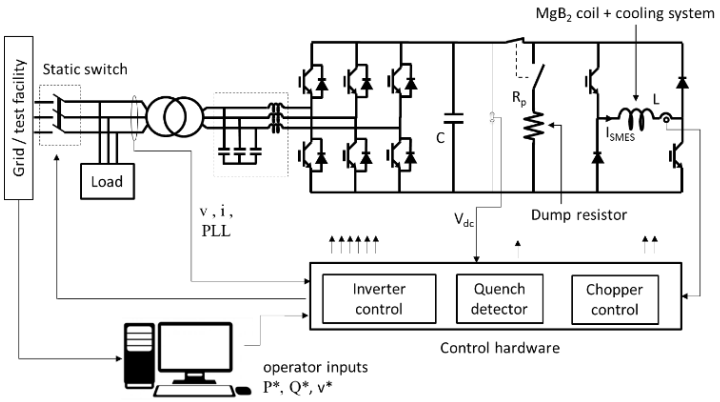


Fig. 3.1 scheme of PCS and control system

## 3.2 $MgB_2$ superconductor

The choice of material is generally concerned to physical-technical characteristics of the superconducting compound (operating temperature, critical current, critical field) and mechanical characteristics (resistance to mechanical stress and deformability). But another important factor is its cost, and an overall balance between all characteristics place $MgB_2$ as an alternative and competitive solution compared to other materials. Based on the indications of the partner Columbus Superconductors, a six-filament superconducting wire and tape are taken into account for the design of the magnet shown in Fig. 3.2

| Number of Filaments | 6 |
|---|---|
| superconductor | MgB2 (29%) |
| External sheath | Monel (44%) |
| Internal matrix | Nickel (24%) |
| thickness | 1,1 mm |
| width | 2,05 mm |

Fig. 3.2. characteristics of $MgB_2$ superconductor

The tape consists of six $MgB_2$ filaments embedded in a nickel matrix with an Monel layer added at the outermost part. The current carrying capacity of the superconducting wire is an integral part of the magnet design. The operating temperature $T_{op}$, operating current $I_{op}$, and maximum magnetic field on the wire, $B_{max}$, must be consistent with both the magnet design and the critical current of the superconducting wire, $I_c$ *(B, T)*. For persistent current mode operation, the n-value limits the operating current to about ~60% (of $I_c$*)* of the critical current. Since $B_{max}$ is strongly correlated with the main field strength, and $T_{op}$ mainly determined by the efficacy of the conduction cooling system, the ability to design the superconducting magnets is determined by the performance of the superconducting wire.

The $I_c$*-B* characteristic curve of the tape at different temperatures, is shown in Fig. 3.3. The figure also shows the interpolation of the experimental data obtained through the analytical approach reported [11]. The fitting of the critical current as a function of the magnetic field and the temperature is determined using the empirical formula:

$$I_c(B,T) = 3.2e^{-6}A_{sc}[a_1 T e^{-b_1 B} + a_2 e^{-b_2 B}] \quad (3.6)$$

$A_{sc}$ is the cross section of the superconductor and the parameters are $a_1 = -14{,}26$ $a_2 = 585$ $b_1 = 0.31$ $b_2 = 0.53$ . the *fitting* by means of the formula is shown in Fig. 3.3.

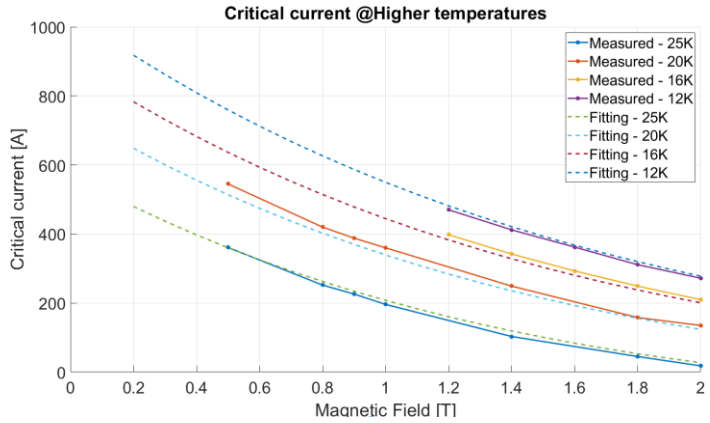


Fig. 3.3. Fitting of characteristic curve Ic-B of $MgB_2$ superconductor

$MgB_2$ wire is of particular interest also due to its mechanical stability, small mechanical and thermal anisotropy [12]. There is an increasing focus on $MgB_2$ wires, but a crucial point is its low failure strain; indeed, the value of critical current is affected by the strain as shown in [13]. Usually, the critical current value has a significant drop for values of strain around *0,5%*. A magnet experiences strain development caused by pretension during the winding process and an anisotropic deformation due to cooling down, over the forces generated when the magnet is electrically charged. Thus, it is critical to understand the strain distribution in the coil.

## 3.3 Preliminary design

In the design stage of a coil, several factors are taken into account to achieve the possible best performance of a SMES system at lower cost. These factors may include coil configuration, energy capability, structure, operating temperature. The solenoid and toroid shaped SMES coils are two main coil designs which have been extensively studied [14]. Solenoid type is simple and easy to construct, and it minimizes the amount of conductor for a given storage capacity. However, this type of design results in rather large strays magnetic field, which may impose some restriction on the site where the SMES can be allocated due to the concerns related to environmental and health effects. To reduce the stray magnetic field, an alternative was sought, and a toroid coil design was utilized. Given that this design is more complicated to fabricate, and significantly more expensive since it requires the use of more conductors . it is chosen a solenoidal configuration [15]

In order to carry out the electromagnetic design the input parameters listed in Table 4.3 are preliminary chosen:

- *Operating temperature of the superconductor,* the range in which the operating temperature can be chosen is particularly limited and ranges from 16 K to 24 K
- *reference field of the solenoid,* the design value of the maximum magnetic field on the conductor (obtained in correspondence with the internal radius in the middle plane of the magnet) is equal to *2 T*, an increase in $B_{max}$ has a positive impact in energy density but causes larger radial and axial stresses that need to be supported with more structural material that induces more cost. The value of the magnetic field is obtained at the internal radius of the solenoid in the middle plan of the magnet where the magnitude has the highest value; the isotropic behaviour of the electric properties of $MgB_2$ allow to not consider the influence of the orientation of the field on the conductor. This value is chosen as a preliminary assumption for the iterative process to obtain the optimal geometry.
- *Aspect ratio,* For the sizing of the solenoid, an Aspect ratio (height / diameter) of 2 was also chosen. The value of aspect ratio is chosen considering that, with this value, the coil can be taken as ‘long’ magnet and the domain of the integral to obtain the volumetric energy density is reduce to the volume inside the coil.
- *Filling factor,* another important parameter is the filling factor *b*, which is the fraction of the cross section filled with the SC conductor. This takes into account both the filling factor of the cable (in case of multi tape cable is considered) and the electrical insulation.
- *Safety factor,* the ratio of the SC current and its critical value.

### 3.3.1 Methodology

The volume $V_{bore}$ of the solenoid bore is obtained as a function of the energy delivered ΔE and the volumetric energy density corresponding to the assumed reference field ($B_{max}$). the internal diameter ($d_{sol}$) of the solenoid is obtained accordingly by considering the aspect ratio (*a)*

$$V_{bore} = \frac{2\mu_0 \Delta E}{B_{max}^2}; \quad d_{sol} = (4V_{bore}/a\pi)^{1/3} \tag{3.7}$$

Given a value of thickness of the solenoid $\delta_{sol}$, the magnitude of the magnetic field at the point of the highest value is proportional to the current density of the solenoid via the geometric coefficient *k (B=kJ(B))* so that it is possible to obtain a *load line* of the coil with the value of the magnitude of the magnetic field depending on the value of the current circulating in the coil. the critical current density of the superconductor is obtained by intersecting the load line of the coil with the *Jc-B* curve, that is by solving:

$$J_c(B) = \frac{1}{b\,c}\frac{B}{k} \tag{3.8}$$

Where *b* filling factor of the solenoid and *c* is the safety factor of *0,6.*

Afterwards, the number of turns *N* is chosen. This is an important parameter since it affects the inductance. The maximum current $I_{max}$ and the deliverable energy ΔE of the solenoid are given by:

$$I_{max} = \frac{J_{max} b\ c\ H_{sol}\delta_{sol}}{N} \tag{3.9}$$

$$\Delta E = 1/2L(I_{max}^2 - I_{min}^2) \tag{3.10}$$

Both the quantities depend on the thickness and the number of turns. Note that the maximum storable energy does not depend on *N* since the inductance *L* increase as $N^2$. Given a solenoid with assigned thickness $\delta_{sol}$ and maximum energy, a high number of turns (high inductance) is desirable since it implies a smaller maximum current with less losses and smaller current leads. However, the deliverable energy also decreases with the number of turns since the residual energy at $I_{min}$ increases. This means that, if a large number of turns is used, a larger solenoid must be used with much higher capital cost. A larger magnet with greater accumulated maximum energy would be needed to deliver the same energy.

### 3.3.2 Reference coils

In order to define the optimal configuration of the magnet it is useful to refer to the significant contribution that the cooling system makes to the overall cost; the lower is the temperature required for the coil, the higher the performance of the cryocooler and its cost. The performance maps of a SMES are shown, referring to two different levels of deliverable power in. It can be seen how, for a given value of magnetic field reference and deliverable power, different values of deliverable energy can be obtain depending on the maximum current $I_{max}$ (which takes into account filling factor and safety factor as in ( 3.9)) reported in Fig. 3.4 performance maps of SMES at different deliverable poweras parallel lines. In the same plot is also shown the curve of the critical current depending on the temperature and reduced by the safety factor *c*.

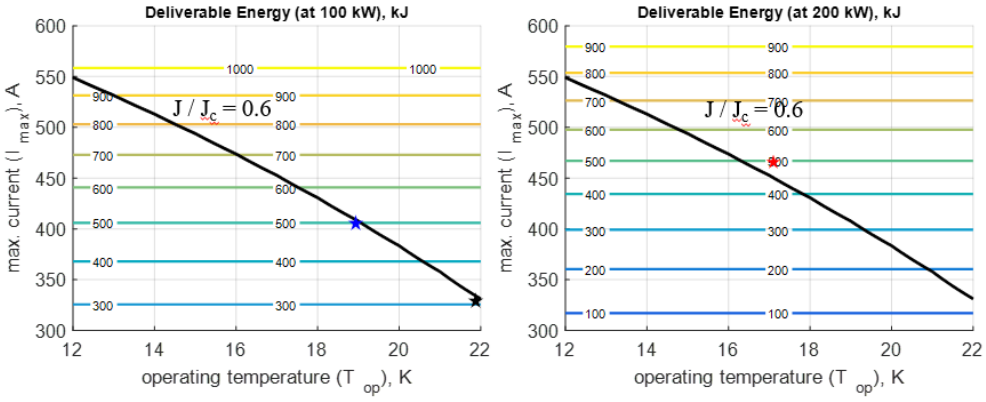


Fig. 3.4 performance maps of SMES at different deliverable power

By intersecting the maximum current curve for the superconductor with the lines relating to the various levels of energy the value of required current and the operating temperature of the system in the different conditions is obtained. In order to accomplish the project requirement (deliverable power of *200 kW* and deliverable energy of *500 kJ*) a temperature of *16,7 K* is obtained with an operative current of *467A*, as reported in Table 3.2. Although the further analysis consider the configurations expected by the specifics of the project, other configurations with 'lighter' requirements are considered in Table 3.2, with lower deliverable energy and power.

Table 3.2.

PARAMENTERS AT DIFFERENT POWER AND DELIVERABLE ENERGY

| **Power [kW]** | **energy [kJ]** | **Temperature [K]** | **current Imax [A]** |
|---|---|---|---|
| ***100*** | *300* | *22* | *306* |
| ***100*** | *500* | *19* | *407* |
| ***200*** | *500* | *16.3* | *467* |

The main characteristics of the designed coil are reported in Table 3.3. The geometrical layout is shown in Fig. 3.5 along with the field map at the maximum state of charge. The total energy stored is *741 kJ*. Once the geometrical layout of the coil is arrived at, a further choice is needed between the number of turns and the current of the conductor.
By choosing a tape a total number of *5220* turns, arranged in *10* layers of *522* turns each, are needed for filling the cross section of the coil (a filling factor of *0.646* is considered for the tape, and a filling factor of *0.907* is assumed for the winding).The maximum current of the SMES, corresponding to the maximum state of charge, is *467 A* in accordance with the design requirement, is *60%* of the critical current of the wire at the corresponding field of *2.0 T* and temperature of *16.7 K*. The inductance of the coil is *6.8 H*. The residual energy of the coil after a discharge at *200 kW* for *2.5s* is *241 kJ* (32% of the total), corresponding to a current of *267 A*.

Table 3.3

CHARACTERISTICS OF 500 KJ / 200 KW SMES COIL

| | |
|---|---|
| Inner radius , $d_{sol}$ | *300 mm* |
| height, $H_{sol}$ | *1200,6 mm* |
| number of layers | *10* |
| number of turns per layer | *522* |
| Number of turns, *N* | *5220* |
| tape length | *10,1 km* |
| Maximum current, $I_{max}$ | *467 A* |
| Minimum current, $I_{min}$ | *266,6 A* |
| maximum magnetic field, $B_{max}$ | *2 T* |
| Safety factor, *c* | *0,6* |
| Inductance, *Lc* | *6,8 H* |
| Total energy | *741 kJ* |
| Deliverable energy | *500,4 kJ* |
| Dump resistance | *2,14* |

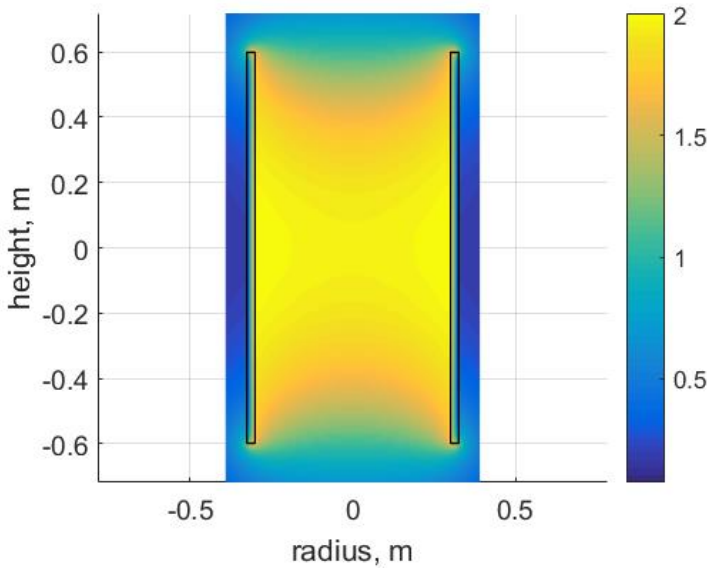


Fig. 3.5 Layout and magnetic field map for the coil at operative conditions

### 3.3.3 Hot Spot temperature - preliminary estimation

A thermal runaway can occur when the superconductor heats up locally over the current sharing temperature $T_{cs}$, the temperature above which the superconductor can no longer carry the full current, at which point the excess current flows in the matrix. If the length of the normal zone in the cable is sufficiently large, the Ohmic heating exceeds the cooling causing the normal zone to grow and propagate until the conductor is destroyed. To improve the thermal stability of the conductor, a fraction of the conductor's cross section is made of copper stabilizer. When the voltage over the conductor rises this is an indication that a growing normal zone is present. In the case of a resistive voltage in the coil (quench), the protection system acts by disconnecting the coil from the DC bus. The energy contained in the magnet is discharged onto an external resistance and the current.

Preliminary stability assessment is performed. it is verified that the hot-spot temperature caused by possible disturbance is contained within the admissible limits the current during this phase. The resistance value should ideally be as high as possible so as to allow a very rapid discharge; in reality this value is limited by the maximum voltage value to which the magnet can be subjected during discharge. Assuming that the quench occurs in the most severe condition, that is when the coil carries the maximum current of *467 A*, and assuming a maximum voltage value on the insulation of the electric devices equal to *1 kV*:

$$R_P = \frac{V_{max}}{I_{max}} = 2{,}14\ [Ohm] \tag{3.11}$$

$R_P$ is the resistance value that allows not to exceed the voltage limit on the circuit in order to protect the devices. Furthermore, in order to obtain a realistic evaluation of the time course of the current after the disturbance, it is necessary to consider a delay time necessary for the QD system to detect the quench and command the opening of the discharge switch. A delay time *Td = 0.3 s* is assumed. The increase of temperature due to a quench event is determined through a zero-dimensional balance between the generation of heat due to the Joule effect and all the thermal capacities of the different materials of which the magnet is composed [17] are considered as follows:

$$J_{Cu}^2(t)\rho_{Cu}(B,T)dt = \left(\sum_i C_i(T)\,\gamma_i f_i\right)dT \qquad (3.12)$$

*Ci* is the specific heat of the *i*-th material depending on temperature, $\gamma_i$ is its density and $f_i$ is its volume fraction. During the steady state condition, the current *Imax* flows through the superconducting section of the conductor. Over the *critical* temperature, the current flows in Copper, so that $J_{Cu}(t) = I_{max}/S_{Cu}$ is the current density referred to the Copper cross section.

In Fig. 3.6 is shown the current during the discharge of the coil on the dump resistor. The profile represents a common *RL* discharge where *Rp* is the dump resistance and *L* is the inductance of the coil, so that $\tau = L/R$ is the time constant of the circuit.

The temperature profile during the quench is shown in Fig. 3.7.

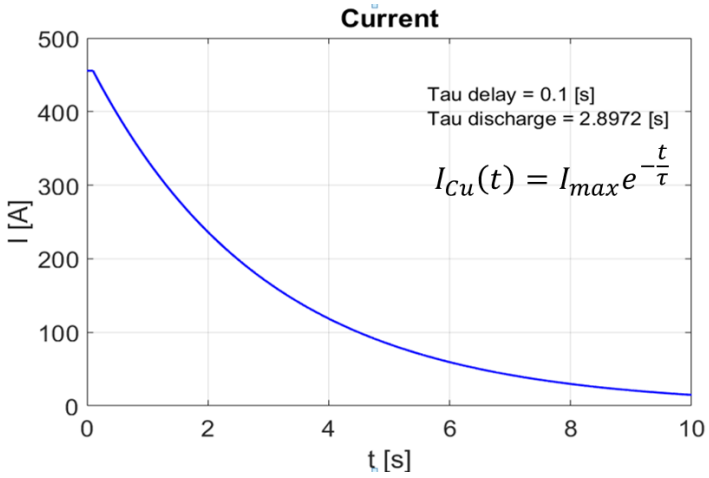


Fig. 3.6. Current during the discharge

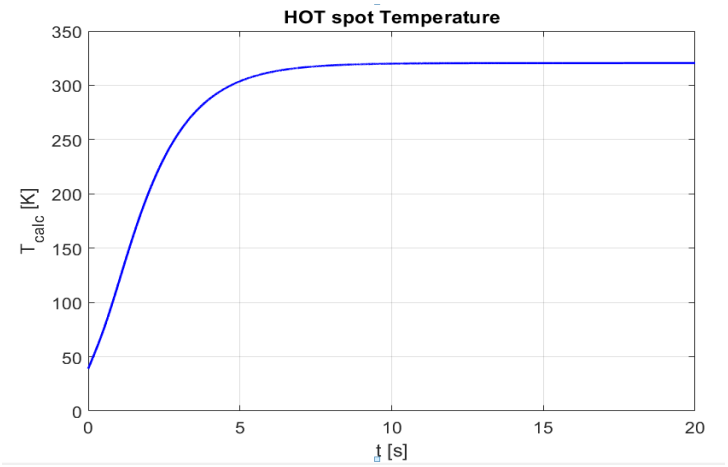


Fig. 3.7. Hot spot temperature during the discharge

Two simplifications have been made in this system to avoid solving the complete differential equation system:

- the system is considered adiabatic [18],
- no longitudinal heat diffusion is considered (thermal conductivity is eliminated from the heat transfer equation);

This zero-dimensional approach is useful for having a preliminary estimate of the temperature increase during a discharge due to a quench. It can be seen that the increase of temperature leads to an increase in heat capacity and resistivity and, at the same time, the current value is reduced, so that a final temperature of 322 K is reached. This hot-spot temperature is however higher of the allowed limit $T_{max}$, which for a conductor in $MgB_2$ is around 200 K. However, it must be considered that the adiabatic model used here is conservative. A more detailed analysis of the quench will be developed in the quench analysis section, in which a three-dimensional model will be developed in which the transverse and longitudinal heat diffusion is taken into account.

## 3.4 Mechanical analisys

An appropriate analysis of the mechanical performance of the coil is essential for the safe and reliable operation of the SMES system [19]. In fact, the strain due to the mechanical load influences the performance of the superconductor. In addition, excessive shear stress in the epoxy can produce cracking that leads to a failure of the electrical insulation [20]. In order to correctly evaluate the mechanical load to which the magnet is subjected, three phenomena must be considered:

- *Pretensioning* due to the winding process of the superconductor onto the mandrel;
- *Thermal contraction* due to the cooling-down from the room temperature to the operating temperature;
- *Lorentz forces* due to the energization of the magnet to its operating power.

As discussed in the previous section, the SMES coil consists of 10 layers of 522 turns each. A schematic of the top part of coil including the mechanical support elements and the copper layer for thermal connection of the coil to the cryo-coolers is shown in Fig. 3.8 The coil is built using the insulated tape introduced in the previous section, which is wound on a *3 mm* thick steel mandrel; a *0.5mm* thick press-board is added on the mandrel to provide proper ground insulation to the innermost layer (layer 1) of the coil in contact with the mandrel [21]. The same pressboard is applied to the outer surface of the outermost layer. During the winding of the coil, a layer of fiber glass is interposed on each layer of the winding and finally a layer of *1 mm* of copper is added at the external surface of the magnet for the thermal connection with the cryo-cooler. The magnet is impregnated with Epoxy Resin; the impregnation of the glass fiber and polyester, with which the tape is insulated, allows to obtain composite materials that act as mechanical support and electrical insulation [21]. In the upper and lower sections of the magnet, Vetronite discs are applied on which the flanges subsequently anchored to the mandrel will be located.

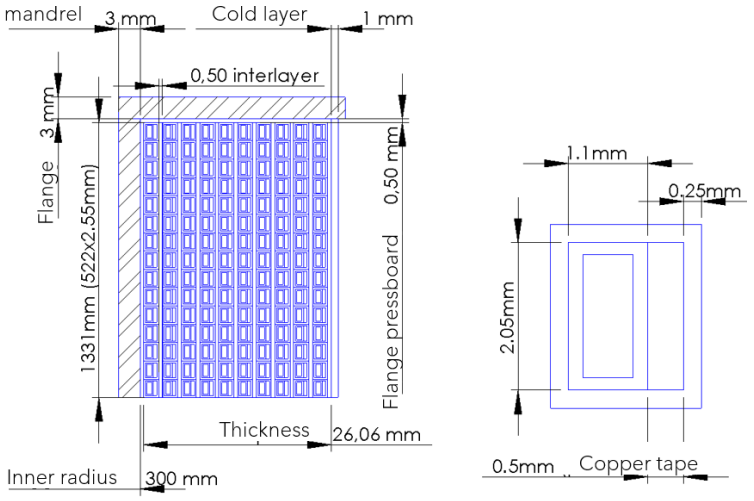


Fig. 3.8. Geometrical scheme of a)the top pf the coil b)insulated tape

The aim of this section is:

- calculate the distribution of stress and strain on the whole coil
- verify that the allowable value is not exceeded on the $MgB_2$ conductor to prevent a drop of the critical current of the conductor
- the allowable stress is not exceeded to avoid any weak points for electrical insulation.

the complete layout of the winding reported in this section was obtained after numerous iterations of the analysis. Different layouts were considered with different mandrel materials (steel, aluminum), thickness and position (inside or outside the coil). Only the final layout is reported here. To carry out the mechanical analysis, a 2D axial-symmetric finite element model was developed in ANSYS environment to evaluate in detail the distribution of stresses; in this analysis the real geometry of the magnet is used in which all the components are modeled and the properties of the constituent materials are considered[23]-[24].

### 3.4.1 Material properties

In this section the material properties used in the coil design re reported. A homogenized model is used for the composite conductor in $MgB_2$, in particular the homogenized composite includes the superconducting filaments and the nickel matrix; this area is surrounded by the Monel layer and the stabilization copper tape is also taken into account. Basically, a full wire model of a Representative Volume Element (RVE) is design and meshed with different constituent materials and their own properties; than, stress and strain are applied in different direction and the deformations of the RVE are obtained as FEM analysis results. The volume averaged strain state allows to calculate the homogenized mechanical properties. The techniques used for the homogenization of the different mechanical properties at cryogenic temperatures of the materials are reported in [25]-[26] and the results are shown in Table 3.4.

Table 3.4

HOMOGENIZED MECHANICAL PROPERTIES OF SC

| Material properties | Homogenized 6 filament wire |
|---|---|
| Modulus of Elasticity (Direction 1) | *153 [GPa]* |
| Modulus of Elasticity (Direction 2) | *123[GPa]* |
| Modulus of Elasticity (Direction 3) | *119 [GPa]* |
| Shear Modulus (direction 1-2) | *43.9 [GPa]* |
| Shear Modulus (direction 2-3) | *36.1 [GPa]* |
| Shear Modulus (direction 3-1) | *40.9 [GPa]* |
| Poisson's Ratio (direction 1-2) | *0.284* |
| Poisson's Ratio (direction 2-3) | *0.332* |
| Poisson's Ratio (direction 3-1) | *0.291* |
| Average thermal expansion coefficient (16-298 K) ($\alpha$23) | *10.79 [$\mu m/mK$]* |
| Average thermal expansion coefficient (16-298 K) ($\alpha$1) | *9.26 [$\mu m/ mK$]* |

The temperature dependent properties of the materials are shown below:

- *elastic properties* - the value of Young modulus of the conductor is obtained as an average weighted on the fractions of the modules of the different materials whose it is made of, shown in Table 3.5. In general, for all the materials employed in the magnet, the constitutive equation for is assumed to follow Hooke's law at the microscale. This property is considered independent of the temperature although its value varies from the ambient temperature to the operating cryogenic temperature.

Table 3.5.
YOUNG MODULUS OF THE COMPONENTS OF COIL

| | |
|---|---|
| Reference tape | *157.23 [GPa]* |
| Aluminum 5083 | *80 [GPa]* |
| Stainless steel | *180 [Gpa]* |
| Copper strip (RRR 100) | *137 [GPa]* |
| Fiber Glass G10-CR | *35 [GPa]* |

- *coefficient of thermal expansion* – All of the materials except G10 and GP03 have an isotropic thermal expansion coefficient. the characteristic curve of GP03 (polyester and epoxy resin ) is obtained as a weighted average of the constituent values

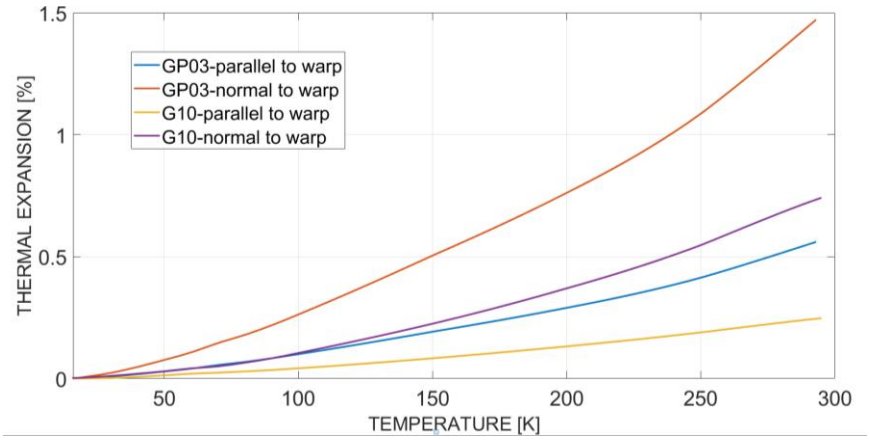


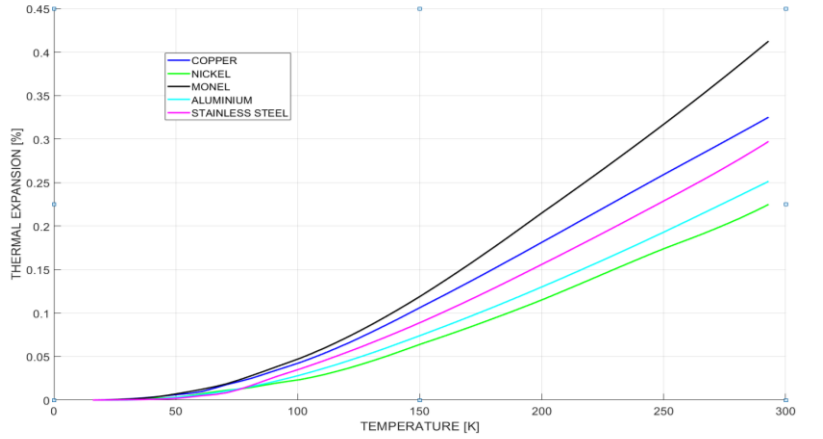


- *specific* heats The specific heat is the amount of heat required to raise the temperature of a solid uniformly by a unit temperature under either constant strain ($C\varepsilon$) or constant stress ($C\sigma$). However, the difference between the two types of specific heat is insignificant for solids and can be neglected in this case.

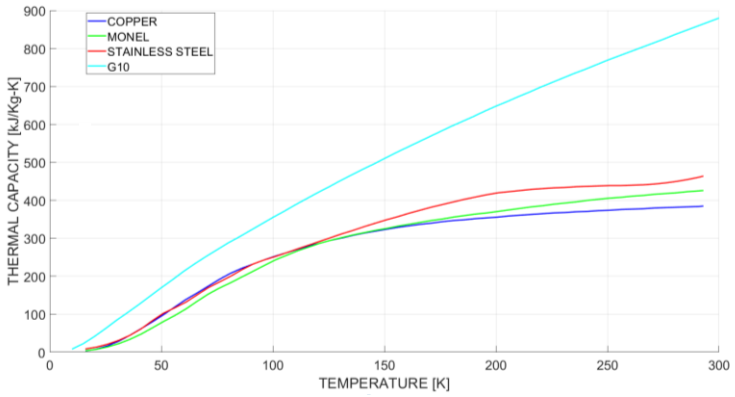


- *thermal conductivity* The thermal conductivity along the radial and axial directions is mainly driven by the conductivity of the epoxy since its thermal conductivity is at least an order of magnitude smaller compared to other components

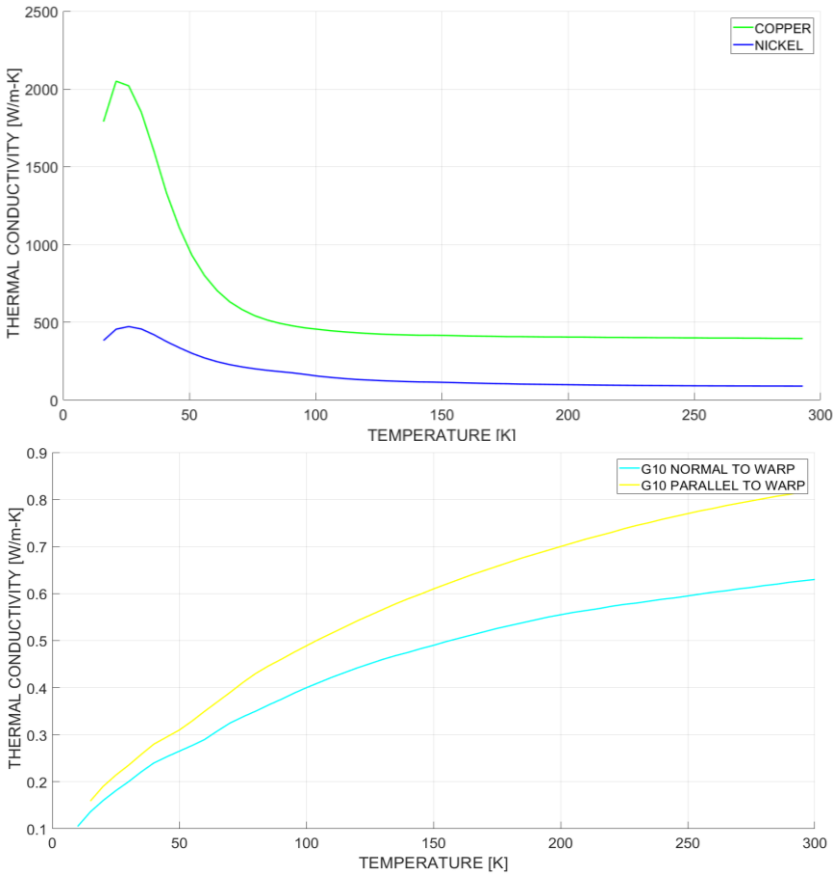

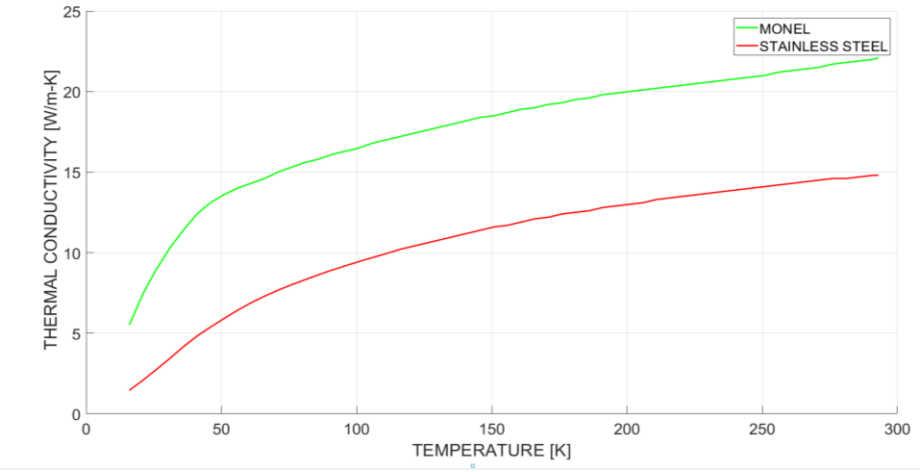


### 3.4.2 Methodology and results

Although there are well-proven analytical approaches to model winding, thermal cooling, and electromagnetic charging, the FEA-based computational approach is favored considering not only the material properties, but also the boundary conditions, geometric complexity, and variable elastic modules in each part of the system. Nevertheless, analytical evaluation is useful for a preliminary consideration and comparison on the behavior of the coil during the different phases, confirmed and detailed with the numerical approach.

In ANSYS the element used for the mechanical analysis is PLANE182. The element is defined by four nodes with two degrees of freedom at each node: translations in the nodal x and y directions, and rotation in the nodal y direction. The element input data includes also a thickness and the orthotropic material properties and temperature.

The insulating polyester wraps the conductor whereas the fiberglass layer is inserted between the layers of the coil and on the internal and external surfaces of the coil. The copper layer used as a cooling contact is fixed on the outer surface while the steel mandrel is used as a mechanical support on the inner side [27].

After the winding process, the magnet is assembled in the vacuum vessel and the copper contact is connected to the second stage of the cryocooler using a copper braid. The whole assembly is contained within Mylar sheets and in an aluminum heat shield. The entire structure is cooled to the nominal operating temperature of $16.7\ K$. Once this temperature is reached, the magnet is energized with a current of $476\ A$, thus generating a magnetic field of $2\ T$ which generates magnetic forces acting on the coil. The operating phases of the coil and all its components are analyzed in order to evaluate the strain distribution.

### 3.4.2.1 Winding Process Stress

The pretension depends on the settings of the winding process. A pretension of *31 MPa* is commonly applied for winding wires with dimensions similar to the case analyzed. Alongside numerical modeling, it is possible to analytically estimate the effect of this pretensioning, considering each layer of the coil as a thin concentric cylinder [28] and applying Hooke's law:

$$\varepsilon_i = \frac{\sigma_i}{E_i} - \sum_{j=1}^{3} \nu_{ji} \frac{\sigma_j}{E_j} \quad i = 1,2,3 \tag{3.13}$$

$\sigma_i$, $\varepsilon_i$ and $E_i$ are stress, *strain* e elastic modulus in three direction of a cylindrical coordinate system (r, θ and z), and $\nu_{ji}$ is Poisson coefficient. The radial force of the *i*-th layer is distributed on the surface of the inner layers as:

$$p_k = \frac{\sigma_{w_0,k} t_k}{r_1 + \sum_{j=1}^{i} t_j} = \frac{\sigma_{w_0,k} t_k}{r_{w,k}} \tag{3.14}$$

$\sigma_{w_0,k}$ is pre-load used on the winding operation on the k-*th layer*, $t_k$ is its thickness, $r_1$ is the radius of the first layer of the coil, and $t_j$ is the thickness of the *j-th* layer. The hoop stress due to that pressure are:

$$\sigma_{\theta i} = \frac{p_k (r_1 + \sum_{j=1}^{i-1} t_j)}{\sum_{j=0}^{i-1} t_j} \tag{3.15}$$

And this value is added to the pre-load, so that the total hoop stress on the *k-th* layer is:

$$\sigma_{wk} = \sigma_{w_0,k} + \sum_{j=k+1}^{n} \sigma_{\theta i} \tag{3.16}$$

To simulate the winding process, a particular technique is used within the axial-symmetrical 2-D FEA analysis: that is, the *birth-and-death* elements are used. At first the pre-tensioning of 31 MPa on is applied on all the layers, then the elements that make up the layers are deactivated and subsequently activated progressively starting from the element of the first layer in contact with the mandrel in order to imitate the winding process. Fig. 3.9 shows a comparison between the finite element approach and the analytical approach to solve the development of stress by winding. As can be seen from the graph, a compressive load develops on the layer near the mandrel. Furthermore, a difference between the two models is highlighted in this area due to the fact that the analytical model

is not able to evaluate the transition between two materials with different elastic modules, in particular between the mandrel and the conductor.

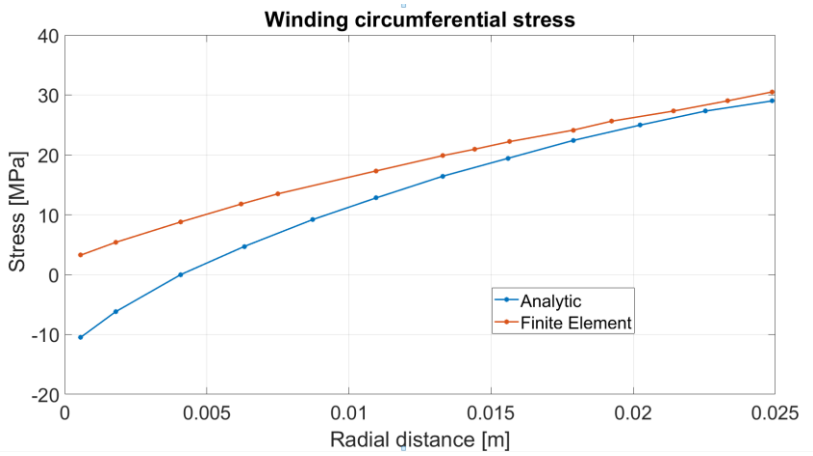


Fig. 3.9, comparison between analytical and numerical winding hoop stress

### 3.4.2.2 Cool-down stress

After the winding process, the next step is to cool it down to the operating cryogenic temperature. This cooling creates additional stresses due to the different expansion coefficients of the materials of which the magnet is made of. The additional strain value reported as a result of the temperature drop from ambient temperature ($T_0$) to the cryogenic temperature ($T_f$) is expressed by the analytic formula [29]:

$$\varepsilon_r = \frac{\partial u}{\partial r} - \int_{T_0}^{T_f(r)} \alpha_r dT\,; \quad \varepsilon_\theta = \frac{u}{r} - \int_{T_0}^{T_f(r)} \alpha_\theta dT \tag{3.17}$$

$\varepsilon$ is the *strain* e $\alpha$ is the coefficient of thermal expansion. The hoop stress are calculated as below:

$$\sigma_0 = \frac{kcr^{k-1}}{kL - V} + \frac{kdr^{-k-1}}{kL + V} + \sum_{i=0}^{n} \frac{1+i}{L} \frac{l_{ri} - (1+i)l_{0i}}{(1+i)^2 - k^2} \tag{3.18}$$

where $l = \alpha \Delta T$ for the i-th element of the time discretization, $\nu_{\theta z}$ e $\nu_{z\theta}$ are the Poisson coefficients $E_\theta$ and $E_r$ are the elastic modulus of the materials e $a$ e $b$ the inner and out radius of the cylinder. This analytical method is used to calculate the distribution of stresses due to cooling along the layers of the winding. Fig. 3.10 shows the comparison between the results of the analytical and numerical method for a coil made up of a homogenized material.

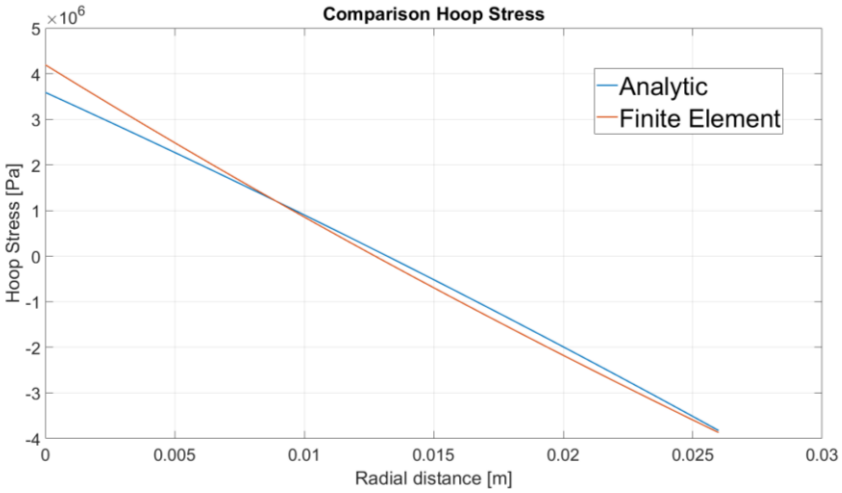


Fig. 3.10. Comparison between analytic and numerical cooling down hoop stress

The fundamental equation used in FEA for stress assessment is:

$$\{\sigma\} = [D]\left(\{\varepsilon \quad\} - \{\varepsilon^{th}\}\right) \tag{3.19}$$

For the comparison to be valid, it has been assumed that the elastic modulus of the magnet is independent of the temperature. In practice, the real elastic modulus of the superconductor can vary during cooling process from ambient to cryogenic temperature, so it is important to use an appropriate average value. from the graph it is possible to note that the maximum effective value of circumferential stress is obtained on the external radius [28].

Thermal stress can be reduced by adding a glass fiber inter-layer between each layer, which will be impregnated with Epoxy resin; this material has thermal contraction properties similar to the conductor so that the distribution of strain between the epoxy resin and the conductor is uniform, decreasing the stress on the entire coil.

In the FEA analysis, more detailed geometry and materials are used to consider more realistically the distribution of stress and strain due to the cooling on each material.

A *contact-model* is used in the contact surfaces between the mandrel and the coil, where sliding is allowed. The lower coefficient of thermal contraction of the steel of which the mandrel is composed, introduces a further stress in the internal part of the coil since its deformation by contraction is forbidden by the mandrel itself; in addition there is a detachment of the magnet from the mandrel in the upper and lower regions due to the high coefficient of thermal expansion of the copper . Sliding is not expected for this layer since it is impregnated with the entire winding, therefore, its deformation propagates to the coil

causing the detachment of the top of the magnet from the mandrel and, moreover increasing the compressive stress at the outer surface of the magnet. In Fig. 3.11 and Fig. 3.12, respectively, the stress and strain maps on the magnet section refer to the state of magnet cooled to cryogenic temperatures without any transport current.

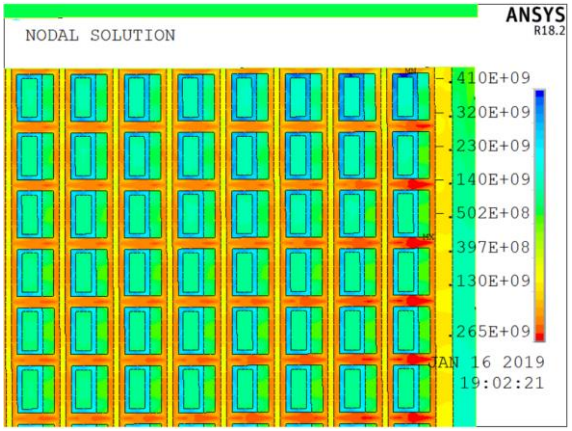


Fig. 3.11. Axial-symmetrical distribution of cooling-down stress

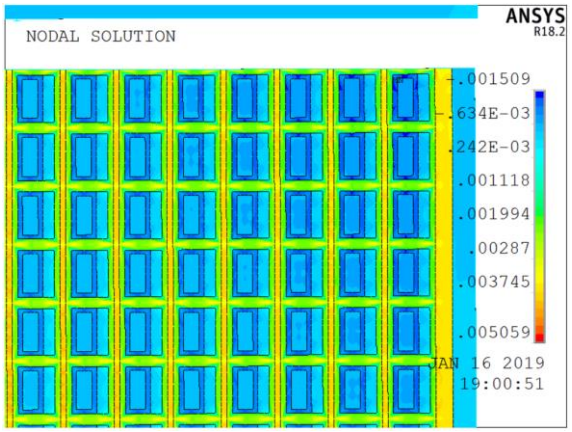


Fig. 3.12 Axial-symmetrical distribution of cooling-down strain

From the stress and strain maps it is possible to see that the conductor is subjected to a force that is below the allowed limit value but the resin between two adjacent turns is more stressed especially in the outermost layers; this is due to the difference in the value of the thermal expansion coefficient between the cold contact of external copper and the polyester of which the conductor coating 'sock' is made. Indeed, the different level of compression between two material produce shear forces at the contact surface. The pressure on the conductor caused by the Polyester in compression reaches *122 MPa* with a *0.07%* of strain, however below the critical value for $MgB_2$ (from -0.3% to 0.2%). Moreover, a tensile stress is produced on the Polyester which can reach *264 MPa* on the outermost layers.

### 3.4.2.3 Electromagnetic stress

When the magnet is energized, electromagnetic forces are generated which can be determined by evaluating J × B (where J and B are the vectors representing the current density and the magnetic field) [1]. Circumferential stresses for a uniform solenoid can be obtained as:

$$\sigma_\theta = \frac{J\{B_1(r_2^2 + r_1 r_2 - 2r_1^2) + B_2(2r_2^2 - r_1 r_2 - r_1^2)}{6r\ln(\frac{r_2}{r_1})} \quad (3.20)$$

$B_1$ e $B_2$ are the axial component of the magnetic field on the inner and outer radius of the coil. The field values are obtained from the head distribution calculated through an FEA magnetic field analysis. From Fig. 3.13 it is possible to verify that the stress of this nature is directly proportional to the intensity of the magnetic field and the results obtained are perfectly in line in the comparison between the numerical and analytical method.

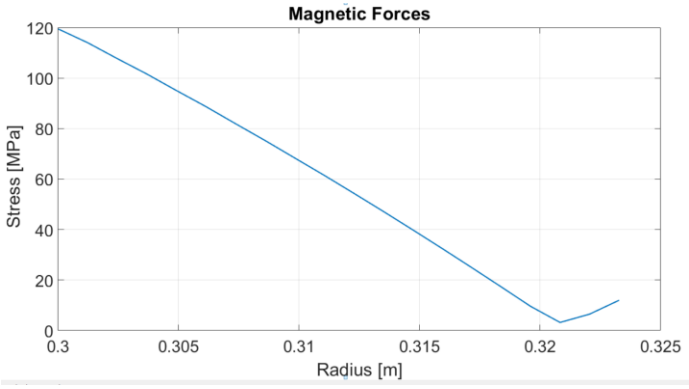


Fig. 3.13. Electromagnetic force depending on the radial distance

Knowing the distribution of the winding tension in each layer, it is possible to control the tension states after cooling and energization by varying the pretensioning on the various layers during the winding phase of the magnet; in particular, increasing the pre-tensioning value where greater compression forces are expected. Therefore, it is also important to verify that the strain and circumferential tension on the wire are below the critical value at any time during the operating states of the magnet. For this purpose, it is useful not to consider Von Mises stress: the composite structure will have locally different states that can be in tension or in compression, which cannot be highlighted by representing the equivalent Von Mises stress. Also, because the Von Mises stress, as a quadratic sum of the stress in three directions, does not allow to derive the direction in which the stresses develop. As a result, circumferential and radial stresses and strains are considered as primary failure criteria for the design and hence. Finally, it is noted that, after the winding operation, the maximum radial stress occurs inside the reel near the mandrel. applying a pretension helps to compensate for the compressive stress created as a result of cooling, it also helps to reduce the stress in the epoxy and reduce the possibility of cracking.

## 3.5 Design of Electric insulation

Voltage in the coil can have fast transients either during normal operating condition (e.g. normal operation of the switches/breakers) or in abnormal operating condition (e.g. faults) and physical phenomena (lightning strikes). The presence of the Chopper connected to the magnet causes an electrical transient due to the commutation [31]. When a voltage surge is applied on the winding the initial distribution of voltage (curve *a* in Fig. 3.14 impulse voltage distribution) on the winding itself depends on capacitances between turns and between turns and ground. Than, a constant value of voltage applied on the magnet eventually leads to a uniform voltage distribution (curve *b).*

In correspondence to a commutation, the chopper imposes a voltage variation between 0 and 750V on the coil terminals; this variation occurs on a microsecond time scale, which is the characteristic switching time of an IGBT. Since there is difference between the initial and final voltage distributions, as shown a transient phenomenon takes place. During this transient period, there is continual interchange of energy between electric and magnetic fields making the transient is oscillatory. The voltage at any point in the winding oscillates about the final voltage value, reaching a maximum as shown by curve c.

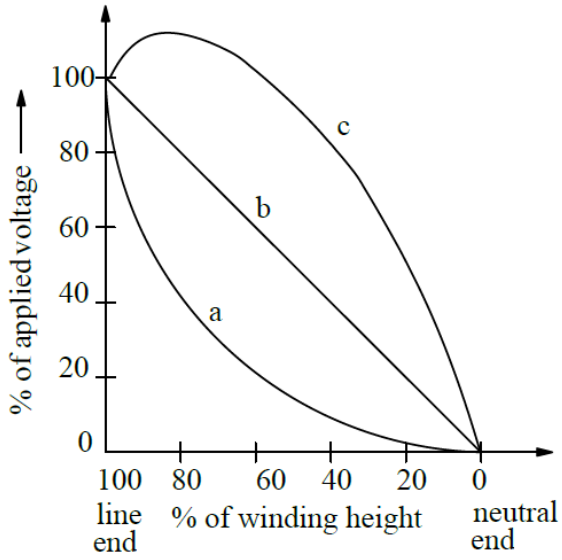


Fig. 3.14 impulse voltage distribution

Due to this pulse, the voltage is not linearly distributed along the turns of the magnet but, rather, it is concentrated on the turns close to the input terminal, thus creating a hot spot of the electric field that could cause the insulation to break. . Insulation failure due to transient overvoltage is a crucial issue to consider during the design phase [20].

### 3.5.1 Coil model

The structure of the coil insulation is the major concern in the superconducting coil design, where it is important for the reliable and economic operation of the entire SMES system. A geometrically large coil makes the design more complex. In order to have complete design of the insulation structure of a winding, the transient voltage stresses of the all subcomponents of the structure must be known. The accurate determination of the impulse voltage distribution in the winding can be obtained using a lumped parameter network model [32]-[33]. In particular, a distributed parametric equivalent circuit model of the winding is introduced. The model consists of inductances mutually coupled, which represent each single turn, and the capacities corresponding to the insulation layers between two adjacent turns or between a turn to ground [34].

The circuital model of the coil is shown in Fig. 3.15. Known the geometric dimensions, it is necessary to first define the following parameters:

- Self-inductance of each turn;
- Mutual inductance for each couple of turns;
- Capacitance between each couple of consecutive turns;
- Capacitance between turns on consecutive layers;
- Capacitances to the ground.

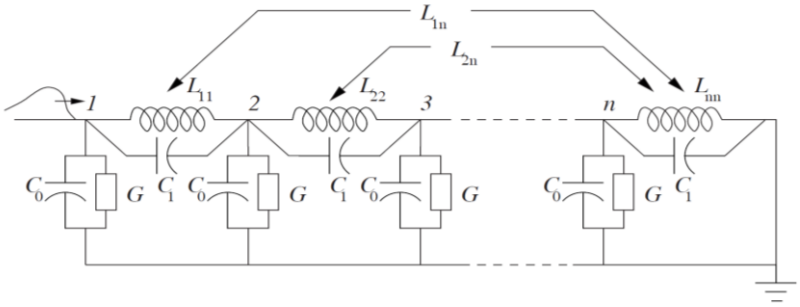


Fig. 3.15 Equivalent electric circuit of the coil

Due to high memory and computing cost, various degrees of simplification are necessary.

### 3.5.2 Numerical procedure

The full model is obtained by considering a circuit representation in which all inductances and capacitances are reported. Nonetheless the voltage distribution on the coil can be accurately modelled obtained with lumped parameters based on the assumption that the dielectric constant of the insulating material does not vary with frequency and that a small resistance value represents the skin effect and eddy current losses.

The equivalent circuit of a winding consists of a finite number of sections having elements such as the shunt capacitance $C_0$, the series capacitance $C_1$, the self-inductance $L_{ii}$, the mutual inductance $L_{ij}$ and the shunt conductance *G*. The impulse voltage distribution of a winding is calculated using a state space model of the lumped parameter network as described below. The equation for the network is formulated:

$$C\ddot{y}(t) + G\dot{y}(t) + \Gamma y(t) = 0 \tag{3.21}$$

Where *C* is nodal capacitance matrix, *G* is the nodal conductance matrix, Γ is the nodal matrix inverse inductances and *y* is the output vector of node voltages.

### 3.5.2.1 Self and mutual inductance calculation

Based on geometric parameters inductance calculation can be written as follows:

$$L = \mu_o R \ln\left(\frac{8R}{R1} - 2\right) \tag{3.22}$$

$$lnR1 = \frac{1}{2}ln(a^2 + b^2) - \frac{b^2}{12a^2}ln\left(1 + \frac{a^2}{b^2}\right) - \frac{a^2}{12b^2}ln\left(1 + \frac{b^2}{ba^2}\right) + \frac{2b}{3a}tan^{-1}\frac{a}{b} + \frac{2a}{3b}tan^{-1}\frac{b}{a} - \frac{25}{12} \tag{3.23}$$

Where *a* and *b* are respectively the height and the width of the tape. Mutual inductance between two circular filaments is calculated by using the formula:

$$L_{ab} = \frac{2\mu_0}{k}N_a N_b\sqrt{R_a R_b\left\{\left[1 - \frac{k^2}{2}\right]K(k) - E(k)\right\}} \tag{3.24}$$

$$k = \sqrt{\frac{4R_a R_b}{(R_a + R_b)^2 + d^2}}$$

Where $R_a$ and $R_b$ are the radius of the mutually coupled turns, *d* is their distance, and *K(k)* and *E(k)* are the complete elliptic integrals of the first and second kind. The branch inductance matrix ($L_b$) and the incidence inductance matrix $Q_L$ of the order (*n* x *n)* can be given as:

$$L_b = \begin{bmatrix} L_{11} & \cdots & L_{1n} \\ \vdots & \ddots & \vdots \\ L_{n1} & \cdots & L_{nn} \end{bmatrix} \tag{3.25}$$

$$Q_L = \begin{bmatrix} 1 & 0 & \ldots & 0 \\ -1 & 1 & \ldots & 0 \\ \ldots & \ldots & \ldots & 0 \\ 0 & 0 & -1 & 1 \end{bmatrix} \tag{3.26}$$

And the matrix *L*:

$$L = Q_L L_b^{-1} Q_L^T \tag{3.27}$$

### 3.5.2.2 Capacitance calculation

Based on the geometric entities, series capacitance between turns, shunt capacitance between axially separated turns, and turn to ground capacitance of layers can calculate easily and accurately by using the parallel plate formula:

$$C_t = \frac{\varepsilon_0 \varepsilon_p A}{t_p} \tag{3.28}$$

Where $\varepsilon_0$ is the dieletric constant of the vacuum, $\varepsilon_p$ is the permittivity of the insulation and $t_p$ is the insulation thickness. To obtain a reduction in the calculation time the capacities between adjacent coils on two different layers have been simplified [35]; the simplification is possible because the shunt capacitance can be divided into two capacities of twice the initial value connected in series as shown in Fig. 3.16

The central point between these two capacitances is at the same potential as the node connecting the two adjacent layers, it is therefore possible to simplify this capacity network between turns on adjacent layers, by adding an additional term to the capacities between two consecutive turns on the same layer [36].

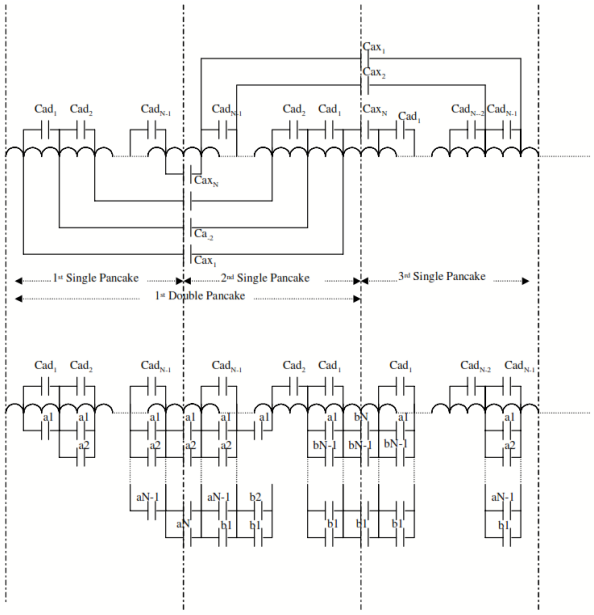


Fig. 3.16. Derivation of equivalent series capacitance for three layers. a1=(2N-1)C_ax1, b1=(2N-1)C_axN, a2=(2N-3)C_ax2, b2=(2N-3)C_(axN-1), a3=(2N-5)C_ax3, b3=(2N-5)C_(axN-3), aN-1=3C_(axN-1), bN-1=3C_ax2, aN=1C_axN, bN=1C_axN

There are 2*n* capacitive branches in the network, therefore, the size of the branch capacitance matrix ($C_b$) is 2n x 2n. it can be written as:

$$C_b = \begin{bmatrix} C_0 & 0 & \dots & 0 \\ 0 & C_1 & \dots & 0 \\ \dots & \dots & \dots & 0 \\ 0 & 0 & 0 & C_1 \end{bmatrix} \quad (3.29)$$

Where $C_0$ and $C_1$ are the capacitance as shown in Fig. 3.15. the corresponding incidence matrix $Q_c$ (*n* x *2n)* is:

$$Q_L = \begin{bmatrix} 1 & 1 & 0 & 0 & 0 & 0 \\ 0 & -1 & 1 & 0 & 0 & 0 \\ 0 & 0 & 0 & 0 & 0 & 0 \\ \dots & \dots & \dots & \dots & \dots & \dots \\ 0 & 0 & 0 & 1 & 1 & 0 \\ 0 & 0 & 0 & -1 & 1 & 1 \end{bmatrix} \quad (3.30)$$

So we can obtain C:

$$C = Q_c C_b^{-1} Q_c^T \quad (3.31)$$

### 3.5.3 State space model

The state space model of the equation ( 3.21) is:

$$\dot{X}(t) = AX(t) + Bv(t) \quad (3.32)$$

$$y(t) = FX(t) + Dv(t) \quad (3.33)$$

Where $X(t)$ is the vector of state variables, *A* and *F* are matrices of constant coefficients, *B* and *D* are column matrices of constant coefficients, $v(t)$ is the input vector of the applied impulse voltage and $y(t)$ is the output vector of node voltage.
Now, rearranging the equation ( 3.21) in order to take into account the input node, it is possible to rewrite:

$$\ddot{y}(t) + C^{-1}G\dot{y}(t) + C^{-1}\Gamma y(t) = C^{-1}C_k\ddot{v}(t) + C^{-1}G_k\dot{v}(t) + C^{-1}\Gamma_k \mathrm{v}(t) \quad (3.34)$$

Where the matrices with *k* are the coefficient matrices with the *k-th* column of the input node removed. Applying the state space model at the equation ( 3.34) with:

$$\alpha_1 = C^{-1}G \qquad \beta_1 = -C^{-1}(G_k - GC^{-1}C_k)$$
$$\alpha_2 = C^{-1}\Gamma \qquad \beta_2 = -C^{-1}(\Gamma_k - GC^{-1}(G_k - GC^{-1}C_k) - \Gamma C^{-1}C_k$$

The constant coefficient matrices are obtained as:

$$A = \begin{bmatrix} 0 & I \\ -\alpha_2 & -\alpha_1 \end{bmatrix} \qquad B = \begin{bmatrix} \beta_1 \\ \beta_2 \end{bmatrix}$$

$$F = [I \quad 0] \qquad D = -C^{-1}C_k$$

This analysis has converted the original second order circuit to an equivalent first order state space system.

### 3.5.4 Voltage profile and distribution of electric stress

Once the circuit has been defined, the equivalent circuit can be solved in the MATLAB environment, by calculating the capacitance and inductance matrices according to the reported relationships by using a state space model to solve the electrical circuit [33]. In the model the distance between two turns, which defines the thickness of the insulation, consists of the thickness of the polyester in which the tape is wrapped and the thickness of the fiber glass interlayer. By adopting a high-speed switching device, such as the IGBT, the voltage applied to the magnet is a square wave, with the rise and fall time of $0.1\ \mu s$. The voltage distribution on the turns during the switching of the chopper is shown in Fig. 3.17.

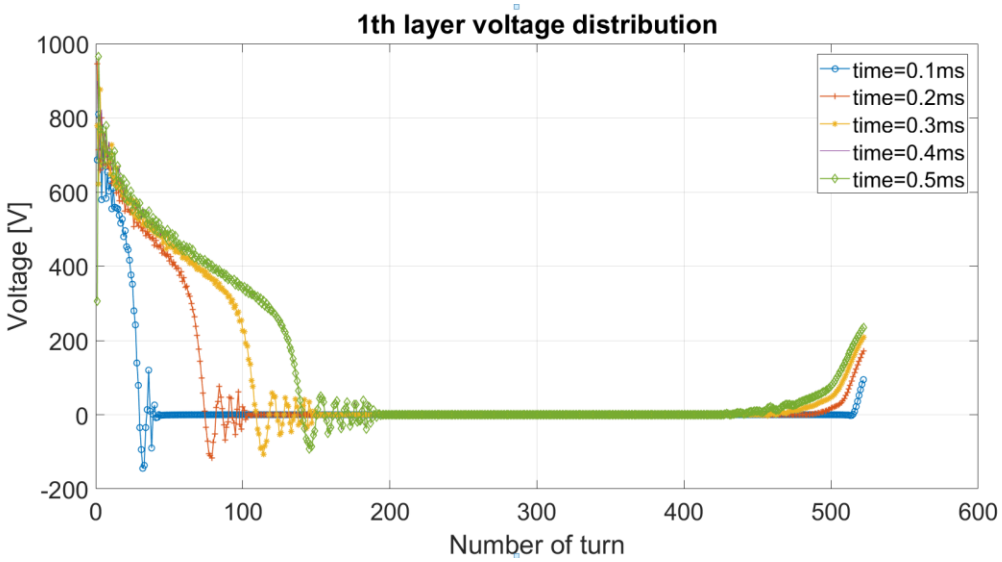


Fig. 3.17 Electric potential distribution on the turns

In this case it can be seen that the very fast transient period in which the switching phase of the chopper takes place produces a complex evolution of the voltage distribution on the coil: the voltage drop is mainly concentrated in the first 15 turns. This behavior is due to the effect of the capacities of the magnet in the dynamic behavior which gradually reduces,

bringing the voltage between the two terminals back to a linear distribution. This means that approximately the entire voltage of the coil terminals exists between the upper turns of the first layer and the corresponding turn of the adjacent second layer. This could cause an overload on the electrical insulation between the first and second layers.

A 2-D finite element model developed in ANSYS is used to obtain, known the distribution of the potential on each turn, the map of the electric field during the commutation. furthermore, the maximum excitation voltage used in the calculation corresponds exactly to the voltage of the DC bus [30].

The distribution of the excitation voltage that comes from the previous calculation is applied following the spatial arrangement of the turns starting from the internal radius, from top to bottom for the first layer, from bottom to top for the second likely to the other layers [37]. The relative electric field distribution on the first turn (the most stressed) is shown in Fig. 3.18

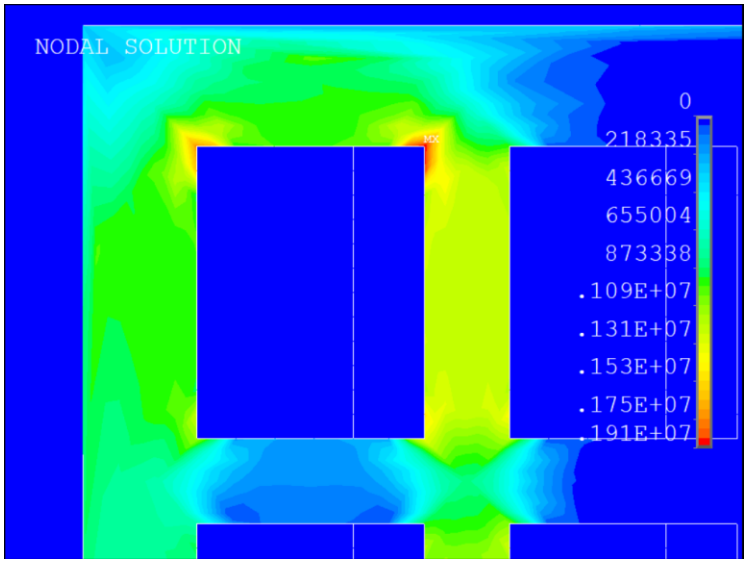


Fig. 3.18 Electric field near the first turn of the coil

As can be seen Fig. 3.18, the peak value of electric field intensity (*1.9 kV-mm*) occurs in the corner of the conductor inside the insulating layer between the two adjacent head turns for the first two consecutive layers; for this reason, the insulation of the intermediate layer is very useful for increasing the distance between the two coils, avoiding an electrical fault.

# 4 Thermal analysis

The main aims of a thermal analysis of the SMES system:

- The thermal design of the Cryocooler with the evaluation of the powers exchanged by the various components;
- The calculation of the temperature increase in each cycle.

Evaluation of the thermal load due to radiation, conduction through the supports, current leads and AC loss is presented. Attention is devoted at explaining the assumptions and the criteria used of the calculation of the AC loss during charge/discharge operation of the SMES coil at actual power rate. The complexity of the cryogenic system, given by the non-linearity of the thermal behavior of the components and by the transience of the phenomena, makes it necessary to simplify the problem. As first approximation, therefore, we can consider a stationary case that allows us to evaluate, through a balance, the exchanged powers. Thereafter, transient thermal inputs are introduced (AC losses, eddy current, magnetization) for a more effective definition of the temperature increases related to the dynamic behavior of the system.

## 4.1 Heat contributions and evaluation of thermal load

In order to estimate thermal powers exchanged between the components of the SMES system and the corresponding temperatures considering an equivalent thermal circuit is used. The analogies between heat exchange phenomena and electrical circuits are used, and in particular the formal correspondence between thermal power and electric current and Fourier's and Ohm's law. According to this analogy, the amount of heat exchanged in the unit of time, i.e. the thermal power, is directly proportional to the temperature difference that causes the heat exchange.

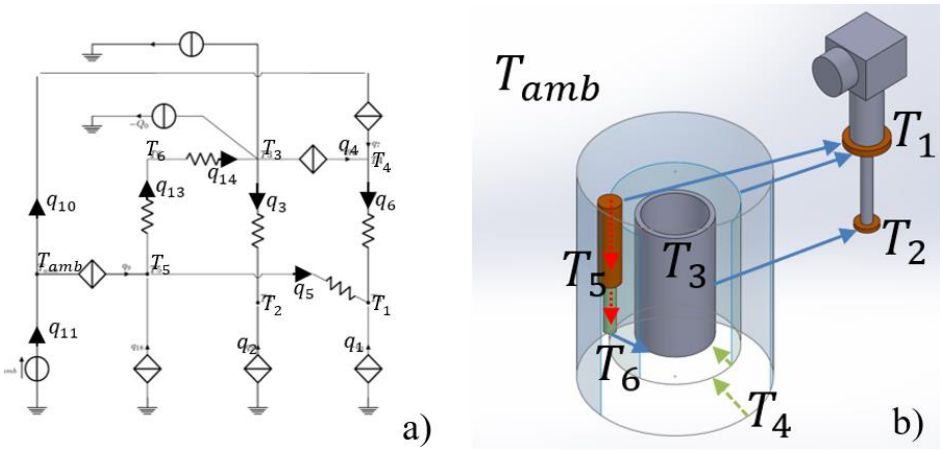


Fig. 4.1 equivalent thermal circuit

Referring to the simplified diagram shown in Fig. 4.1b which shows the components of the SMES system, an equivalent non-linear thermal circuit is obtained (Fig. 4.1a) in which the node potentials represent the temperatures of the following components:

- /First stage *cryo-cooler* (*T1*);
- Second stage *cryo-cooler* (*T2*);
- Magnet (*T3*);
- Thermal shield (*T4*);
- 1° stage Cu *current lead* (*T5*);
- 2° stage Cu *current lea*d (*T6*).

The currents in the branches represent the thermal powers exchanged between the components:

- Cooling power of the first stage of *cryo-cooler* (*Q1*);
- Cooling power of the second stage of *cryo-cooler* (*Q2*);
- Magnet and second stage of *cryo-cooler* (*Q3*);
- Radiation power from thermal shield to magnet (*Q4*);
- *Current lead and first stage of cryo-cooler* (*Q5*);
- Thermal shield and first stage of *cryo-cooler* (*Q6*);
- radiation power from external case to thermal shield (*Q7*);
- convection between thermal shield and magnet (*Q8*);
- convection between external case and thermal shield (*Q9*);
- conduction through the support bars of the magnet (*Q10*);
- current lead heat generation(*Q11*);
- current lead HTS portion (*Q12*);
- conduction through the copper braid (*Q13*);
- joule heat on the copper braid (*Q14*);

In particular, the temperatures of the cryo-cooler stages are a function of the extracted thermal powers *T1* = f (*Q1*, *Q2*) and *T2* = f (*Q1*, *Q2*) according to the characteristic map of the reference cryo-cooler (Fig. 4.2).

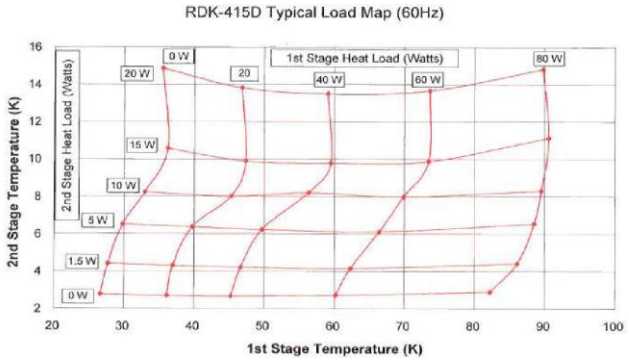


Fig. 4.2. Cryo-cooler map

The power extracted from the magnet towards the II stage of the cryo-cooler and extracted from the thermal shield and the copper part of the current leads towards the I stage of the cryo-cooler flow by conduction through copper braids by conduction according to the law:

$$Q = \frac{A}{L} k\,\Delta T \tag{4.1}$$

*A* is the cross section of the conductor, *L* is its length and *k* is the thermal conductivity, supposed constant in the temperature range considered. The conduction power through the support bars depends on the weight of the magnet and the size of the bars, according to the formula:

$$Q = \frac{P}{\sigma L} k\,\Delta T \tag{4.2}$$

*P* is the weight of the magnet, $\sigma$ is the elastic modulus of the bars material the parameters of the conduction power are reported in Table 4.1. With regard to the powers by irradiation between the heat shield and the magnet, and the external shield and the heat shield, the reference formula is shown below

$$Q = \frac{\sigma A_1 (T_2^4 - T_1^4)}{\frac{1}{\epsilon_1} - \frac{A_1}{A_2}(\frac{1}{\epsilon_2} - 1)} \tag{4.3}$$

$\sigma$ is the stephan-Boltzmann coefficient, *A* is the surface exposed to the radiation $\epsilon$ is the emissivity. It is considered that the external surfaces of the magnet and the thermal shield are coated with multilayer Mylar. Also for the radiation power the parameters are reported Table 4.1. Convection powers are instead calculated using the formula corresponding to the molecular convection case for the degree of vacuum that is reached within the cryogenic system:

$$Q = 2.426e-4 A_1 \frac{\alpha_1 \alpha_2}{\alpha_2 + \frac{A_1}{A_2}(1-\alpha_2)\alpha_1} \frac{\gamma+1}{\gamma-1} \frac{p}{\sqrt{MT}} (T_1 - T_2) \tag{4.4}$$

$$\alpha = \frac{T_i - T_e}{T_i - T_w} \tag{4.5}$$

*A* is the surface, *p* is the pressure in *uPa*, $\gamma$ is the specific heat ratio (cp/cv), *M* is the molecular weight of gas. the power of the current leads, considering that they are sized in order to minimize the thermal load, is calculated with reference to the formula

$$Q = 2I\sqrt{L\frac{T_2^2 - T_1^2}{2}} \quad (4.6)$$

*I* is the current, *L* is the Wiedemann-Franz-Lorenz constant (2.44e-8WΩ/K2). Whereas for the HTS part it is considered that this portion is made of silver stabilized BISCCO with a steel coating so that the power is transmitted by conduction in the conductive materials

Table 4.1

THERMAL PROPERTIES OF THE SYSTEM

| Conduction parameters | |
|---|---|
| Copper thermal conductivity 17K | *1.28e3 [W/mK]* |
| Cross section | *2e-4 [$m^2$]* |
| Length (Q3) | *0.6 [m]* |
| Length (Q5) | *0.2 [m]* |
| Length (Q6) | *0.3 [m]* |
| Length (Q13) | *0.1 [m]* |
| Length support bar | *2.5 [m]* |
| Magnet weight | *1735 [kg]* |
| Elastic modulus stainless steel | *160 [MPa]* |
| **Radiation parameters** | |
| Magnet surface | *2.82 [$m^2$]* |
| Thermal shield surface | *4.31 [$m^2$]* |
| External case surface | *6.21 [$m^2$]* |
| Mylar emissivity | *0.02* |
| Steel emissivity | *0.16* |
| **Convection parameters** | |
| Accommodation factor (alpha) | *1* |
| Molecular weight residual gas | *4 [g/mol]* |
| Specific heat ratio | *1.66* |
| pressure | *0.075 [micronHg]* |

The solution of the equivalent thermal circuit is represented by a list of temperatures in each node and power exchanges between the components:

Table 4.2

THERMAL CIRCUIT RESULTS

| | |
|---|---|
| first stage *cryo-cooler* | *85.6443 [K]* |
| Second stage *cryo-cooler* | *5.226 [K]* |
| Magnet | *12.7782 [K]* |
| Thermal shield | *129.1494 [K]* |
| First stage current lead | *126.1844 [K]* |
| HTS current lead | *12.8324 [K]* |
| Power extracted by first stage *cryo-cooler* | *83.4522 [W]* |
| Power extracted second stage *cryo-cooler* | *3.2222 [W]* |
| Magnet to second stage *cryo-cooler* | *3.2222 [W]* |
| Radiation from thermal shield to magnet | *0.8324 [W]* |
| Current lead to first stage of *cryo-cooler* | *48.6482 [W]* |
| Thermal shield to first stage of *cryo-cooler* | *34.8041 [W]* |
| Radiation from external case to thermal shield | *35.6326 [W]* |

## 4.2 Calculation of AC losses during SMES operations

Particular attention is dedicated to the evaluation of AC losses during the charge / discharge phase of the SMES. The calculation of losses is carried out using THELMA, a model developed as part of an Italian initiative, mainly aimed at analyzing nuclear fusion problems [38]. This model considers a system consisting of N elements (CE) of a section of superconductor cable (SC) that can be wound to make a winding. The power law is assumed to define the characteristic of the superconductor, that is

$$\boldsymbol{E}(r) = E_0 \left(\frac{J}{J_c}\right)^n \frac{\boldsymbol{J}(\boldsymbol{r})}{J} \tag{4.7}$$

the electric field can be derived by the magnetic vector potential as follow:

$$\boldsymbol{E} = -\nabla V - \frac{\partial \boldsymbol{A}}{\partial t} \tag{4.8}$$

The unknowns of the problem are the current values in each CE. A generator is connected to the two terminals of the cable which supplies the current *I* as a function of time and, moreover, the external magnetic field and the field produced by the conductor itself are considered. The geometry of the cable is defined with respect to the axial coordinate system as shown in Fig. 4.3, in which all elements can exchange a current in the transverse direction through the matrix in which they are immersed.

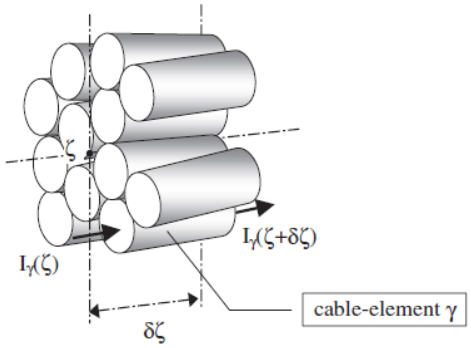


Fig. 4.3. schematic view of the wire

The 3D model is obtained by extruding the wire geometry along the helix of the winding and with a rotation around the helix in order to consider the filament twisting. The current is assumed to be uniformly distributed in the cross section of each CE and its value depends on the axial coordinate and time. The equations describing the current distribution are derived from the Faraday law, by means of charge conservation law on each cross section [39]. It is usually not necessary to consider the magnetic coupling between each CE of the cable segment; the coupling coefficients of two CEs more far than a maximum distance can be neglected. Furthermore, in order to simplify the model, it is assumed that the vector

potential due to the transverse coupling currents flowing through the matrix is negligible compared to that one due to the longitudinal currents flowing in the conducting filaments. This implies that the transverse currents are not part of the state variables , reducing the size of the solving system. To carry out the calculation of the conductance between the filaments in the transversal direction, a 2D model of the wire (filaments + copper tape) is introduced while the matrix is not directly introduced into the geometry of the model as shown in Fig. 4.4.

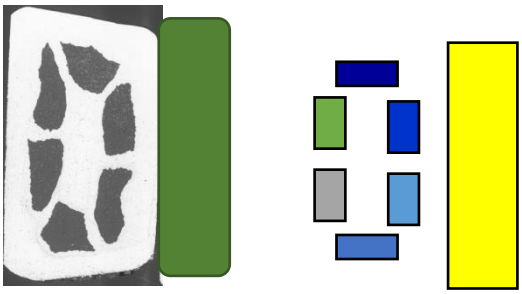

Fig. 4.4. Geometrical model of $MgB_2$ wire with rectangular section

### 4.2.1 Mathematical model

The finite element model requires a subdivision of $N_S$ elements along the length of the cable for every $N_F$ filaments. The unknowns of the discretized problem are $N_C = N_F N_s$ currents of transverse faces shared by two elements or connecting the coil to the current supply, defined as:

$$\boldsymbol{I}(x_h, t) = [I_1(x_h, t), \dots, I_{NF}(x_h, t)]^T \quad (4.9)$$

$$\boldsymbol{I}(t) = [\boldsymbol{I}^T(x_1, t), \dots, \boldsymbol{I}^T(x_{NS}, t)]^T \quad (4.10)$$

Faces corresponding to the same *x* coordinate form a cross section of the cable, hence:

$$\sum_{k=1}^{N_F} I_k(x_h, t) = I_{coil}(t) \qquad h = 1, \dots, N_s \quad (4.11)$$

A double set of points is also introduced to discretize the problem. Between each pair of longitudinally consecutive problems another series of points is interposed which defines a transverse problem in which the current flows from one element to another. The elements can exchange current in the transverse direction through the matrix material, so that longitudinal current $I_k$ of the filament *k* at coordinate *x* and the transverse current $K_k$ per unit of length of filament *k* at coordinate *x*, are:

$$I_k(x,t) = \int_{S_k} \boldsymbol{J}.\boldsymbol{n}\, dS \qquad (4.12)$$

$$K_k(x,t) = \frac{1}{dx}\int_{S_k} \boldsymbol{J}.\boldsymbol{n}\, dS \qquad (4.13)$$

Where $\boldsymbol{J}$ is the current density through the filament and $\boldsymbol{n}$ is the direction perpendicular to the cross section. For the law of the charge conservation the derivative of the longitudinal current corresponds to the transverse current.

As previously said the *A-v* formulation is used for expressing the electric field at any point of the conducting domain. The magnetic vector potential is expressed as the sum of the contribute due to currents of the discretized domain and the contribute due to the external current. The latter is produced by the currents flowing in the part of the coil not included in the discretization, and is expressed as:

$$\boldsymbol{A^{ext}}(\boldsymbol{r},t) = \frac{\mu_0}{4\pi}\int_{\tau coil-\tau fil} \frac{\boldsymbol{J}(\boldsymbol{r}',t)}{|\boldsymbol{r}-\boldsymbol{r}'|} d^3r' \qquad (4.14)$$

The contribute to the conducting elements, instead, can be simplify assuming that the vector potential due to the transverse coupling currents flowing through the matrix is negligible with respect to the one due to currents flowing in the conducting filaments and this is a suitable approximation in problems where a dominant direction of current exists. This contribute can be expressed as:

$$\boldsymbol{A^J}(\boldsymbol{r},t) = \frac{\mu_0}{4\pi}\int_{\tau fil} \frac{\boldsymbol{J}(\boldsymbol{r}',t)}{|\boldsymbol{r}-\boldsymbol{r}'|} d^3r' \qquad (4.15)$$

To solve the transversal problem along a transverse path connecting two CEs of the same section, the conductances between each pair of CEs of a section are calculated, as schematically represented in Fig. 4.5. Graphical representation of the discretization of the problem

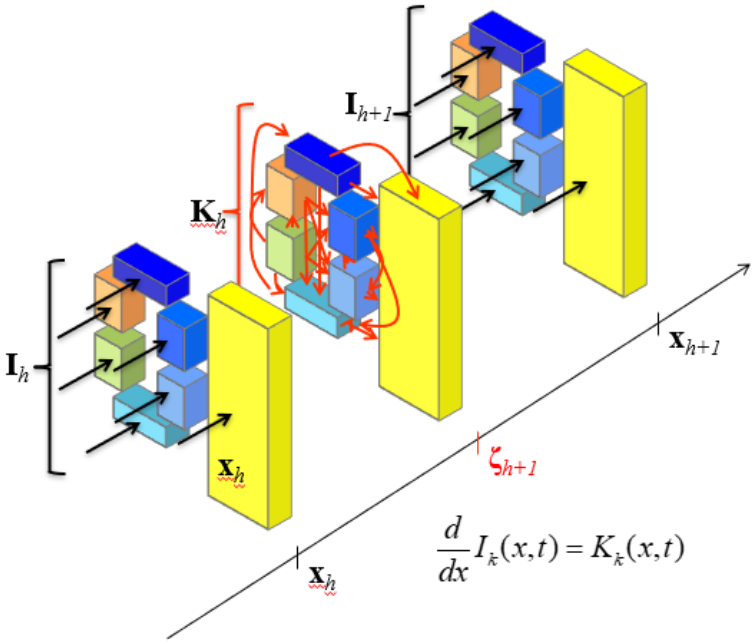


Fig. 4.5. Graphical representation of the discretization of the problem

If all the transverse conductance are different from zero, the conductance matrix is dominant diagonal and therefore invertible. By introducing a conductance matrix of the CEs, it is possible to calculate the transverse currents as a function of the node potentials which represent the elements. In fact, considering a pair of *n* and *m* nodes:

$$K_{nm}(x_h) = g_{nm}(x_h)(-\sum_{j=1}^{Ns}\sum_{k=1}^{Nf} m^t_{mn,k,j}(x_h)\frac{d}{dt}I_k(x_j,t) + (v_m(x_h) - v_n(x_h)) \qquad (4.16)$$

$$K_m(x_h) = \sum_{n=1}^{Nf} K_{nm}(x_h) = \frac{d}{dt}I_k(x_h,t) \qquad (4.17)$$

*Kmn* is the transversal current flowing between two CE of the same cross section, $v_m(x_h) - v_n(x_h)$ is the voltage drop between two CE, and $\frac{d}{dt}I_k$ is the derivative of longitudinal current. $m^t_{mn,k,j}$ is the mutual inductance between the elements *m* and *n* along the section *k,j* of the filament. $g_{nm}$ is the conductance between two elements on the same cross section and it is calculated using commercial software, including the resistivity of the materials of which the matrix is composed ($\rho_{monel}(20K) = 4{,}2e^{-7}\Omega m$; $\rho_{nickel}(20K) = 11e^{-9}\Omega m$) The conductance between each pair of CE is obtained by applying a unit potential value on one CE and a zero

potential on the others, as shown in Fig. 4.6:

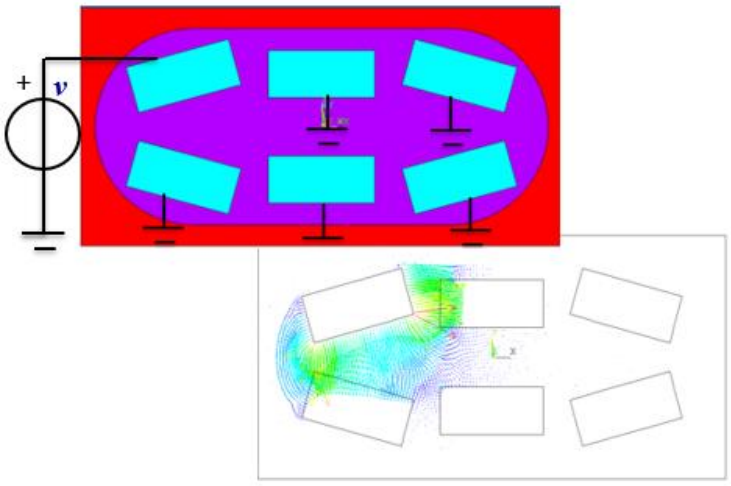


Fig. 4.6. Current distribution for conductance calculation

. The total longitudinal current carried by the elements in any x coordinate must coincide with the total current of the coil. To simplify the resolution of the problem the longitudinal current of the element at coordinate x is expressed as the sum of the "uniform" current plus a "deviation" current with respect to it. The so-called uniform current is obtained from the total current on the coil assuming a uniform distribution of the current density $I_h(t) = \frac{Icoil(t)}{\sum S_k} S_k$. By assembling the transverse voltage balances referring to all filaments but the last we obtain from (4.16) the system :

$$\boldsymbol{K_h}' = \boldsymbol{g_h}'(-\sum_{j=1}^{Ns} \boldsymbol{m}_j^t \frac{d}{dt}\boldsymbol{I}_j - \boldsymbol{u}_h \frac{d}{dt} I_{coil} + \boldsymbol{v_h}' - v_{Nf}) \tag{4.18}$$

Where $\boldsymbol{g_h}$ is the matrix of the conductances, $\boldsymbol{m}_j^t$ are the matrices of the mutual inductances of a j-th section of the domain, $\boldsymbol{u}$ is the inductance of the cable and $\boldsymbol{v}_h$ are the vectors of the node potentials. Finally, by using charge conservation, the potentials at all nodes of each section but the las are related to the longitudinal current as:

$$\boldsymbol{v_h}' = \boldsymbol{g_h}^{-1} d_h(\boldsymbol{I}_{h+1} - \boldsymbol{I}_h') + \sum_{j=1}^{Ns} \boldsymbol{m}_j^t \frac{d}{dt}\boldsymbol{I}_j + \boldsymbol{u}_h \frac{d}{dt} I_{coil} + \boldsymbol{1} v_{Nfh} \tag{4.19}$$

Two further nodes are added for calculating the derivative of voltage at the input and output sections of the discretized model; also, a resistive model of terminations is added in order to calculate the potential of the additional nodes at the input and output sections:

$$\boldsymbol{v}_1 - \mathbf{1}v_0 = -\text{diag}(\boldsymbol{R}_{in})\boldsymbol{I}_1 \qquad \boldsymbol{v}_{NS-1} - \mathbf{1}v_{NS} = -\text{diag}(\boldsymbol{R}_{out})\boldsymbol{I}_{NS-1} \tag{4.20}$$

Where $v_0$ is the voltage at the input node, $\boldsymbol{R}_{in}$ $\boldsymbol{R}_{out}$ are the resistances at the input and output of the model. The system can be solved with the balance on the longitudinal currents:

$$\boldsymbol{f}_h(I_h) = \sum_{j=1}^{Ns} \boldsymbol{m}_{hj}\frac{d}{dt}\boldsymbol{I}_j - \boldsymbol{u}_h\frac{d}{dt}I_{coil} - \boldsymbol{p}_h d_h(\boldsymbol{v}_{h+1} - \boldsymbol{v}_h) \tag{4.21}$$

The last of the longitudinal voltage balance equations of each sections is used for eliminating the potential $v_{Nf}$ from the corresponding dual sections in (4.19).

The longitudinal current of element at coordinate *x* is expressed as the sum of the constant current plus a deviation current with respect to it:

$$I(x_h, t) = I_h^c(t) + i_h(x_h, t) \tag{4.22}$$

Where $I_h^c$ is an assigned, time dependent, term of current and $i_h$ is the deviation current at coordinate *x* of element *k*. By replacing this new form of longitudinal current in the voltage balance equation (4.21), it is possible to make the matrix of the coefficients of the currents sparse. Also, if the distance between two blocks is greater than a certain value, we ignore the corresponding blocks of the coefficient matrix. Long-term interactions are not neglected but considered, in a simplified form, through the additional term of the current.

## 4.2.2 Numerical results

The power required by the system can be transferred from the SMES to the network in both directions thanks to the use of two converters. the SMES is able to deliver a power of 200kW. The current profile during a cycle at the maximum power is shown in Fig. 4.7, and at the state of maximum charge a current of 467 A can be delivered. The inductance of the winding is 6.8 H.

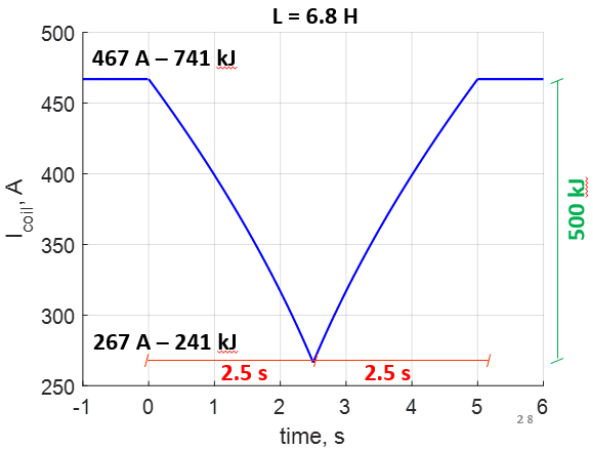

Fig. 4.7. Current time profile

In order to reduce the calculation times, only 10 turns of the coil are modeled for each simulation; A total of 20 cases are simulated, thus taking into account the central area and the one at the end of each layer. In particular, a conductor length of 19 m was considered with 42 elements for twist pitch (1323 elements in total) Fig. 4.8. The convergence analysis shows that the same results are obtained with a greater number of elements and with a greater number of turns. The complementary part of the coil acts on the computational domain as the source of the external magnetic field. The current distribution at the end of the charging time on the cable elements in the considered length (from $x = 9\ m$ to $x = 10.9\ m$) is shown in Fig. 4.7. The sum of the filament currents for each axial coordinate corresponds to the operating current, but the coupling currents cause variations on the length considered with values between -175 A and 190 A.

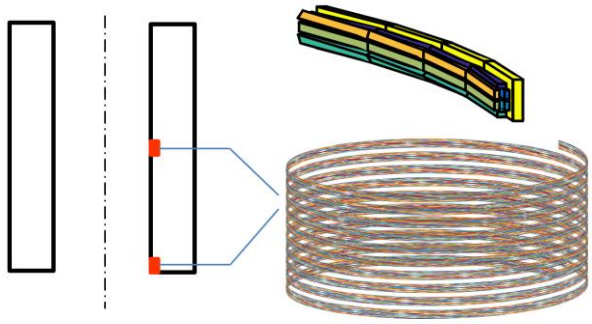

Fig. 4.8. Domain of THELMA evaluation

the following are the current profiles in the CEs over a length of 1.8m. in particular, the results are obtained from the simulation of Layer 1 in the tension zone of the magnet and the profiles reported refer to the time instants $t = 100\ s$, $t = 101\ s$, $t = 103\ s$, $t = 105\ s$ *and* $t = 155\ s$ in Fig. 4.9.

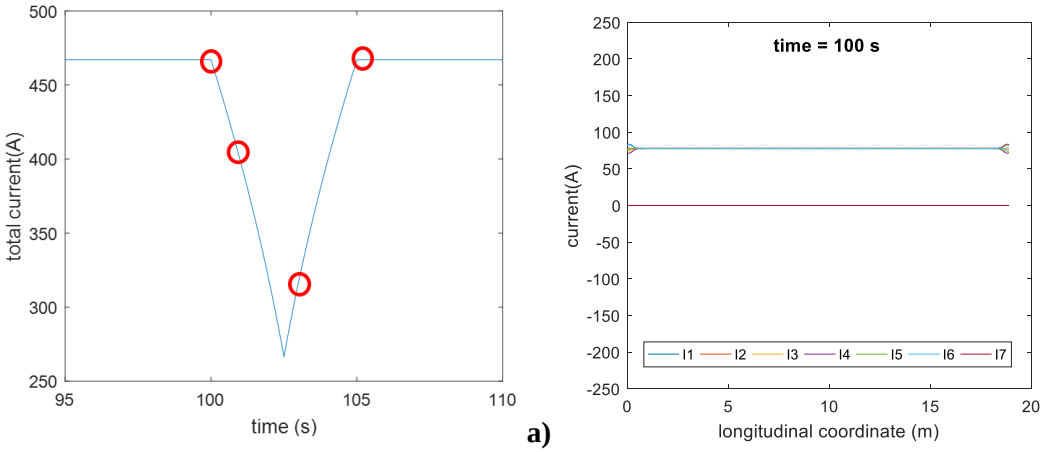


**a)**

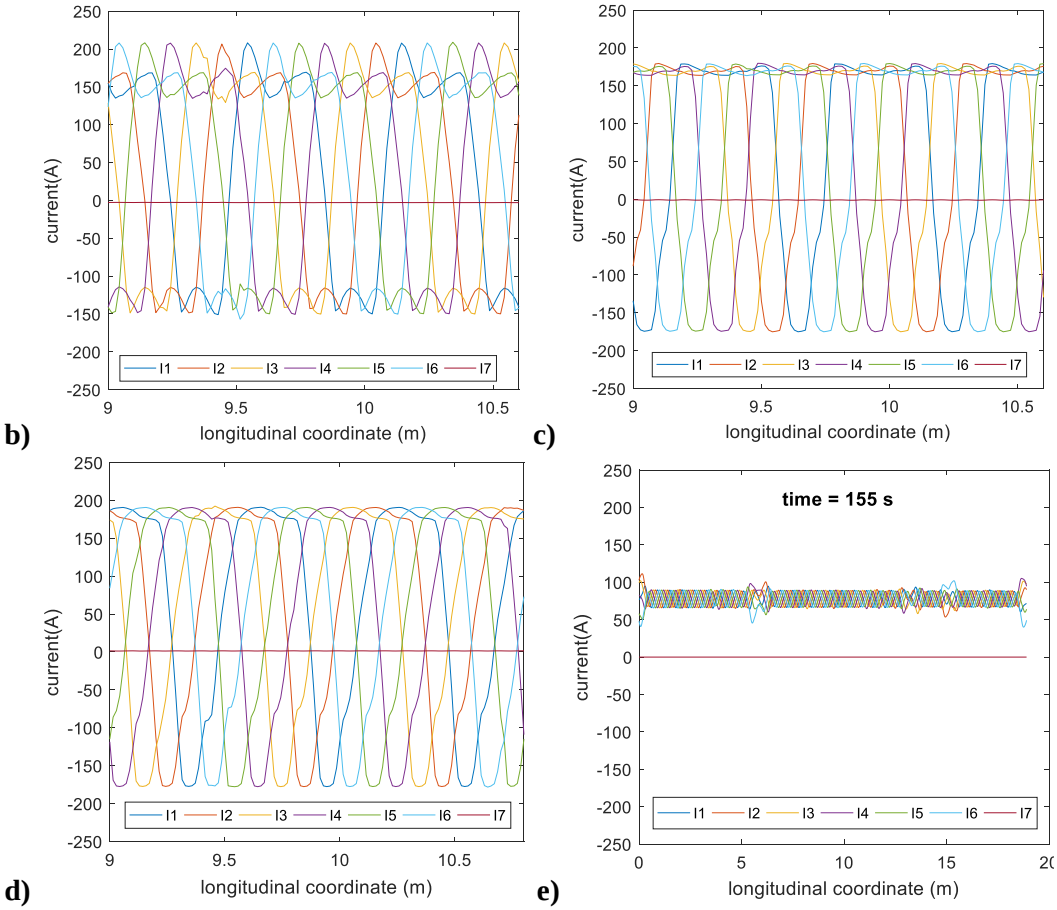


Fig. 4.9. Current profile during charge/discharge a) t = 100 s b) t = 101 s c) t = 103 s d) t = 105 s e) t = 155 s

coupling current on the CEs become negligible again following a relaxation period of 50s. The oscillation of the current during charging / discharging causes variations in the magnetic field that generate AC losses. The magnetic field distribution is shown in Fig. 4.10, and also the operating current and critical current profiles on a filament are shown. It can be seen that the operating current is above the critical one. This produces an increase in the electric field and consequently in the resistivity within the superconducting filaments. Joule losses within superconducting filaments and coupling losses within the matrix are considered.

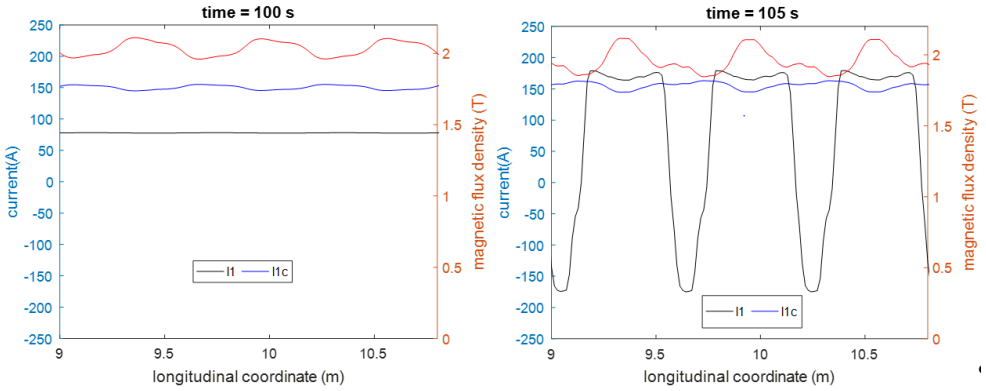


Fig. 4.10 Magnetic field, critical current and operating current on filament

The power loss profile of the central part of the cable is shown in Fig. 4.11:

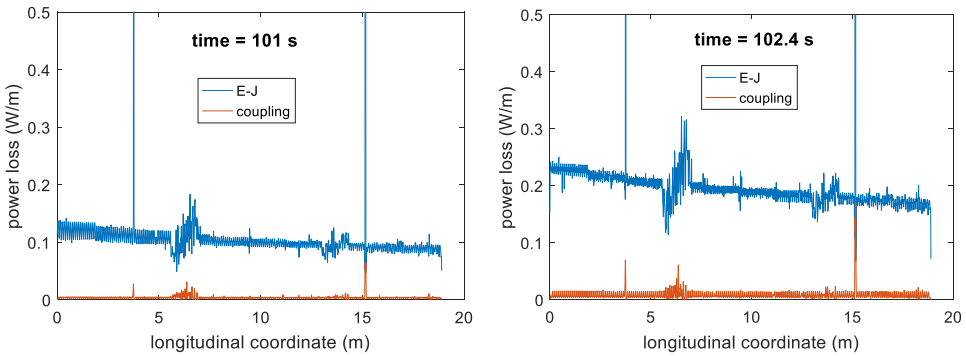


Fig. 4.11. Losses distribution depending on time

Fig. 4.12 shows the time distribution of AC and coupling losses for a turn of layer 1 in the terminal zone of the magnet.

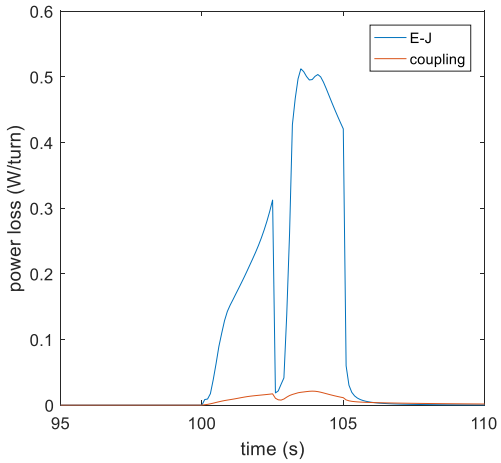


Fig. 4.12. Losses per turn in the first layer at the top section of the magnet

the coupling losses are negligible compared to the losses in superconducting filaments. The average value of the losses per loop in the charging and discharging phase is *155mW*. From all the loss profiles obtained from the various simulations distributed in the different areas of the magnet it is possible to obtain a map of the distributions of energy generated on the section of the magnet. The map in Fig. 4.13 was obtained as a planar interpolation of the power values on the individual turns, therefore each node of the map shown contains the value relating to the turns in the corresponding position.

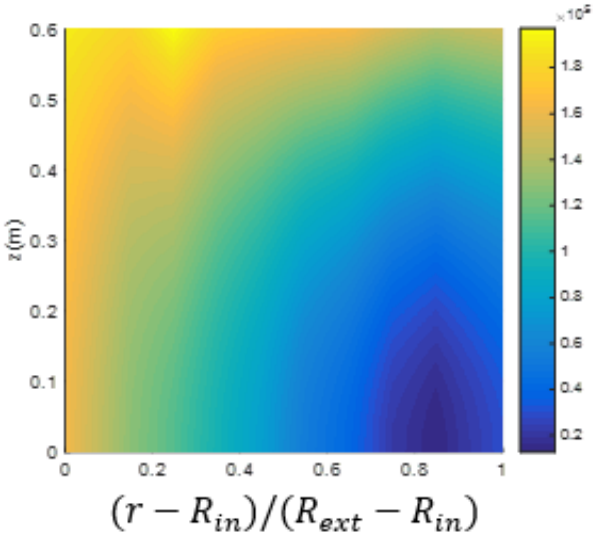


Fig. 4.13 Losses distribution per volume (J/m3) on the cross section of the magnet in a charge/discharge cycle

In the internal part of the winding the losses are greater due to the greater intensity of the magnetic field. Overall, therefore, the AC losses of the magnet for a charge and discharge cycle amount to 5.2 kJ; this power can be extracted from the second stage of 2 cryocoolers which work at *20 K* in *120 s* and considering also the relaxation time of the coupling currents, an activation time of 1 minute is required between two consecutive cycles.

## 4.3 Evaluation of temperature distribution

The total average power dissipated in the magnet due to AC losses during a complete charge and discharge cycle at pina power is *Ptot = 502 W*. this value was determined using the THELMA numerical model. profiles of the total power density generated on the first turns of the first and fifth layer respectively as shown in Fig. 4.14.

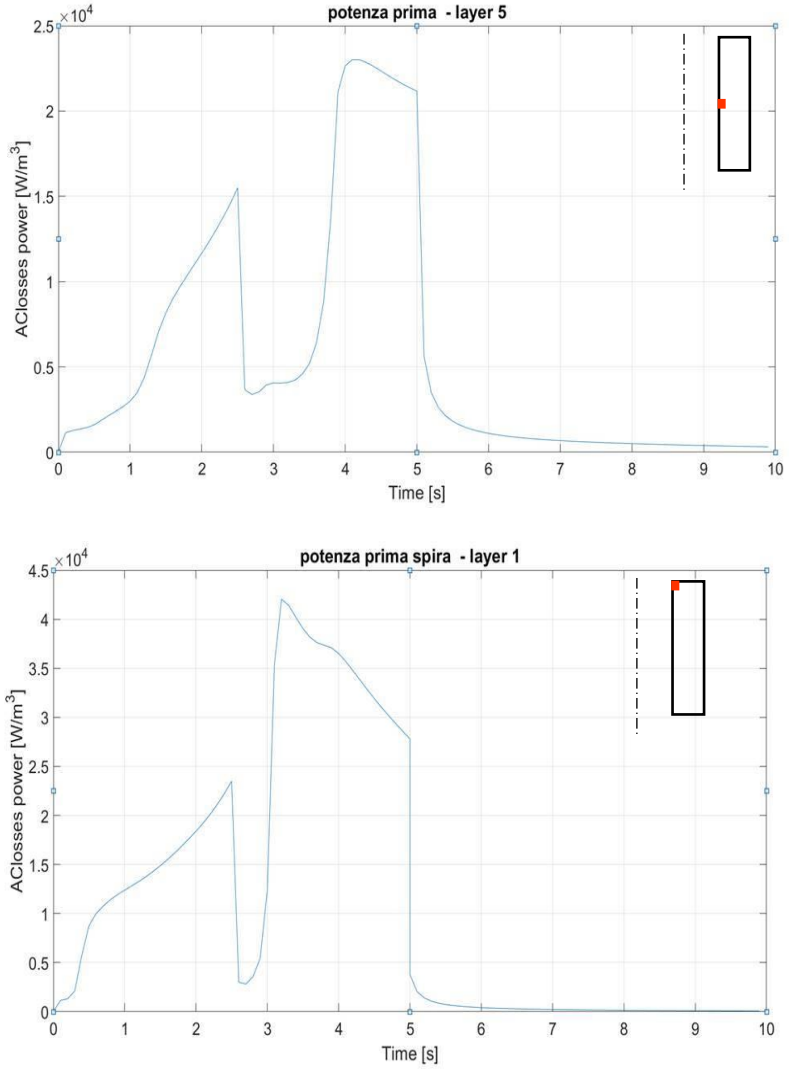


Fig. 4.14. Power density profile over time in different layers

In addition, the distributions of energy generated on the section of the magnet are reported. The map in **Errore. L'origine riferimento non è stata trovata.** was obtained as a planar interpolation of the power values on the individual turns, therefore each node of the reported map contains the value relating to the turn in the corresponding position.

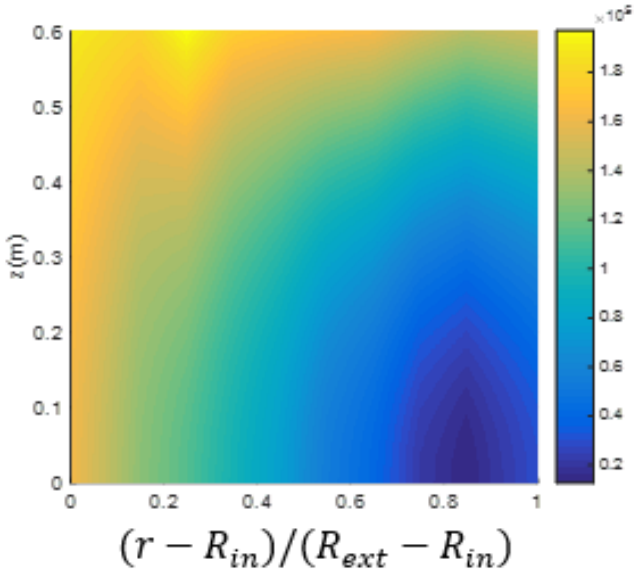


Fig. 4.15. Energy density distribution on cross section of magnet

The evaluation of the power generated by induced currents on copper was carried out with a three-dimensional thermo-electromagnetic analysis in ANSYS in which the current has a known distribution on the cycle, and in which the geometry was modeled by reporting the copper layer proposed by the partner ICAS, responsible of the thermal design, as below. The overall thermal power generated over the cycle in the copper contact is 18 W. The temperature distribution of the magnet at the end of the cycle is obtained by reporting as input in the axial-symmetrical two-dimensional analysis all the power contributions obtained from the steady-state balance and the evaluation of transient phenomena, in particular:

- the thermal power dissipated by AC losses as a function of time has been applied to each single loop;
- the thermal power dissipated by Eddy current was applied to the copper strip attached to the conductor and to the copper layer of the cold contact;
- the power radiated by the thermal shield is applied to the external surfaces;
- the power by conduction from the current leads is applied to the insertion points of the terminals in the upper part of the magnet;
- the extracted power of the cryocooler contact is applied in the midpoint outside the copper layer.

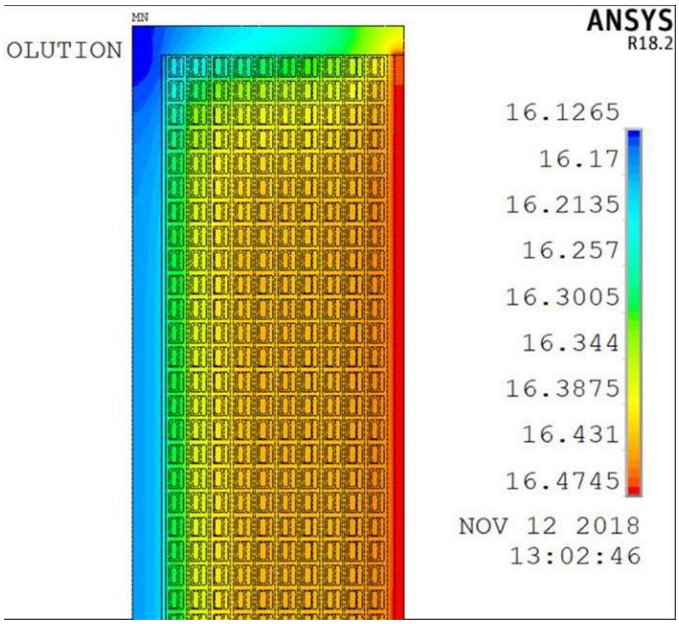


Fig. 4.16. Temperature distribution

As can be seen from Fig. 4.16, temperatures after a work cycle increase by 0.5 K.

## 4.4 Effect of magnetic field on Cryo-cooler

Furthermore, the definition of the position of the cooling system with respect to the magnet is of fundamental importance. The operating conditions of the cryocoolers are in fact limited by the magnetic field. The manufacturer therefore defines the field limits necessary to guarantee an adequate level of efficiency [2]. In particular, the magnetic field perpendicular to the displacer (component inside the cryo-cooler head) of a Sumitomo RDK-415 Cryo-cooler must not exceed 0.05T. Fig. 4.17 shows the map of the magnetic field in the presence of only the *2cm* thick steel heat shield.

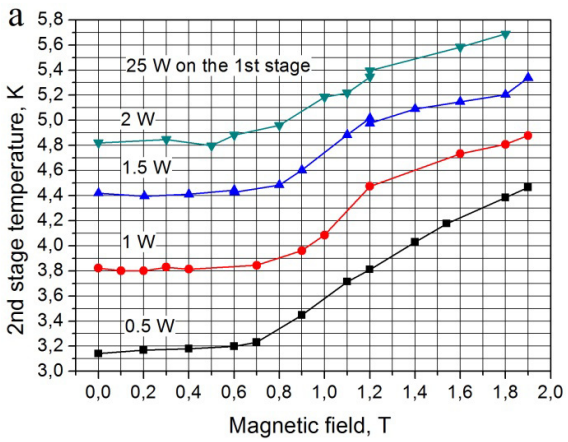


Fig. 4.17. Cryo-cooler second stage temperature depending on the magnetic field

The map is the result of an electromagnetic finite element simulation in which the magnet is in the operating conditions. It is possible to verify that by placing the cryocoolers in the upper part of the magnet, the intensity of the field is such as to allow normal operation of the cooling system.

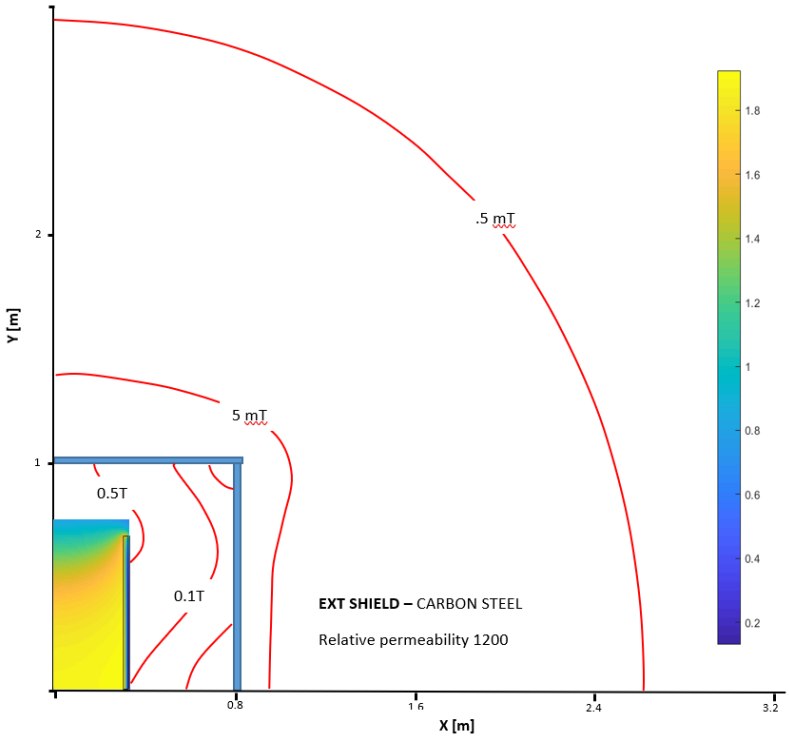


Fig. 4.18 Magnetic field with carbon steel shield

## 4.5 Quench analysis

A fundamental aspect of the superconducting magnet design is the analysis of thermal stability during normal operations and in quench conditions [41].
During a quench, if the resistive section that forms remains localized, a hot spot is created that destroys the magnet due to the out-of-control heating and the mechanical stresses that may arise from it. An HTS material with a high energy required to reach a resistive state (quench) but also with a very fast propagation, which leads to a very high final hot-spot temperature. Also, superconducting magnets are operated at cryogenic temperature. Operating magnets at such a low temperature without a proper protection measures poses a threat of magnet being permanently damaged by quenching. Simulation of quenches can help us understand probable problems and how to resolve them before they occur in real world situation. ANSYS is an example of widely used Finite Element Analysis tools to simulate this coupled multiphysics transient problem. There are two different methods to solve the coupled field problems. A *direct method,* where a coupled-field element is used that contains all necessary degrees of freedom and the corresponding stiffness matrix and the load vector takes into account all necessary terms; A *load transfer method,* which involve two or more analyses coupled by applying results from one analysis as a load to another analyses.

### 4.5.1 Quench problem

Theorical models that explain the physics behind the quench are well formulated [42] - [45]. The coupled physical boundary value problems are:

- The electrical problem, non-linear current-voltage characteristics of the superconductor; non-linear dependency of the conductor resistivity on magnetic field and temperature.
- The magnetic problem: non-linear inductance and eddy-current effects inside the coil and in other structural elements.
- The thermal problem in solids, Joule losses in conductor, temperature dependent thermal conductivity and heat capacity.

To study the dynamics of the quench, the temperature inside the magnet is calculated by solving the non-linear and three-dimensional equation of heat [47]:

$$\gamma C(T)\frac{\partial T}{\partial t} = \nabla(k(T)\nabla T) + Q_{ext} + Q \qquad (4.23)$$

Where $Q$ represents the thermal power generated in the wire during the *quench*, and $Q_{ext}$ represents the external thermal power generated by a disturbance which starts the quench event, $C$ is the temperature-dependent specific heat capacity and $k$ is the temperature-dependent thermal conductivity. The range of energy values of a disturbance due to mechanical movement or microfractures during the operation of a superconducting magnet

is attested, is from 1 to 3 J [18]. The initial heating in this case is considered as a power of 15 W applied to the external surface of the coil, on a volume of *2mm x 10mm x 0.25mm* delivered for a period of *0.1 s*. The minimum energy of quench (MQE) applied is determined by finding the minimum value of $Q_{ext}$ necessary to initiate a self-sustaining quench event.

### 4.5.2 Numerical model for quench propagation

From a numerical analysis point of view, quench simulation is one of the most challenging subject in the superconducting magnet technology [46]. The main aspects considered while solving the quench problem are:

- Transient problem, the simulation model seeks to solve the temperature profile of the coil and its derivatives as a function of time. The accurate evaluation requires the calculation of the temperature profile with smallest time steps in order of a micro-second.
- Complex geometry of the coil, the geometry construction for the numerical analysis using such materials is difficult.
- Non-linear heat flux in the boundaries, such as the heat flux and the integrated transferred energy.
- Inhomogeneous and non-linear material properties, the coil is made of superconductor, copper and the insulation material, each having material properties which exhibit a non-linear dependency on the temperature and the magnetic field. The finite element method can easily take into account in-homogeneous material properties in the calculation of the stiffness matrix. However, the non-linear problem usually involves some form of iteration or drastically reduced time steps, and the process can be computationally expensive. An efficient model would use adaptive temporal and spatial integration methods in order to reduce the computation time.

A 3D non-linear finite element heat diffusion model is introduced to calculate the evolution of the temperature profile in the conduction cooled $MgB_2$ magnet during a quench phenomenon using the element SOLID 90 for the thermal analysis in ANSYS APDL [44]. The model includes the thermal and electrical properties of the composite wire and epoxy resin, the characteristic value *n* of the superconductor which characterizes its behavior during transition and the critical current profile of the superconductor and the inductance of the magnet. It is therefore assumed that the quench event occurs while the magnet operates at the temperature conditions of *Tn = 17 K* and with the maximum current of *Imax = 467A* and the current profile during the quench is reported in Fig. 3.6.

The disturbance occurs on the external surface of the magnet where the magnetic field is less intense, in order to consider the worst condition. Furthermore, to reduce the computation time, it is useful to consider the volume surrounding the spot where the disturbance occurs as the only computation domain.

Fixed temperature conditions on the upper, lower and radially innermost surfaces of the domain (Dirichlet condition) are imposed to simulate the thermal conduction inside the magnet in order to take into account the parts not included in the domain.

On the external surface, however, a condition of thermal insulation is applied (Neumann condition). Thermal radiation is not considered. It is also necessary to consider a delay time that takes into account the time that the detection system takes to detect the quench by operating the switch that starts the discharge. This delay is *Td = 0.3 s* .
Hence, the temperature rises and the resistive voltage across the coil is calculated for all time steps of the simulation. The quench may propagate further or vanish depending upon the intensity of the heat pulse and the Joule heating corresponding to the transport current. On the one hand the heat conduction phenomenon in the wire decreases the hot-spot temperature, on the other hand the Joule effect increases the temperature of a node that is in the normal conducting state. Since usually at the onset of a quench only a small fraction of strand is above the critical temperature, in the beginning of the transient, the heat conduction phenomenon becomes more effective compared to Joule heating and the hot-spot temperature drops. If the intensity of heat pulse is below a certain limit, the initial drop in hot-spot temperature can fall below the critical temperature thereby preventing quench propagation.
At every time step the critical current of the superconductor is recalculated on every element of the domain depending on the magnetic field that is decreasing due to the discharge of the current and on the temperature that is rising due to the propagation of the heat flux coming from the disturbance. $Q_{int}$ represents the internal heat generation, which comes from internal heating in the wire and is given by:

$$Q_{int} = \frac{I}{A} min\left\{E_c\left(\frac{I}{I_c(B,T)}\right)^n, \rho(B,T)\frac{I}{A}\right\} \quad (4.24)$$

Where *I* is the current, A is the cross sectional area of the wire, *Ec* is the electric field criterion, *Ic (B,T)* is the critical current fir the superconductor, *n* is the n value of the wire, and $\rho$ is the average resisitivity. If the value of the operative current is higher than the critical current one, the transition of the superconductor occurs and the current flows into the copper strip with a heat generation by means of joule effect.

### 4.5.3 Numerical results - hot spot temperature during quench

These results show the temperature of the coil during a quench event. In Fig. 4.19 the maximum winding temperature is shown as a function of time. It is shown how the temperature rises very quickly during the disturbance event and therefore the effect of the heat capacity and the reduction of the current allow to reduce the temperature to a non-critical value.

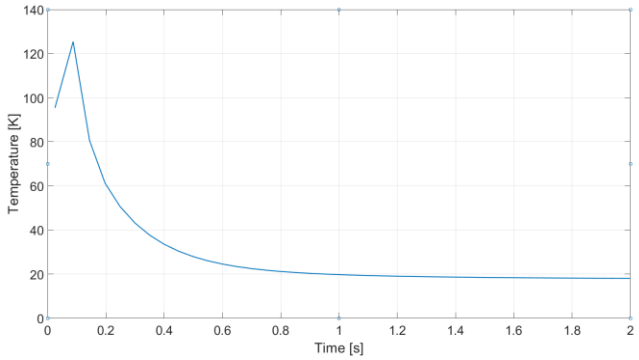


Fig. 4.19. Max Temperature during the quench

In our case one can notice from the figure that initially the hot-spot temperature drops however does not fall below the critical temperature thus leading to quench zone expansion and further heat generation. The generated heat propagates longitudinally successively raising the temperature above critical temperature and propagating the quench. The effect of thermal conductivity is also important: in Fig. 4.20 it is shown how the volume in which the superconductor turns into the normal state has a small size and how the temperature has already risen to *19.84 K* after 1 s.

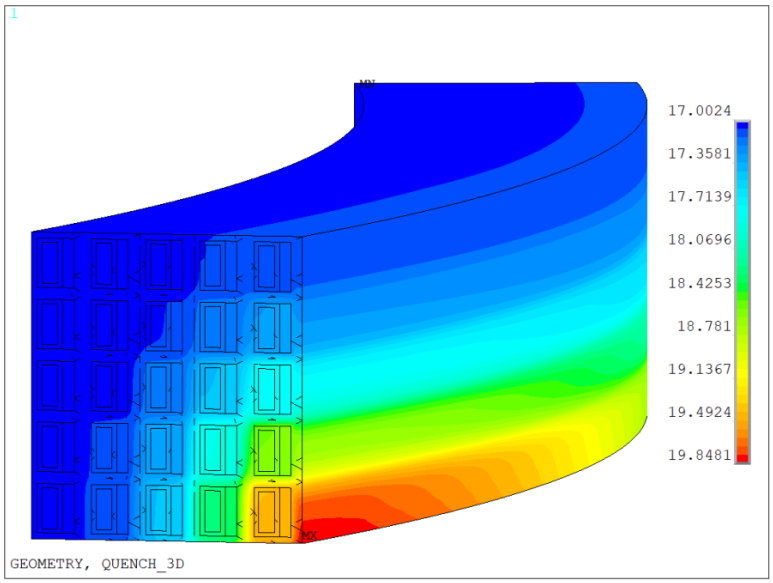


Fig. 4.20. 3-D temperature distribution at t=1s after the quench event

Once the temperature in the coils has been calculated, an ANSYS post-processing simulation verifies that the stress and strain of the $MgB_2$ superconductor and epoxy insulation are within the 0.2% strain safety limit. The element SOLID185 is used for the thermo-mechanical analysis. In addition to the development of deformation, the shear stress in the epoxy must also be considered. The maximum stress value due to the

temperature increase is 20 MPa as shown in. This stress value, to be considered in addition to the previously calculated stress, is negligible in a first approximation.

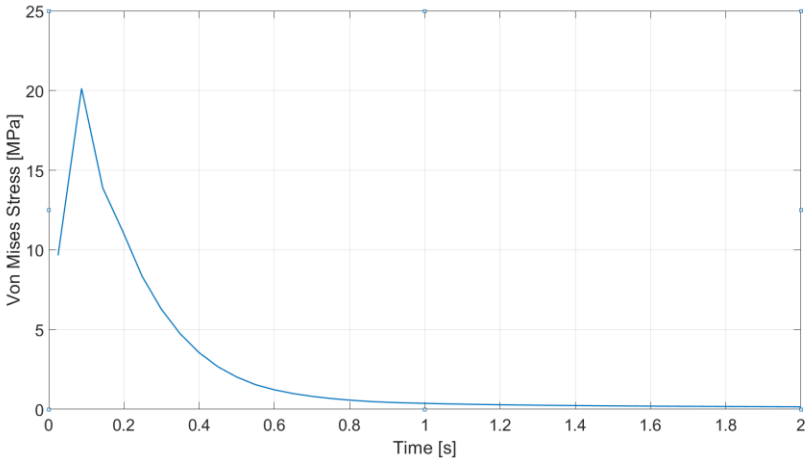


Fig. 4.21. Max Von Mises stress profile

From Fig. 4.22 the strain value in $MgB_2$ is well below the safety limit of 0.2%, even if superimposed on the strain value of the winding process, cooling and electromagnetic charge. Also for what concerns the strain, the value obtained following the quench event in the epoxy resin of 0.006% can be neglected. As far as protection is concerned, the magnet can therefore be considered safe in terms of stress and strain on the conductor and on the resin.

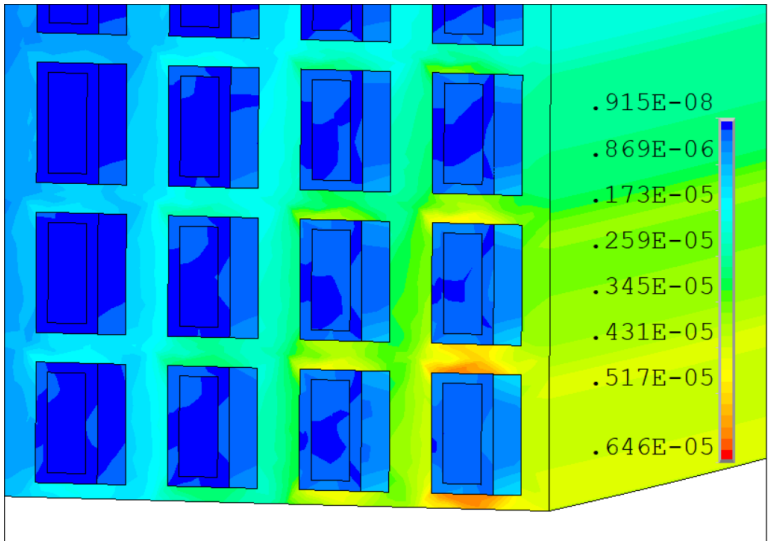


Fig. 4.22 3-D strain distribution at t=0,5s

## 4.6 Conclusions

The design of a solenoidal coil has been carried out by means of the methodology previously exposed. These tools have been developed and, thus, implemented in a software environment specially developed with the support of commercial software, for the Multiphysics design of the system.

In order to accomplish the project specifics in terms of power and deliverable energy, a 6 filaments rectangular tape supplied by the manufacturing company has been selected for the design. The stability of the superconductor is guaranteed by the application of a copper strip with an adequate thickness. The mechanical verification method has been defined for the assessment of the strain level on the winding during the phases of its operation: winding process, cool-down and energization. The strain value caused by the mechanical stress applied to the coil in the operating phases falls within the allowable values. Therefore, mechanical stress levels allow a stable operation of the superconductor

The evaluation of he AC losses has been implemented with THELMA code and the calculation of the thermal load on the SMES system has been carried out using an equivalent thermal circuit model. A 3D finite element model of non-linear heat diffusion has been also developed for the evolution of the temperature profile in the $MgB_2$ conduction cooled magnet during a quench phenomenon

A voltage transient occurs in the SMES due to the commutation of the chopper. This voltage at the terminals is not evenly distributed on the turns of the coil, but rather is concentrated on the turns located on the input terminal, thus creating a hot spot of the electric field. An accurate determination of the impulse voltage distribution in the winding is obtained using an equivalent lumped parameter network model developed in MATLAB. The distribution of the excitation voltage that comes out of the previous calculation is implemented with a finite element analysis for the electrical dimensioning of the insulation. The executive drawings of the designed magnet are shown in the Appendix1

# 5 Design of HTS coil of SI-SFCL in a 30 kV/1 kA DC power grid

## 5.1 Introduction

Nowadays a high-power quality is necessary to integrate increasing amount of distributed generation sites into the grid. In this case a more sophisticated electric network with high short circuit rate is needed, with low vulnerability in case of fault[22][48].

Driven by the advances in voltage source converter (VSC) technology and rapid growth of end-user DC loads, MVDC grids are now receiving an increasing attention as an enabling platform for grid integration of wind and photovoltaic sources and energy storage, and for the supply of DC loads. In a VSC-MVDC system, the DC circuit breaker (DCCB) uses a quick isolation switch to interrupt the current and isolate the fault on the DC side, then resume power supply to the system to return to normal operation. However, because there is no zero-crossing point like AC system current, interrupting DC fault current is very difficult and DCCB for MVDC power systems has not been commercialized yet.

A fault current limiter (FCL) is a device with nonlinear behavior in which the inductance can change as soon as the current achieves a certain value [49]. Such a tool is able to increase the short circuit power of network in nominal condition without hazard for the grid in case of fault. Lately there is a widely spread interest for current limiter in medium voltage network [50]. In medium-voltage direct-current transmission system based on voltage source converter (VSC-MVDC) a high peak value and fast rising speed of the DC side current can occur in case of fault. This fault current can easily damage components of inverter and protection devices. Current limiting technology is required to suppress the DC fault current and slow down the capacitor discharge.

Among the various topologies, saturated core superconducting fault current limiter (SFCL) has been introduced, which is an effective means of significantly reducing the stress on the DCCB in MVDC systems due to the inherent physical characteristics that can quickly limit the fault [51]. Unlike the resistive type SFCL, the saturated iron-core type SFCL (SI-SFCL) reduces the magnitude of the fault current using the non-linear behavior of the iron-core. This limiting technology is particularly suited for high voltage and high capacity DC power. In this thesis, the design of a SI-SFCL for a MVDC power system is presented, with focus on the core configuration and coils. More specifically, the electrical characteristics and operating principle of the SI-SFCL for the DC power system are first analyzed . Next, the detailed design process is introduced and optimal configuration of the SI-SFCL is proposed. Numerical models are used to determine the parameters and the layout of the SI-SFCL needed to limit the magnitude of the fault current by 70%. The SI-SFCL consists

of a primary copper coil (PC) connected to the DC power system, and wound onto a iron-core. The iron core is driven into saturation by means of a superconducting secondary coil (SC) supplied by a DC current. The design of each of these elements (primary and secondary coil and core) strongly impact the operating conditions and the limiting effect of the device. A 3D finite element model is developed to investigate the dynamic behavior of the system with different core configuration and the importance of the losses performance of SFCL [52]. For this purpose, different open-core and close-core shapes are compared in term of efficiency, current limitation, depth of saturation, weight, and cost. Also, coil position wrapped on the core and shape of bobbin where the primary coils are wound onto are analyzed in terms of effect on core magnetization. The configuration that minimizes costs and weight is defined, and material and level of lamination of the core is chosen, in order to decrease the induced current in the core during the fault. Number and disposition of coil on primary and secondary side are also studied as well as the influence on the magnetic response of shape and material of coil bobbin. Based on these results the next step is the design of the superconductive coil and its cryogenic cooling system finalized to the realization of the prototype. The key advantage of the saturated core SFL is the DC operation of the superconductor. AC loss does not occur and only a small cooling power is needed. There are many companies involved in the development of this technology for application at the medium voltage level[53]-[54]. However, the size of the device can be a concern and most of the studied design still suffer of some drawbacks of the original design. In this design indication are adopted which resolve the described issues.

## 5.2 Case study and simulation circuit

The SI-SFCL consists of a copper coil and a superconducting coil wounded onto a common iron core as is shown in Fig. 5.1, the superconducting coil is connected to a DC current source [16]. The copper coil is connected to the protected circuit. The DC SI-SFCL is aimed at the protection of the 30 kV-1kA MVDC system shown in Fig. 5.1. The main characteristics of the system are resumed in Table 5.1. More specifically, the aim of the SI-SFCL is to reduce by 70% the prospective fault current of 44 kA. The limiter is installed in the AC/DC converters station. In order to protect the circuit also in case of pole to ground fault, two identical DC SI-SFCL need to installed on the positive and the negative poles of the converter station, as it is shown in in Fig. 5.1 The peak value of the fault current depends on the fault location and type. A pole-to-pole fault occurring at 1 km from the terminal station is considered in order to evaluate the effect of the SFCL on the system. This is amongst the most severe fault conditions that can be realistically considered, generating the highest peak of the fault current.

Table 5.1
MAIN PARAMETERS OF THE POWER CONDITIONING SYSTEM

| | |
|---|---|
| Rated voltage, $V_n$ | *± 15 kV* |
| Rated current, $I_n$ | *1 kA* |
| Rated power, $P_n$ | *30 MVA* |
| DC link capacitance, C | *0.866 mF* |
| DC cable resistance per unit legth, *r* | *0.0183 Ω/km* |
| DC cable inductance per unit legth, *l* | *0.178 mH/km* |
| Fault current without FCL | *44 kA* |
| Target limited fault current | *13.2 kA* |
| Target limiting factor | *70%* |

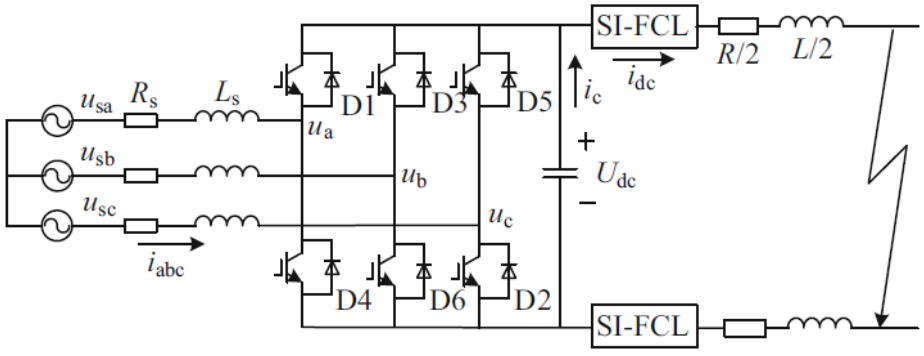


Fig. 5.1. MVDC system with SI-SFCL

When a fault occurs on DC side, the IGBTs are blocked for self protection. Hence, since the free wheel diodes are interdicted by the DC link capacitor, the AC grid is disconnected form the system. During this phase the capacitor discharges into the short-circuit point, creating the overcurrent [73]. Based in this picture the equivalent circuit shown in Fig. 5.1 is considered for calculating the fault current. In this circuit two identical SI-SFCL are involved. Each of them is modelled with a pair of coupled inductors, with one inductor connected to the protected circuit and the other connected to a DC current source. Before time $t_f$, when the fault occurs, switch S1 is ON and switch S2 is off, corresponding to the nominal current of 1 kA circulating in the circuit and providing the nominal power of 30 MVA to the load. At the instant $t_f$ of the fault both the switches change state, commanding the disconnection of the AC grid and bypassing the load's resistor, thus producing the discharge of the capacitor and te related overcurrent. It is worth to report that a similar circuit, with voltage $V_n/2$ of the generator and one SI-SFCL, also holds for modelling a pole to ground fault

The results are obtained by a 3D finite elements model in which the electro-magnetic analysis of the SI-SFCL is coupled with the circuit analysis of the DC grid as in Fig. 5.2. the DC grid is simulated by means of a voltage generator, which supplies the current to the primary coil in the normal state and a capacitor charged in parallel. The capacitor is pre-charged with a DC voltage up to 30 kV by means of DC generator driven by switch S2. At the current fault time *t =1.5 s*, the switch S1 is closed and the capacitor discharges on the primary coils.

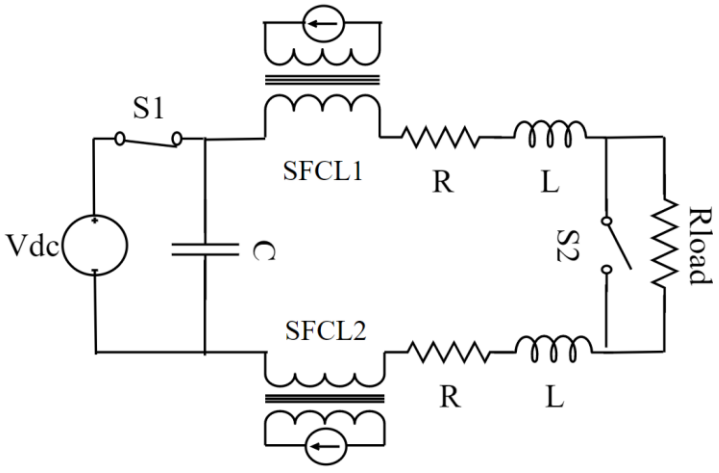


Fig. 5.2. Circuital scheme of DC network

## 5.3 Main characteristics of the SI-SFCL and finite element model

The SI-SFCL consists of a copper coil and a superconducting coil wounded onto a common iron core [16], as shown in Fig. 5.3.a. The superconducting coil is supplied by a DC current source. The copper coil is connected to the protected circuit. The two coils are wounded onto the core with opposite directions, so that the magnetomotive forces that they produce subtract.

During normal operating conditions, the core operates in the saturated region due to the bias magnetomotive force $N_{sc}I_{sc}$ produced by the secondary superconducting coil, as it is shown schematically in in Fig. 5.3.b. In fact, the two windings are designed so that the total magnetomotive force $N_{sc}I_{sc} - N_P I_n$ in normal condition is larger than the value $NI_{SAT}$ needed for producing the saturation of the core. Since in this condition the differential permeability of the iron-core is small, the equivalent inductance is low and the device has a negligible effect on the network behavior. When a fault occurs in the protected DC circuit a high current flows in the primary coil. The core is driven out of saturated state in the linear area, which rapidly rises the differential permeability and inductance, limiting the fault current.

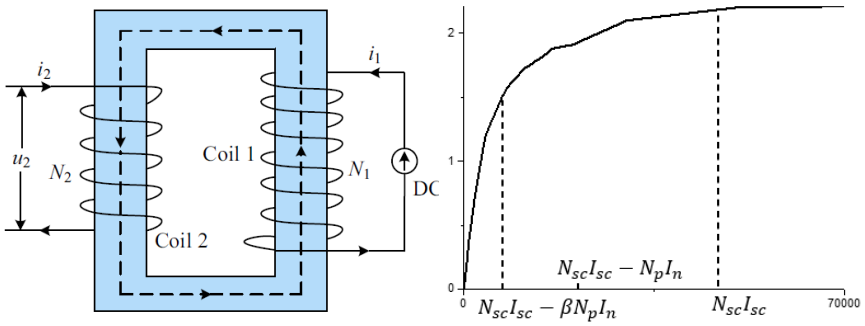


Fig. 5.3 structure of SI_SFCL for MVDC system. b) Schematic Φ-NI curve of the iron core

The main characteristics of the SI-SFCL are reported in Table 5.2. First we report that, as it is discussed in detail in [80], the operating current $I_{SC}$ of the superconducting coil is fixed to a value allowing the optimal design of the SC coil. This value depends on the HTS conductor, the current leads and the operating temperature chosen for the coil. In the present case a value of $I_{SC}$ = 420A is assumed, as motivated in [80]. The procedure developed in [72] is applied for obtaining the other parameters of design. A preliminary number of turn *Np*= 150 is obtained for the primary coil. This corresponds to a 100 V per turn, which is a typical value used for the design of the AC transformers windings [49]-[58]. The final number of turns is arrived at in the next section by evaluating compliance of the limiting performance of the SI-SFCL with the target limiting factor of 70%.

Table 5.2
MAIN PARAMETERS OF THE POWER CONDITIONING SYSTEM

| | |
|---|---|
| Operating current of the SC coil, $I_{SC}$ | *420 A* |
| Cross section of the core, *S* | *0.465 $m^2$* *(1.2e-4*sqrt(15e6))* |
| Number of turns of the copper winding, $N_P$ | *150* |
| Number of turns of the winding, $N_{SC}$ | *430* *(150*1200/420)* |

Based on the operating principle of the SI-SFCL described above the number of turns $N_{SC}$ of the superconducting coil is obtained from :

$$N_{SC}I_{SC} = (NI)_{SC} + \alpha N_P I_n \qquad (5.1)$$

where α is the allowable overload margin of the DC current. By assuming $\alpha$=1.2 and by neglecting the magnetomotive force needed to reach saturation, that is the first term of the RHS of equation (5.1) (which is much smaller compared to the magnetomotive force $N_P I_n$ impressed by the primary coil), a value of $N_{SC}$ = 430 is obtained.
The fault current of the MVDC system is calculated by coupling a 3D magnetostatic finite elements model of the limiter with the equivalent circuit of the system shown in Fig. 5.2. Circuital scheme of DC network In this circuit the SI-SFCL is schematized by means of two coupled inductors. The FEM modelling is in needed because the self and mutual induction coefficients of the coupled inductors depend on the magnetic state of the core, which in turn depend on the circulating current of the circuit. This means that the magnetic state of core has to be recalculated for every time step via a magnetostatic FEM analysis [55].

## 5.4 Comparison of different core geometries

The disadvantages of the saturated iron-core type SFCL are the large dimension and mass of the core and the large voltage induced on the DC coil during the limitation. The layout of the iron core has a significant impact on both these factors. Hence, appropriate design of the core is crucial for optimizing the performance of the SI-SFCL device. In this section, two different layouts, the shell type and the core type shown in Fig. 5.4. Core shape of SFCL a) shell type b) core type, are considered for the design of the core and compared in terms of fault current limiting capability and induced voltage on secondary coil. In the shell type layout, the windings are concentric and are placed on to the central leg, with the SC winding at the outer side. In the core type layout, the SC coil is placed on to the bottom yoke (or equivalently on the bottom yoke) while the primary core is split in two halves placed on the core's limbs. The shell type configuration allows a strong coupling of the two windings, regardless of the state of the core. This imply that any transient of current in the copper coil induce a significant voltage on the superconducting coil. In the core type configuration, the interaction mainly occurs via the leakage flux of the copper coil, thus inducing a reduce voltage on the SC winding in transient conditions.

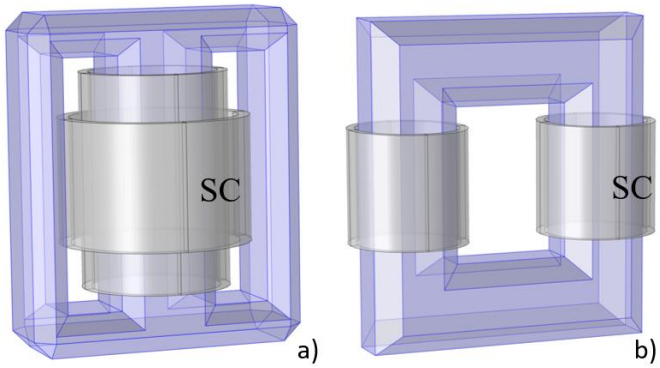


Fig. 5.4. Core shape of SFCL a) shell type b) core type

The core type layout is more economical and easier to manufacture than the shell type design. Furthermore, it avoids the strict proximity between the primary and the secondary coil thus allowing a more relaxed design of the SC coil and the cooling system. A laboratory scale prototype of SI-SFCL with 500V/50A rating is now under development at CNU

The fault current of the MVDC circuit with the shell type SI-SFCL with different number of turns of the copper coil is shown in Fig. 5.5. The fault current obtained with the core type SI-SFCL with different number of turns of the copper coil is shown in Fig. 5.6. It can be seen that for different number of turns in primary coil (*Np=150,200,250*) a different limiting capability is obtained. The number of turns previously chosen of 150 allows to achieve the target of current limitation only in the shell type of the core. Others number of

turns have been considered in order to compare the two different configurations of core with which both of the cases respect the requirements.

In both types the limitation target is achieved already with the number of turns of 200 on the primary

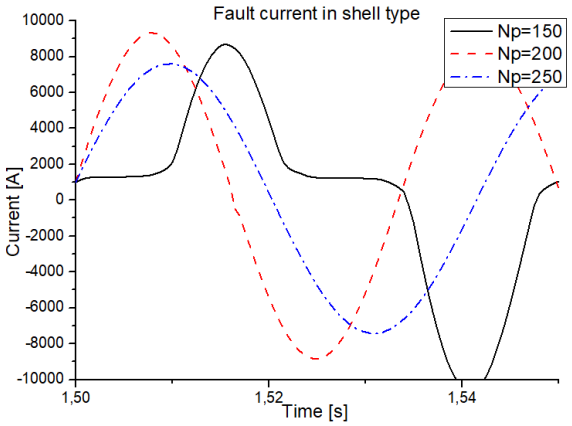


Fig. 5.5 The fault current of the MVDC circuit for the shell layout of the SI-SFCL with different number of turns of the copper coil

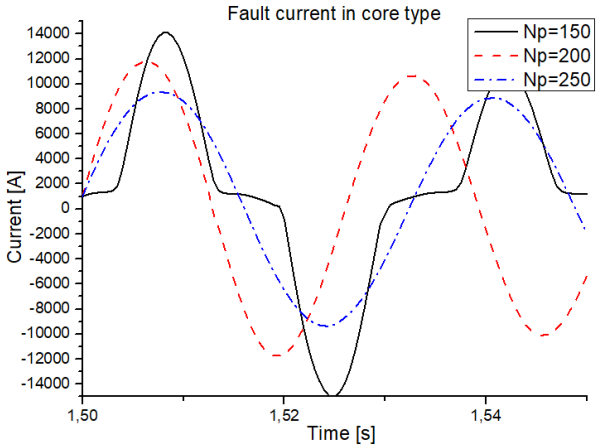


Fig. 5.6 The fault current of the MVDC circuit for the core layout of the SI-SFCL with different number of turns of the copper coil

An important effect emerges in Fig. 5.7 where the induce voltage profile are shown with a current of 420 A (Isc). The shell type configuration presents higher value of induced voltage($e.m.f = 39\ kV$). The primary and secondary coil are wounded on the same limb and their reciprocal position causes a strong magnetic coupling acting as a transformer.

Table 5.3

COMPARISON OF DIFFERENT CORE GEOMETRIES

| Core type | **Shell type** | **window-type** |
|---|---|---|
| Coil turns (Np) | *200* | *200* |
| Yoke-cross section [$m^2$] | *0,64* | *0,64* |
| Yoke length [m] | *6,8* | *8,6* |
| SC coil current [A] | *420* | *420* |
| SC coil turn (Ns) | *700* | *700* |
| Core volume [$m^3$] | *2.24* | *1.953* |
| Electro-motive Force [kV] | *39* | ***17*** |
| Material Cost [k$] | *186+21* | *186+18* |

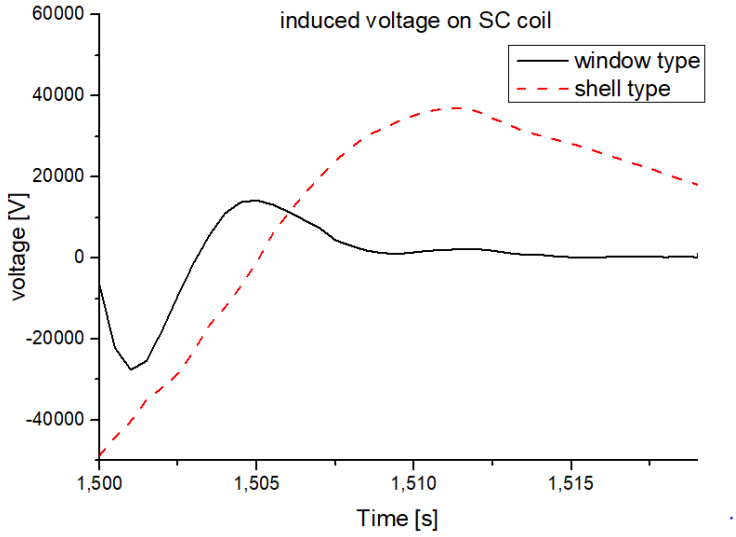


Fig. 5.7. Induced voltage on SC coil

This effect is drastically reduced in the window type configuration where the primary and secondary coils, wounded on two different limb, have a lower magnetic coupling . In Table 5.3 are reported the final specifics for all the analyzed configuration, the final cost is been calculated taking into account the cost of the total length of superconductor required for the secondary coil (2G HTS SUNAM is been considered) and the cost of the volume of core material required for the core. The window type can be considered as optimal configuration for this application.

## 5.5 Winding direction

In AC application of SFCL a pair of coils for each phase with each of the coils wounded in opposite direction is used; this coils arrangement is needed to limit the fault current regardless of its direction (positive or negative) .

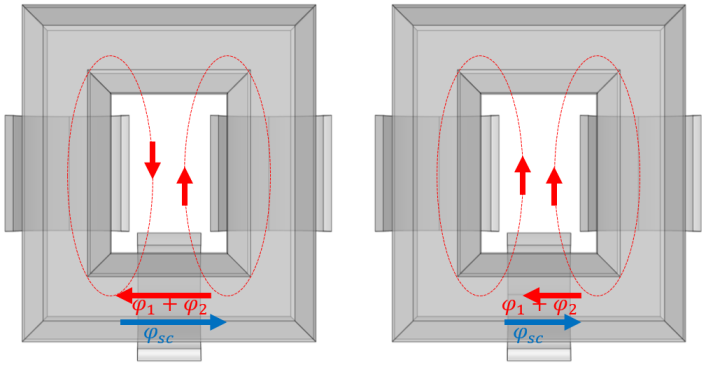


Fig. 5.8. schematic representation of coils fluxes a) normal primary winding direction b) inverted primary winding direction

In the DC application, dividing the primary coil in two sub-coils wounded in opposite direction and connected in series can be considered to obtain two important effects:

- reduce the voltage induced on the SC coil during the fault.
- reduce the number of turns needed for the SC coil.

In order to point out these effects, the window type configuration is considered as an example and the two following cases are compared:

- *Case 1* - normal winding, one copper coil and one SC coil wounded on the limbs of the core.
- *Case 2* - split inverted winding the copper coil is splitted in two parts wounded with opposite directions on to the core limbs.

The SC coil is wounded in the lower yoke of the core. This configuration is shown in Fig. 5.4. For both cases, the same number of turns is assumed, in total, for the copper (Np=200) and the superconducting coil (Ns=430). The operating conditions of the core are shown in Fig. 5.8 for the two cases considered:

a) In normal case the direction of primary is opposite to the secondary flux and more Ampere-turns are needed on the secondary side to drive the core throughout the linear region to make it saturated.
b) By splitting the primary side in two coils with opposite direction a neglectable magnetic flux is produced on the core, so that less ampere-turns are needed on secondary side to saturate the core.

c) When the fault occurs only one of the coils participate to desaturation of the core whereas the core part under the other coil remains saturated; .

In the core section underneath the primary coil, different values of magnetic flux density are reached in operating condition; In this configuration only one of the primary coil contribute to the fault current limitation: whereas one coil drives the core in the non-saturated state, the other with the flux in the same direction of the SC coil, holds the core saturated. In Fig. 5.9 is shown the average value of the magnetic flux density on the section of the core underneath the two coils on primary side over time: before the fault both of coils are saturated with a magnetic flux density higher than 1.65 T and during the fault only one is driven in non-saturated state. Theoretically, the sum of primary coils flux in the inverted winding configuration would be always zero on core with consequently no current fault limitation; instead, the leakage flux affects the magnetization level on core and the limbs behave as two separated core with different magnetization.

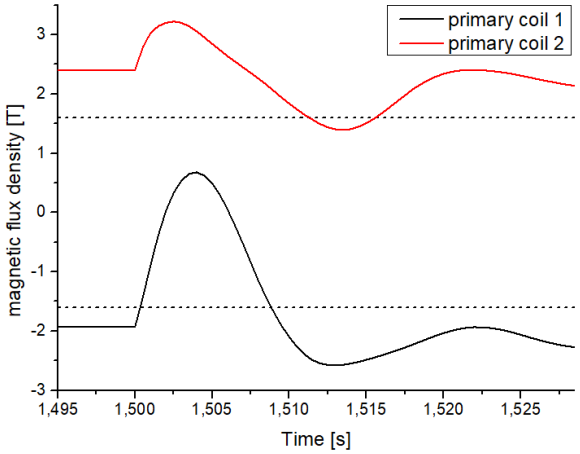


Fig. 5.9. Magnetic flux density in primary coil

Another crucial point in the saturated core fault current limiter is the DC operation on the superconducting coil; the DC operative condition offers the benefit of a small cooling power for the absence of AC loss. Nonetheless, the protection of the secondary SC coil is not trivial because the superconducting winding is strongly coupled with the protected circuit during the fault and a high induced current may appear over the critical value of the superconductor.

For MVDC grid, the high value of fault current and the very short time of fault can cause induced voltage which can damage the DC bias source and affect the current limiting performance.

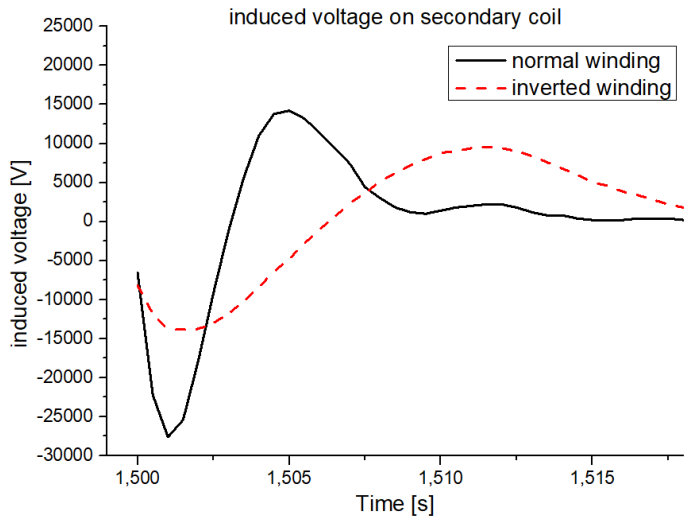


Fig. 5.10. Comparison of induced voltage on the secondary coil

In Fig. 5.10 are shown the induced voltage profile on the secondary SC coil for two of the configurations considered in the core type which represented the most emblematic cases. The induced voltage is evaluated as the time derivative of the flux linked; the core type presents an induced voltage lower in the inverted winding configuration (*e.m.f. = 10 kV*) than the normal winding configuration. The reason is that the SC coil on the short limbs of the core are collocated on the plane of symmetry in between the two copper coils so that they are exposed to minimum flux and the transformer-coupling problem is minimized.

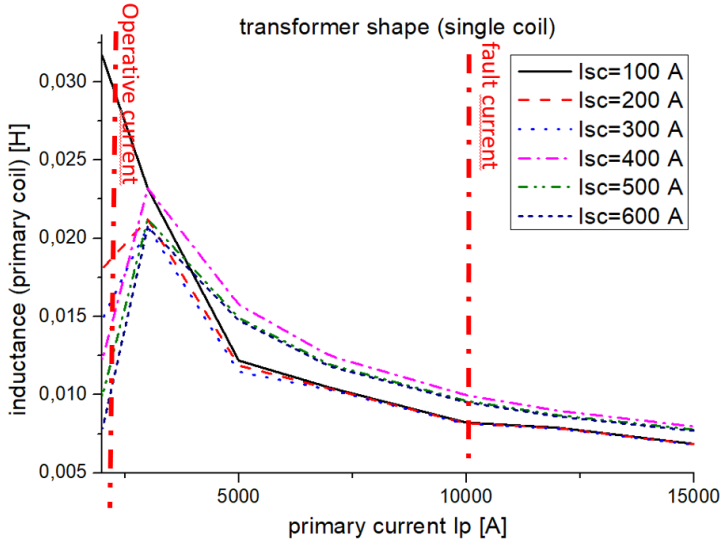

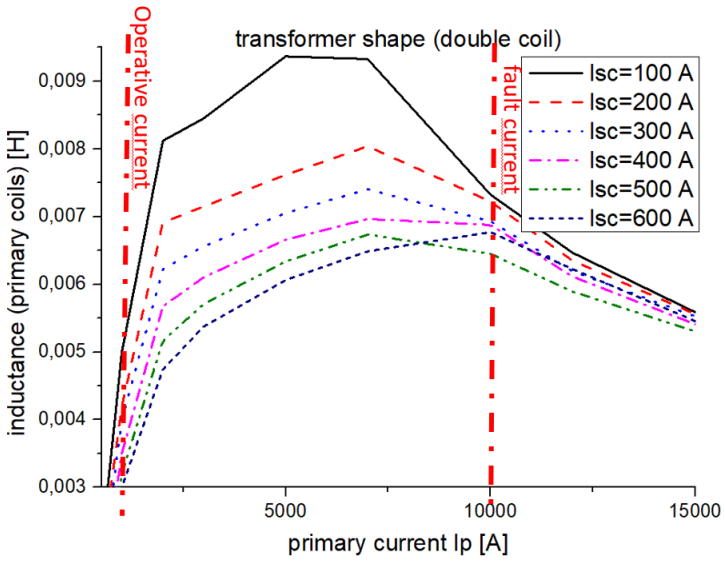


Fig. 5.11. inductance of primary side with different level of current on secondary side a) normal winding b) inverted winding

The main effect of this configuration is on the inductance of the primary coil from the point of view of the DC power network; In Fig. 5.11 the inductance over the current is shown for both normal winding configuration and inverted winding configuration at different level of current on the secondary side. In the normal configuration the increase of inductance (for a current on secondary coil of 400A the inductance rises from 0,01 mH to 0,022 mH) is high enough to limit the current. In the inverted configuration the rise of inductance is also present at the current fault , even if in this case, the increase is lower (from 0,003 mH to 0,0065 mH) and the current margin is small (for a small over-current gains an higher inductance).

## 5.6 Material Selection

The SFCL can convert the electric energy of the capacitor into magnetic energy; this process in real condition depends on the losses is the system. During the transient a magnetic material has a cyclic magnetization and two type of losses, eddy and hysteresis losses, occur in it. The losses can cause a delay in magnetization of core dissipating the magnetic energy, and can be minimized using a better grade of core material and thinner lamination, respectively as shown below for losses power:

$$P_{eddy} = \frac{V}{12\rho} d^2 \left(\frac{dB}{dt}\right)^2 \quad (1)$$

$$P_{hyst} = K_2 f B_{rms}^{n} \quad (2)$$

Where and $K_2$ are material dependent constants, d is the thickness of core lamination, B is the effective flux density value and n is the Steinmetz constant[33].

Table 5.4.
CHARACTERISTIC CORE MATERIAL

| **Core material** | **Hard iron (S45C)** | **Silicon steel (M-36)** | **Silicon steel (M-6)** |
|---|---|---|---|
| Permeability | *150* | *3000* | *7000* |
| density [kg/m3] | *8190* | *7700* | *7800* |
| Resistivity [Ω*m] | *1.67e-7* | *4.7e-7* | *5e-7* |
| Steinmetz constant | *10.5* | *1.91* | *1.91* |
| Coercivity [A/m] | *800* | *60* | *7* |
| Core losses | *Very high* | *Low* | *Low* |
| Saturation field[T] | *1.6* | *1.7* | *1.7* |
| Cost [$/kg] | *20* | *50* | *100* |

Different types of material have been considered, in which the saturation flux density remain practically constant, but the magnetic characteristic and conductivity change offering different solutions as shown in Table 5.4.

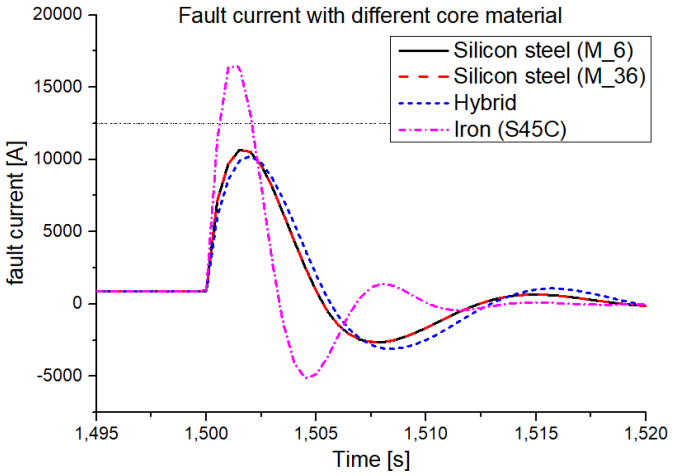


Fig. 5.12. Comparison of fault current with different material

A comparison between the effect of different core material on the fault current limitation is shown in Fig. 5.12. Iron as core material does not allow the SFCL to reach the fault current limitation target (12,5 kA). The two different types of Silicon steels present the same performance but the oriented-grain type (M-6) is more expensive because it is a very high loss characteristic. These kinds of material are produced with different lamination thicknesses according to the magnetic variation rate (0,3 mm for frequency up to 200 Hz).

In order to reduce cost and keep the same efficiency, an hybrid solution is been considered: the main material of the core is Iron except for the core section underneath the primary coil which contribute to the fault current limitation; as above explained, the core losses delays its de-magnetization, negatively affecting the response to the fault. Thus, it is possible to use silicon steel, with high cost but low losses, only for the core section meant to be de-saturated. This solution offers good performance and a reduction of the total cost.

## 5.7 Design of superconductive magnet of SFCL

The geometry selected for the core is the window type, where the magnetic core is shaped as window. The copper coil is split in two parts mounted on the limbs. The SC coil is mounted onto the yoke [60].

In the SC design, the circular solenoidal shaped double pancake coils (DPC) is applied, with 6 DPCs. The number of turns in each DPC is 116. The dimensions and parameter of the system are reported in Table 5.5.

Table 5.5
SC COIL SPECIFICATIONS

| **Item** | **Value** |
|---|---|
| Current on secondary side | *420 A* |
| Number of DPC | *6* |
| Number of turns for DPC | *118* |
| Total number of turns | *708* |
| Inner radius of magnet | *400 mm* |
| Total height of magnet | *240 mm* |
| Thickness of Al support | *5 mm* |
| Inner radius of thermal shield | *390 mm* |
| Height of thermal shield | *355 mm* |
| Inner radius of cryostat | *350 mm* |
| Height of cryostat | *605 mm* |
| Thickness of cryostat | *5 mm* |

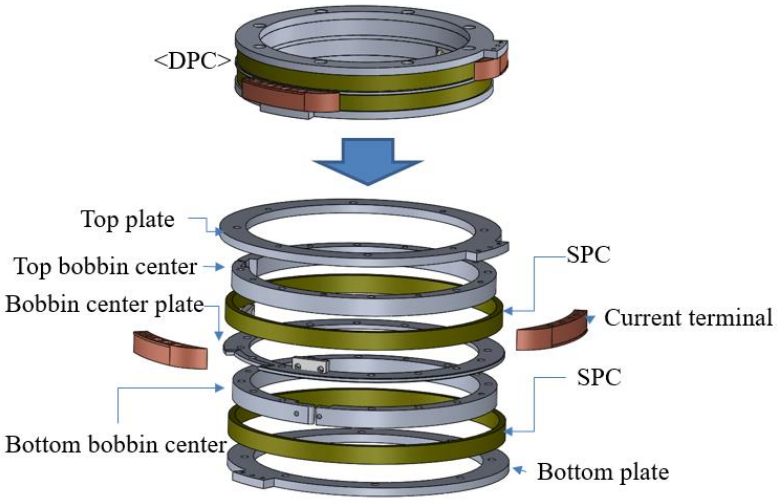


Fig. 5.13. Exploded view of DPC

As shown in Fig. 5.13 a DPC is made of the superconducting coil supported by a bobbin with two plates at the top and at the bottom; A skeleton of Aluminum withstands induced voltage as pancake-to-pancake insulation with no effect on the current fault limiting capability. in Fig. 5.14 a comparison between the fault current with and without aluminum support is shown, where the value of the current is 4200 A for both the cases.

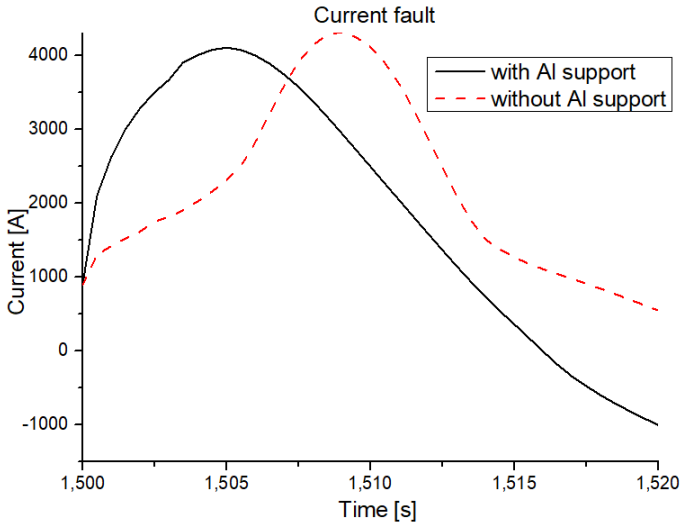


Fig. 5.14. Comparison of fault current

During the current fault the induced current in the Aluminum bobbin shield the SC coil furtherly decrease the induced voltage. The energy released for eddy current losses (P = $1{,}7\text{x}10^{-7}$J) does not cause temperature raising which can influence the cooling system; the value of induced voltage on SC coil is decreased from 11 kV to 1500 V as shown in Fig. 5.15.

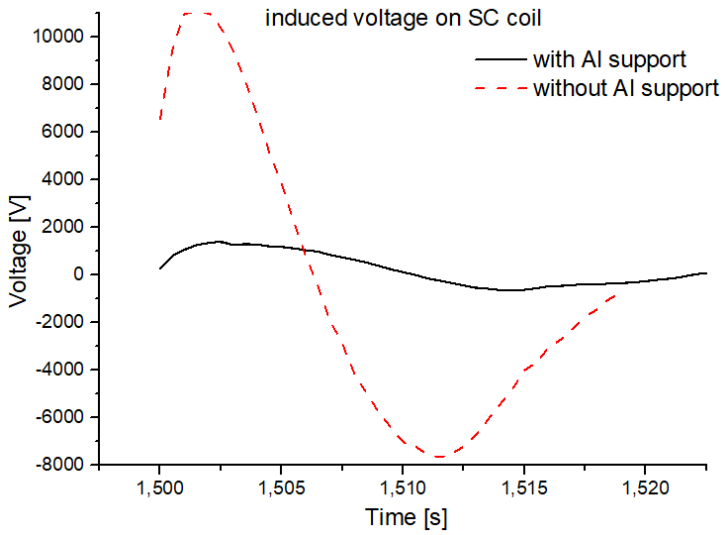


Fig. 5.15. Comparison of induced voltage on SC coil during the fault

## 5.8 superconductor for SI-SFCL

Different second generation high temperature superconductor tapes (YBCO coated conductors) are considered for the design of the coil. In Table 5.6 the dimensions of the tapes, the cost and the critical current at 77 K with no external field [61] are reported.

Table 5.6.
SUPERCONDUCTING TAPES CHARACTERISTICS

| SC tape | **SuNAM** | **BASF** | **Theva** |
|---|---|---|---|
| Width | *12 mm* | *10 mm* | *12 mm* |
| Thickness | *0.15 mm* | *0.15 mm* | *0.2 ~ mm* |
| Critical current | *580 A at 77 K, 0 T* | *380 Aat 77 K, 0 T* | *400 A at 77 K, 0 T* |
| cost | *65.000 won/m* | *60,000 won/m* | *109,000 won/m* |

At the temperature of the liquid nitrogen the performance of the tape are not adequate for this application, for this reason a conduction cooling system is considered. The main difference is the dependence of the critical current by the angle of the magnetic field on the tape.

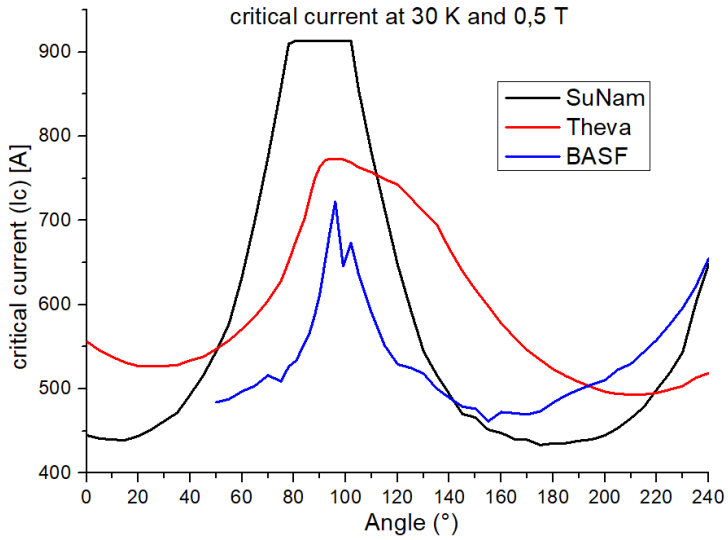


Fig. 5.16. Angle dependent critical current of tape at 30 K and 0,5 T

As shown in Fig. 5.16 the critical current with the external field created by the considered coil of 0.5 T can be affected by great variations according to the direction of the field; the angle considered is the one created by the perpendicular direction of the tape and the direction of the magnetic field lines. The SuNam tape's critical current varies between 430 A to 920 A with its peak at 90°, the Theva tape from 490 A to 780 A and the BASF tape from 480 A to 720 A with their peak at 100°. In order to choose the tape for this application a map of the magnetic field is used to calculate consequently a map of critical current distribution on the cross section of the magnet. In particular, three most emblematic points are considered:

- *point 1*, in the inner surface of the coil at the middle plane perpendicular to the axis of the coil;
- *point 2*, in the inner surface of the coil at the top plane;
- *point 3*, in the medium radius at top plane.

Table 5.7.
CRITICAL CURRENT FOR DIFFERENT POINTS ON THE COIL

| | **SuNAM** | **BASF** | **Theva** |
|---|---|---|---|
| Point 1 | 441.59 A | 482.62 A | 553,11 A |
| Point 2 | 581.36 A | 622.22 A | 549,06 A |
| Point 3 | 887.76 A | 698.8 A | 658,39 A |

As reported in Table 5.7 the point of highest magnetic field is located at the inner surface of the solenoid on the middle plane and also the most critical condition. The critical current

profiles are reduced by 75% to consider a safety margin. Only the Theva tape satisfyes the requirement of current.

## 5.9 Electric Model

The transient event of fault produces a voltage surge of 1500 V on the SC winding terminals; this variation occurs on a time scale of the microsecond. Due to this impulse, the electric potential is not linearly distributed along the turns of the magnet. The uneven distribution of electric potential can provoke transient turn-to-turn over-tensions which are crucial point during the design phase [62]. The accurate evaluation of impulsive voltage distribution in the winding can be obtained by means of a lumped parameters model of the system. The equivalent electric circuit is made of the inductances, which represent the turns mutually coupled, the capacitance corresponding to the insulation layers in between turns and pancakes The detailed model of the coil can be considered taking into account every single inductance and capacitance, such as:

- auto-inductance of each turn;
- mutual inductance of each pair of turns;
- capacitance between each pair of consecutive turns;
- capacitance between each turn and the ground.

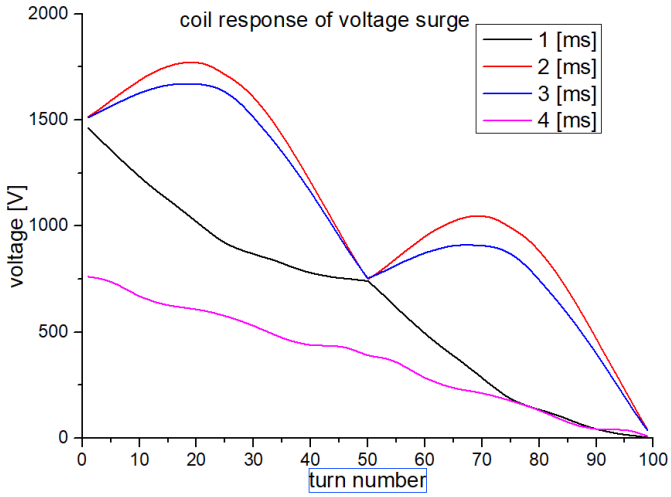


Fig. 5.17. Voltage distribution on the turns at different times

In Fig. 5.17 is shown how the fast transient produces an electric potential distribution where the voltage drop is concentrated in the first 15 turns. In particular in fig a) is reported the electric potential distribution of 100 turns in a DPC at different instants and in fig b) the time distribution of electric potential in different turns. This behavior is due to the effect of the non-linear components of the circuit which gradually decreases. Indeed, at 4 ms, the

voltage drop is evenly distributed. During the fault an voltage over load on the first turns can produce a break in the voltage. Known the electric potential on each turn, a 2-D finite element model is used to evaluate the electrical field, where the electric potential previously obtained is applied to the turns. The distance between the turns is defined by the thickness of the insulation of 0.25 mm. According to the result of the FEM analysis the maximum value of electrical field of the insulation is 1,59 kV. This value is below the breakdown strength of the common type of insulations reported in Table 5.8

Table 5.8.
CHARACTERISTICS OF COMMON INSULATIONS

| **material** | **Electrical performance of common films at low temperature** | | |
|---|---|---|---|
| | **Permittivity** | **Breakdown strength [kV]** | |
| kapton | ***3,1*** | *15* | - |
| paper | ***4,2*** | *7* | *7,5* |
| Mylar | ***2,5*** | *10,3* | *16* |
| Teflon | ***2,3*** | *8* | - |

## 5.10 Thermal Balance

The design of the cooling system with cryostat and thermal shield for HTS magnet is discussed in this section. The heat-transfer analysis using a FEM tool and equivalent circuit is performed. As shown in figure, a double stage GM cryo-cooler is installed on the cryostat and the magnet is equipped with a thermal shield with warm bore, in addition, the metal current leads are connected to the current terminal of the magnet and copper braids are used to thermally connect the magnet to the second stage of the cryo-cooler. The Fig. 5.18 represents the real system with magnet, thermal shield and cryostat sectioned; also the cooling system is shown with optimized current leads, and supports of the thermal shield.

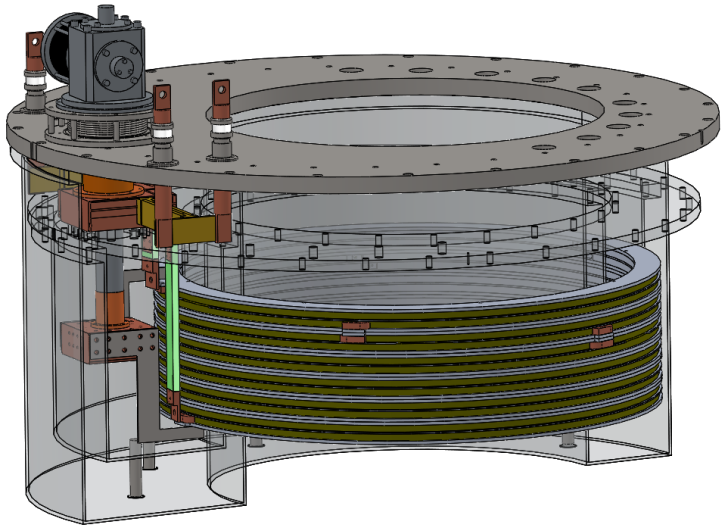

Fig. 5.18. View of SC coil, cryostat and cooling system

The main aim of the thermal analysis is the thermal design of the cryo-cooler with the evaluation of the heat exchanged by the different components. For the first estimation of thermal powers and temperature, an equivalent thermal circuit is used as described in section 4.2, where a similar approach is used for the thermal design of the SMES coil. . In this circuit the node potentials are:

- first stage of cryo-cooler (T1);
- second stage of cryo-cooler (T2);
- HTS magnet (T3);

And the currents in the branches are:

- Cooling power of first stage of cryocooler;
- Cooling power of second stage of cryo–cooler;
- Conduction heat from magnet to second stage;
- Radiation from thermal shield to magnet;
- radiation from external cryostat and thermal shield;

- Current lead heat generation;

In particular, the temperature of the stages of the cryo-cooler are function of the thermal power extracted T1=f(Q1,Q2) e T2=f(Q1,Q2) according to the characteristic map of the cryo-cooler reported in Fig. 5.19. The thermal power on the current lead is evaluated according to the law of Wiedmann-Franz-Lorenz. In this case the current lead geometry and material is optimized in order to minimize the power losses. A comparison between the results from the MATLAB equivalent thermal circuit and FEM thermal analysis is reported in Table 5.9.

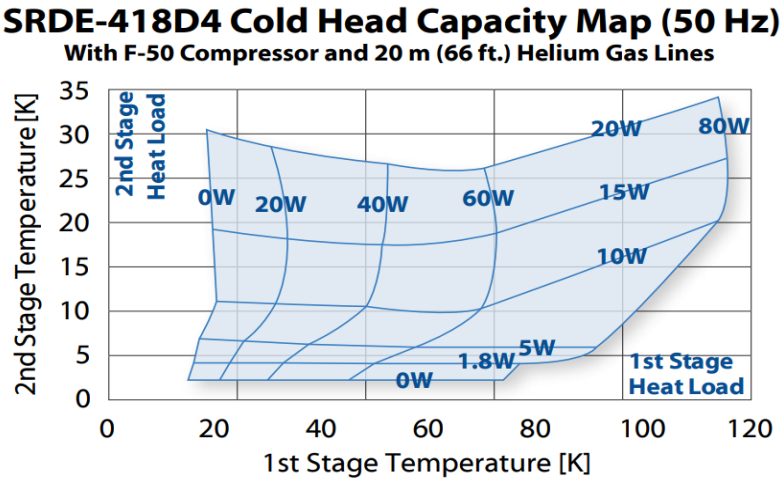


Fig. 5.19. Characteristic map of cryo-cooler

Table 5.9.
COMPARISON OF HEAT LOADS

| | **MATLAB** | **FEM analysis** |
|---|---|---|
| $1^{ST}$ stage cryocooler temperature [*K*] | *94.51* | *102* |
| $2^{ST}$ stage cryocooler temperature [K] | *27.69* | *30* |
| Magnet temperature [K] | *30,27* | *32* |
| Current lead heat load [*W*] | *44* | *44* |
| $1^{ST}$ stage cryocooler Power [*W*] | *62,6* | *69* |
| Radiation from thermal shield to magnet [W] | *0,1* | *0,15* |
| Radiation from cryostat to thermal shield [W] | ***17*** | ***19*** |
| additional Heating power [W] | ***20*** | ***20*** |

With the magnet at 30 K and the value of the current which fixes the heat load generated by the current lead, according to the thermal balance an additional heating power is needed

on the I stage of the cryo-cooler to maintain the operative condition required. The results present a good match in the two different approaches in which the high value of radiation from room temperature to the thermal shield emerges. Especially in FEM analysis this effect is pointed out by the temperature distribution on the thermal shield shown in Fig. 5.20; the temperature on the most distant part of the thermal shield from the cryo-cooler reach the temperature of 127 K. in this case a low value of emissivity is need to reduce the negative effect of the worm bore on thermal the thermal emissivity of the polished aluminum considered is set to 0.018. the accuracy of the analysis also is dependent on the thermal conductivities of the materials used in the magnet assembly.

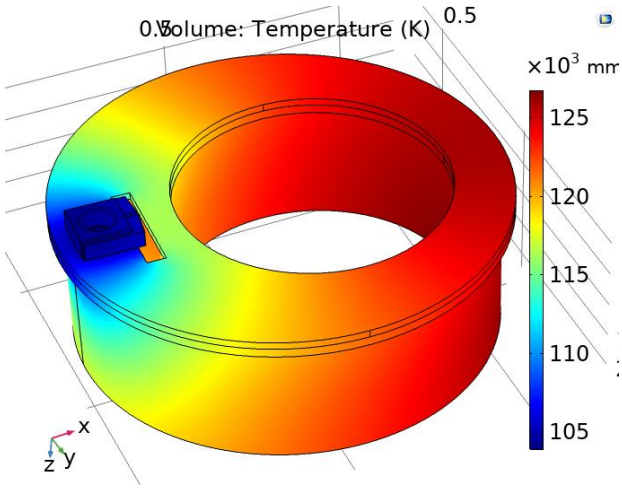


Fig. 5.20. Temperature distribution on the thermal shield

## 5.11 Mechanical Analysis

the stress due to the mechanical load affects the efficiency of the superconductor. For a correct mechanical analysis three phenomena are considered:

- *Pretensioning* due to the process of winding of the tape on the mandrel;
- *thermal contraction* due to the cool-down from the room temperature to the operative temperature;
- *Electromagnetic stress* due to Lorenz forces when the coil is charged to its full power.

As previously introduced, the coli is made of 6 DPC with 70 turns each. The mechanical support of the tape is represented by an aluminum bobbin and the space between each turn is filled by the layer of insulation. The purpose of this section is to evaluate the stress distribution on the coil to verify that the maximum value is below the allowable stress on the superconductor. The analytic evaluation is used as preliminary analysis, then confirmed by numerical results. Once the mechanical properties of material are known, the winding

cool-down, and electromagnetic charging stress are than calculated and compared to the analytical methods described by Arp [28] and Caldwell [30] In Fig. 5.21 are shown the tension stress in the circumferential direction along the longitudinal direction of the tape due to the winding process; the difference between the two model is due to the incapability of the analytic model to evaluate the change of mechanical properties at the boundary with the mandrel. Therefore, in the numerical result the stress corresponds to the pretension applied by the winding machine on the tape of 5 MPa, decreasing towards the mandrel.

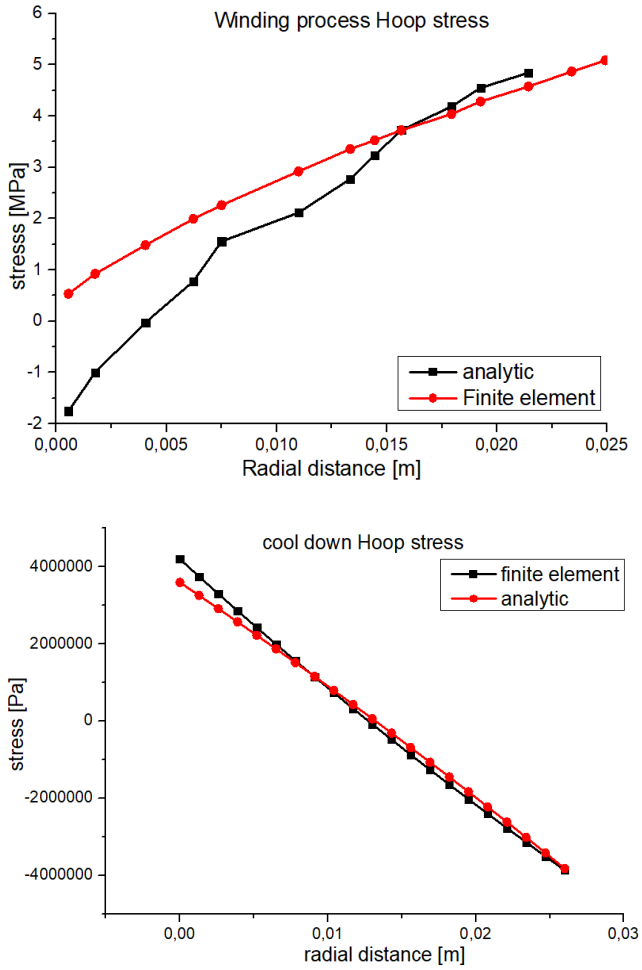


Fig. 5.21. Hoop stress comparison a) winding process b) cool down

The result comparison for the radial distribution of hoop stress due to the cool-down presents a good matching with a maximum value of hoop stress of 4 MPa as shown in fig. the FEM results are obtained via 2D thermo-mechanical analysis of the cooling down transient from 300 K to 30 K. In this phase, the contraction of the coil caused by the cooling process is not allowed by the structural component (mandrel, thermal shield) with different coefficient of thermal expansion, so that the deformation is converted into stress. In Fig. 5.22 is reported the radial distribution of all the contributes for the mechanical stress; the lorentz force are evaluated on the middle plane of the solenoid where the magnitude of

magnetic field is higher. The maximum value of hoop stress of 15 MPa is located on the first layer. The maximum stress is well below the 250 MPa failure stress limit of the tape to provide a safety margin.

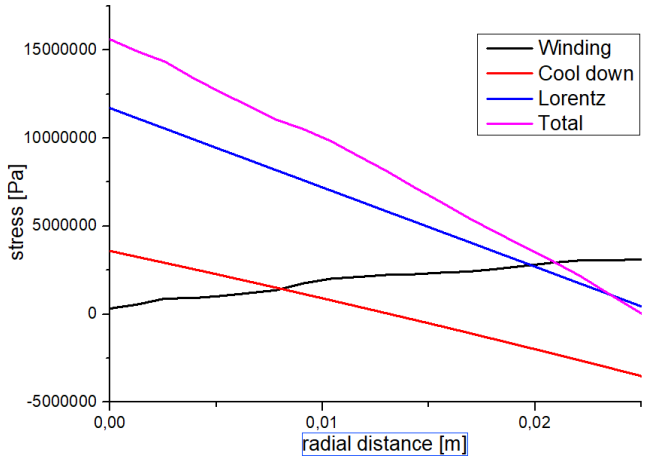


Fig. 5.22. Radial distribution of total stress

A support for the secondary coil is analyzed in order to point out electro-magnetic and thermal effect . During the fault the rapid variation of magnetic field in the bore causes a pulsing Lorentz force on the thermal shield, the components of the resultant in three direction of this force are shown in Fig. 5.23.

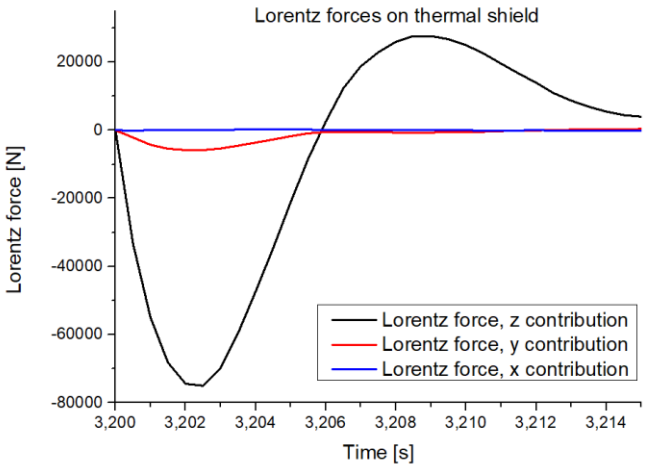


Fig. 5.23. Magnetic force on thermal shield

The GPFR supports, in this case need to be :

- Thermal insulating to prevent heat flux from external case to thermal shield
- With high compressive strength in order to stand the Lorentz force and weight

As shown in the support bars can share the weight and the forces generated equally, within the compressive strength value.

Table 5.10
CHARACTERISTICS OF SUPPORT BARS

| **Item** | **Value** |
|---|---|
| Total force in axial direction | 75 [kN] |
| weight (magnet + term. Shield) | 4,5 [kN] |
| Number of supports | 10 |
| Cross section of support | 25 [mm] |
| Compressive strength GPRF | 349 [Mpa] |
| Max pressure on each support | 15,9 [Mpa] |

## 5.12 Conclusion

To investigate to viability of the SI-SFCL conceptual design of the superconducting magnet were completed. Using optimization techniques, a magnet coil geometry was found. A theva YBCO HTS tape is chosen. A numerical model of the lumped parameter electrical circuit of the coil is developed to evaluate the voltage distribution along the length of the tape. A conduction cooling system was designed around the coil geometries and uses copper straps to transfer heat from the coil windings to a two stage cryocooler. A detailed 3D model of the cryocooler, copper conduction path, superinsulation, and vacuum vessel was used to calculate the heat load due to thermal radiation. It was concluded that the heat load from the thermal radiation is expected to be 20W at the first stage of the cryocooler and 0.4W at the second stage.

The temperature gradient within the coil is expected to be less than 2 K and in the thermal shield 25 K. An estimation of the total heat load (including heat loss from mechanical supports, charging leads, and instrumentation) is 58W at the first stage and 0.6W at the second stage. The initial results suggest that conduction cooling of the HTS magnet to a temperature of 30 K is available.

Detailed ANSYS simulations of the mechanical stress and strain within the coil bundle during manufacturing, cool down, and energizing were completed. In particular, the focus was on the stress developed within the YBCO tape it is concluded that these magnet designs could operate under normal conditions without mechanical failure. Among these include the design of a mechanical support system to handle the large magnetic forces on the coil bundle while at the same time minimizing the heat leak through the support structures. With a more complete mechanical support system developed, the heat loads and temperature profiles can be calculated with more accuracy.

# 6 General Conclusion

In this thesis two different applications of superconductor technology have been investigated. Superconducting magnetic energy storage system (SMES) and superconducting fault current limiter (SFCL) have been studied.

The complete design method has been discussed in detail. The developed design method has been applied to the design of an industrial scale conduction cooled SMES system. Commercially available superconductor magnesium diboride (MgB2) tapes have been considered for the design of the magnet. AC loss of the magnets has been evaluated and the required materials for each case have been calculated. Also, the cooling power requirement of each case and round trip efficiency of the SMES system has been evaluated. The SMES system and the medium voltage power system have been simulated in Matlab/Simulink. Because of the high forces involved it is necessary to impregnate the coil with epoxy resin. However, the differential thermal contraction may easily lead to additional strain on cable causing degradation of critical current. For this reason, the solution adopted is a fiber glass insulation layer in between each pair of conductor layers. When the coil is impregnated the cable is surrounded with polyester layer provided my the producer and the fiber glass with the same thermal contraction as the coated conductor.

The resulting electrical network for the coil geometry is important to design the electric insulation but can be large comprising several thousands of elements with matrices containing all mutual inductances between all elements. The system was simplified by means of state space model than solved in MTALAB.

In order to define the cooling power and the number of cryo-coolers needed, a thermal analysis was developed considering steady and transient thermal power contributions. All the components for the fila design were defined from the thermal shields to the cooper braids used to connect the cryo-coolers to the system. Particular attention was dedicated to evaluating the AC losses using the numerical model THELMA developed at the University of Bologna. In the model the longitudinal distribution of the current in the filaments and the transverse current in the matrix between filaments was calculated. The heat generation produced by the non-uniformity of the current distribution during transient was added to the thermal balance to define the temperature rise for each charge/discharge cycle.

In order to study the coil in detail in term of magnetization, normal zone propagation and stability it was necessary to develop a numerical model. A electro-magnetic and thermal network model was developed. In ANSYS APDL. The current and the magnetic field density in nodes and elements of the finite element domain are obtained and coupled with thermal physics.

# References


[1] P. F. Schewe et al., The grid: A journey through the heart of our electrified world, Washington, 2007.

[2] A. P. Malozemoff et al., Second-generation high-temperature superconductor wires for the electric power grid, Palo Alto, 2012.

[3] N. Amemiya et al., «AC loss reduction of YBCO coated conductors by multifilamentary structure.,» *Superconductor Science and Technology,* vol. 17, pp. 1464-1471, 2004.

[4] M. Iwakuma et al., «Development of a rebco superconducting transformer with current limiting function,» *IEEE Transactions on Applied Superconductivity,* vol. 21, n. 3, pp. 1405-1408, 2011.

[5] L. S. Lakshmi et al., «Magnetic and transport AC losses in HTS Roebel cable,» *IEEE Transactions on Applied Superconductivity,* vol. 21, n. 3, pp. 3311-3315, 2011.

[6] S. Kalsi et al., «discussion of test results of a superconductor synchronous condenser on a utility grid,» *IEEE Transactions on Applied Superconductivity,* vol. 17, n. 2, pp. 2026-2029, 2007.

[7] D. S. Johnson et al., «Circuit breakers,» in *Standard handbook for electrical engineers*, 1993.

[8] P. Tixador et al., «Superconducting magnetic energy storage: Status and perspective,» *IEEE/CSC & ESAS European Superconductivity News Forum.*, 2008.

[9] M. H. Ali et al., «An overview of SMES applications in power and energy systems,» *IEEE Transactions on Sustainable Energy,* vol. 1, n. 1, pp. 38-47, 2010.

[10] L. Chen et al., «Conceptual Design and Evaluation of an HTS Magnet for an SMES Used in Improving Transient Performance of a Grid-Connected PV System,» *IEEE Transactions on Applied Superconductivity,* vol. 28, n. 3, p. 1–8, 2018.

[11] T. Baig et al., «Conceptual designs of conduction cooled MgB 2 magnets for 1.5 and 3.0 T full body MRI systems,» *Superconductor Science and Technology,* vol. 30, n. 4, pp. 43-45, 2017.

[12] S. L. Bud'ko et al., «Boron Isotope Effect in Superconducting $MgB_2$,» *Physical review letters,* vol. 86, n. 9, 2001.

[13] P. Kovac et al., «Behaviour of filamentary $MgB_2$ wires subjected to tensile stress at 4.2 K,» *superconductor science and technology,* vol. 26, n. 10, 2013

References

[14] M. Watanabe et al., «A Study on High Temperature Superconducting Coil of Different Coil Arrangements,» *IEEE Transactions on Applied Superconductivity,* vol. 17, n. 2, 2002

[15] W. Hassenzahl et al., «A comparison of the conductor requirements for energy storage devices made with ideal coil geometries,» *IEEE Transactions on Magnetics,* vol. 25, n. 2, p. 1799–1802, 1989.

[16] B. P. Raju et al., «A current limiting device using superconducting D.C. bias applications and prospects,» *IEEE trans. Power Appar. Syst.,* vol. 101, n. 9, pp. 3173-3177, 1982

[17] L. S. Abdullah Al Amin et al., «Computational homogenization of the elastic and thermal properties of superconducting composite $MgB_2$ wire,» *Composite Structures,* vol. 188, pp. 313-329, 2018.

[18] L. bottura, «cable stability» arXiv:1412.5373.

[19] D. Lieurance et al., «Design and cost studies for small scale superconducting magnetic energy storage (SMES) systems,» *IEEE Transactions on Appiled Superconductivity,* vol. 5, n. 2, pp. 350-353, 1995.

[20] A. B. Aesoy et al., «Transient Modeling and Simulation of a SMES Coil and the Power Electronics Interface,» *IEEE transactions in applied superconductivity,* vol. 9, n. 4, 1999.

[21] L. Botong et al., «Current-limiting characteristics of saturated iron-core fault current limiters in VSC-HVDC systems based on electromagnetic energy conversion mechanism,» *J. Mod. Power Syst. Clean Energy,* vol. 7, n. 2, pp. 412-421, 2019.

[22] J. Bock et al., «Resistive superconducting fault current limiters are becoming a mature technology,» *IEEE Trans. Appl. Supercond.,* vol. 23, n. 3, june 2015.

[23] L. Chen et al., «Detailed Modeling of Superconducting Magnetic Energy Storage (SMES) System,» *IEEE Transactions on Power Delivery,* vol. 21, n. 2, pp. 699-710, 2006.

[24] C. Poole et al., «Numerical study on the quench propagation in a 1.5 T MgB 2 MRI magnet design with varied wire compositions,» *Superconductor Science and Technology,* vol. 29, n. 4, pp. 44-47, 2016.

[25] M. Guan et al., «Structural mechanics exploration for multicomponent superconducting solenoids by Hoop strain tests during cooling and excitation,» *Journal of Superconductivity and Novel Magnetism,* vol. 27, pp. 1179-85, 2013.

[26] E. Luciano et al., «Variational methods for the homogenization of periodic heterogeneous media,» *European journal of mechanics,* vol. 17, n. 4, pp. 599-617, 1998.

[27] K. Tanaka et al., «Fabrication and transport properties of an $MgB_2$ solenoid coil,» *Superconductor Science and Technology,* vol. 18, n. 5, 2005.

[28] V. Arp et al., «Stresses in superconducting solenoids,» *Journal of Applied Physics,* vol. 48, n. 5, pp. 2026-2036, 1977.

[29] L. Li et al., «Preliminary Mechanical Analysis of a 9.4-T Whole-Body MRI Magnet,» *IEEE Transactions on Applied Superconductivity,* vol. 25, n. 2, pp. 1-7, 2015.

[30] J. Caldwell et al., «Electromagnetic forces in high field magnet coils,» *Applied Mathematical modelling,* vol. 6, n. 3, pp. 157-160, 1982.

[31] A. M. Miri et al., «Investigation of the transient behaviour of a superconducting magnetic energy storage (SMES) generating high power pulses,» *European transaction on electrical power,* vol. 8, n. 1, 2007.

[32] Z. Xia et al., «Verification of HTS SMES Lumped Parameter Network Model,» *IEEE Transactions on Applied Superconductivity,* vol. 27, n. 4, pp. 1-5, 2017

[33] S. K. S.V. Kulkarni, «Transformer Engineering - design, technology and diagnostics,» CRC press, 2013, p. chapter 4.

[34] S. V. Kulkarni. e. S. A. Khaparde, «Transformer engineering: design, technology, and diagnostics»

[35] J. Shi et al., «Voltage Distribution Characteristic of HTS SMES Magnet,» *IEEE Transactions on Applied Superconductivity,* vol. 26, n. 4, pp. 1-5, 2016.

[36] W. McNutt, «Response of Transformer Windings to System Transient Voltages,» *IEEE Transactions on Power Apparatus and Systems,* vol. 93, n. 2, pp. 457-467, 1974

[37] P. Huang et al., «Electric Field Simulations and Analysis for High Voltage High Power Medium Frequency Transformer,» *Energies,* vol. 10, n. 3, p. 371, 2017.

[38] M. Breschi, «Electromagnetic modeling of the jacket in cable-in-conduit conductors,» *transaction on applied superconductivity,* vol. 18, n. 1, pp. 18-28, 2008.

[39] M. Ciotti, «THELMA code electromagnetic model of ITER superconducting cables and application to the ENEA stability experiment,» *Superconductor Science and Technology,* vol. 19, n. 10, pp. 987-997, 2006.

[40] E. Kostrova et al., «Performance test of a G-M cooler in magnetic field,» *Physics procedia,* vol. 67, pp. 440-444, 2015.

[41] C. Poole et al., «Numerical study on the quench propagation in a 1.5 T $MgB_2$ MRI magnet design with varied wire,» *Supercond. Sci. Technol.,* vol. 29, n. 4, pp. 44-47, 2016.

[42] P. Bauer, Stability of Superconducting Strands for Accelerator Magnets. PhD thesis, Technical University Vienna, 1996.

[43] G. Willering, Stability of Superconducting Rutherford Cables. PhD thesis, University of Twente Enschede, 2009.

[44] S. Caspi et al., Calculating quench propagation with ANSYS, IEEE Transactions on Applied Superconductivity, 13(2):1714–1717, 2003.

[45] P. P. Granieri, Heat Transfer between the Superconducting Cables of the LHC Accelerator Magnets and the Superfluid Helium Bath. PhD thesis, EPFL Lausanne, 2012.

[46] D. Paudel, Quench Simulation of Superconducting Magnets with Commercial Multi-Physics Software, PhD Thesis, Aalto university, 2015

[47] T. J. Lewis et al., «The transient behaviour of ladder networks of the type representing transformer and machine windings,» *Proceedings of the IEE - Part II: Power Engineering,* vol. 110, n. 83, pp. 541-553, 1954.

[48] A. Hobl et al., «Superconducting fault current limiters—A new tool for the "grid of the future",» in *CIRED 2012 Workshop, Integr. Renewables Into Distrib.*, Lisbon, Portugal, 2012.

[49] A. Morandi, «State of the art of superconducting fault current limiters and their application to the electric power system,» *Physica C, Supercond.,* vol. 484, n. 15, pp. 242-247, jan. 2013.

[50] «CIGRE technical brochure 239/2003 - fault current limiter».

[51] C. Franck et al., «HVDC circuit breakers: A review identifying future,» *IEEE Trans. Power Del,* vol. 26, n. 2, pp. 998-1007, 2001.

[52] Y. Nikulshin, «Saturated Core Fault Current Limiters in a Live Grid,» *IEEE Trans, appl. Supercond.*, vol. 26, n. 3, 2016.

[53] F. Moriconi et al., «Development and deployment of saturated-core fault current limiters in distribution and transmission substations,» *IEEE Trans. Appl. Sup,* vol. 21, 2011.

[54] Y. Xin et al., «Performance of the 35 kV/90 MV A SFCL in live-grid fault current limiting tests,» *IEEE Trans. Appl. Sup.,* vol. 21, n. 3, pp. 1294-1297, 2011.

[55] A. Morandi et al., «Coupled Electromagnetic-Thermal Model and Equivalent Circuit of a Magnetic Shield Type SFCL,» *IEEE trans. appl. supercond.,* vol. 23, n. 3, 2013.

[56] F. Langford-Smith et al., in *Radiotron Designer's Handbook*, Radio Corporation of America, 1953, pp. 233-235.

[57] L. Chen et al., «Comparison of Inductive and Resistive SFCL to Robustness Improvement of a VSC-HVDC System With Wind Plants Against DC Fault,» *IEEE trans. appl. supercond.,* vol. 26, n. 7, 2016.

[58] A. Morandi, «Superconducting transformers: key design aspects for power applications,» *Journal of Physics*, 2008.

[59] G. F. Mechler et al., «Calculation of spatial loss distribution in stacked power and distribution transformer cores,» *IEEE trans. appl. supercond.*, vol. 13, n. 2, pp. 532-537, 1998.

[60] Y. Nikulshin et al., «Saturated Core Fault Current Limiters in a Live Grid,» *IEEE Transactions on Applied Superconductivity*, vol. 26, n. 3, p. 1, april 2016.

[61] «http://htsdb.wimbush.eu/,» [Online].

[62] J. Caldwell et al., «Electromagnetic forces in high field magnet coils,» *Appl. Math. Model.*, vol. 6, pp. 157-160, 1982.

[63] B. G. e. M. F. A. Morandi, «Design and performance of a 1 MW-5 s high temperature superconductor magnetic energy storage system».*Superconductor Science and Technology, vol. 29, n. 1, pag. 015014, gen. 2016.*

[64] A. Greenwood, «Electrical Transients in Power Systems».

[65] Y. Iwasa et al., «SUPERCONDUCTING MAGNET TECHNOLOGY».*in Case Studies in Superconducting Magnets, Boston, MA: Springer US, 2009, pagg. 1–24.*

[66] A. Morandi e. al., «The DRYSMES4GRID Project: Development of a 500 kJ/200 kW Cryogen-Free Cooled SMES Demonstrator Based on $MgB_2$».*IEEE Transactions on Applied Superconductivity, vol. 28, n. 4, pagg. 1–5, giu. 2018.*

[67] H. Lee et al., «Feasible application study of several types of superconducting,» *IEEE Trans. Appl. Supercond.*, vol. 28, n. 4, 2018.

[68] V. Arp et al., «stresses in supeconducting solenoids,» *Journal of Applied Physics*, vol. 48, pp. 2026-36, 1977.

[69] A. Zhou et al., «The Supplementary Design Method of HTS SMES System Considering Voltage Distribution Characteristic,» *IEEE Transactions on Applied Superconductivity*, vol. 27, n. 4, pp. 1-5, june 2017.

[70] L. Li et al., «Effect of Pretension, Support Condition, and Cool Down on Mechanical Disturbance of Superconducting Coils,» *IEEE Transactions on Applied Superconductivity*, vol. 22, n. 2, 2012.

[71] S. Lim et al., «Analyses of a solenoid magnet made of pancakes of coated conductors,» *Superconductor Science and Technology*, vol. 18, n. 4, 2005.

References

[72] V. Q. Dao et al., «Conceptual Design of a Saturated Iron-Core Superconducting Fault Current Limiter for a DC Power System,» *IEEE trans. appl. supecond.*, vol. 30, n. 4, 2020

[73] J. Yang et al., «Short-circuit and ground fault analyses and location in VSC-based DC network cables,» *IEEE Trans. Ind. Electron.*, vol. 59, n. 10, p. 3827–3837, 2012.

[74] Y. Shiroyanagi et al., «The Construction and Testing of YBCO Pancake Coils for a High Field Solenoid,» *IEEE Transactions on Applied Superconductivity*, vol. 21, n. 3, pp. 1649-1652, 2011.

[75] M. Fu et al., «Quench characteristics and normal zone propagation of an MgB 2 superconducting coil,» *Superconductor Science and Technology*, vol. 17, n. 1, pp. 160-163, 2004.

[76] M. Ciotti et al., «THELMA code electromagnetic model of ITER superconducting cables and application to the ENEA stability experiment,» *Superconductor Science and Technology*, vol. 19, n. 10, pp. 987-997, 2006.

[77] M. Guan et al., «Magneto-Mechanical Coupling Analysis of a Superconducting Solenoid Magnet in Self-Magnetic Field,» *IEEE Transactions on Applied Superconductivity*, vol. 24, n. 3, pp. 1-4, 2014.

[78] A. Liu et al., «Transient Modeling and Simulation of a SMES Coil and the Power Electronics Interface,» *IEEE transactions on applied superconductivity*, vol. 8, n. 4, p. 10, 1999.

[79] S. W. Sciver et al., «Low-Temperature Materials Properties,» *Helium Cryogenics*, pp. 17-58, 2012.

[80] U. Melaccio, Van Quan Dao, Jae In Lee, Chang-Soon Kim, A. Morandi and Minwon Park, Design of HTS coil of SI-SFCL in a 30 kV/1 kA DC power grid, in preparation

## Appendix 1- executive drawings of SMES magnet

A1.1 Assembly of magnetic and cryogenic system with external case

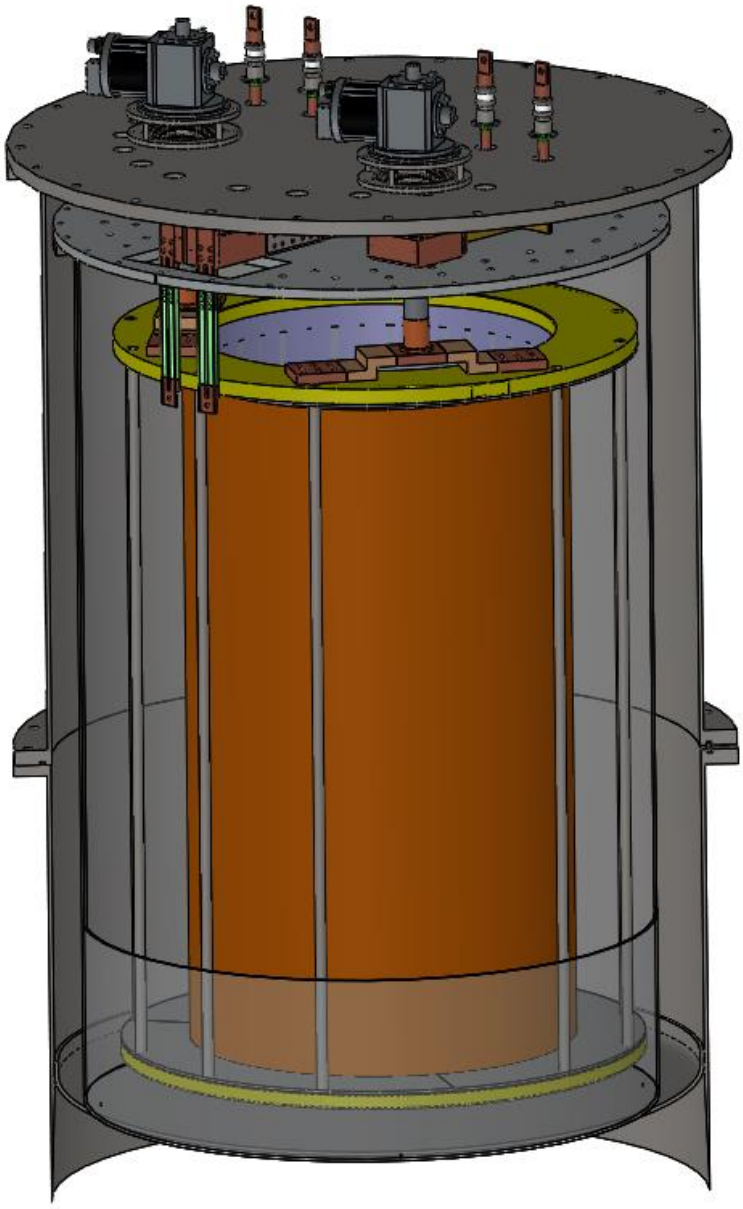

A1.2 Assembly of magnetic and cryogenic system with thermal shield view

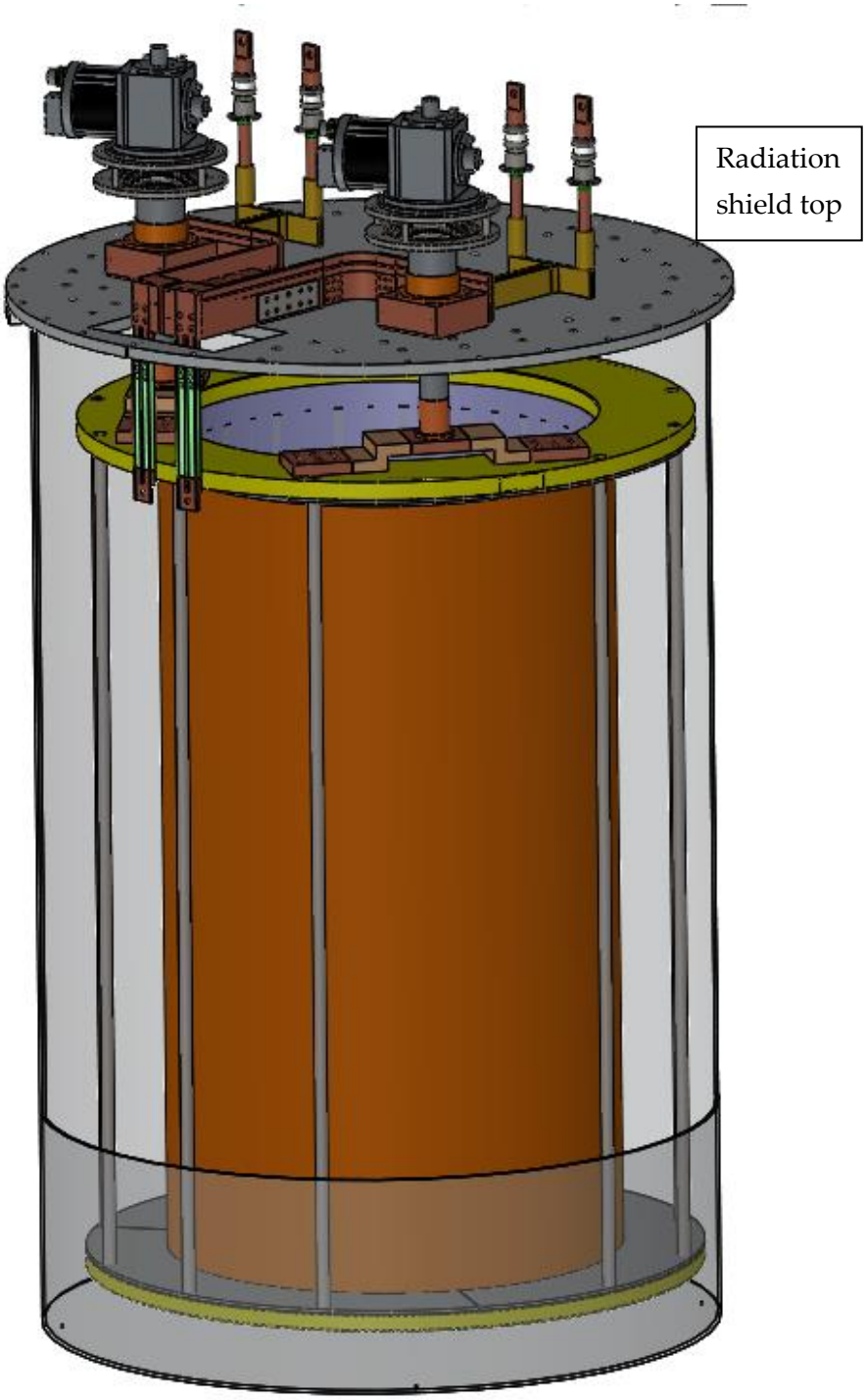

## A1.3 Cryogenic system

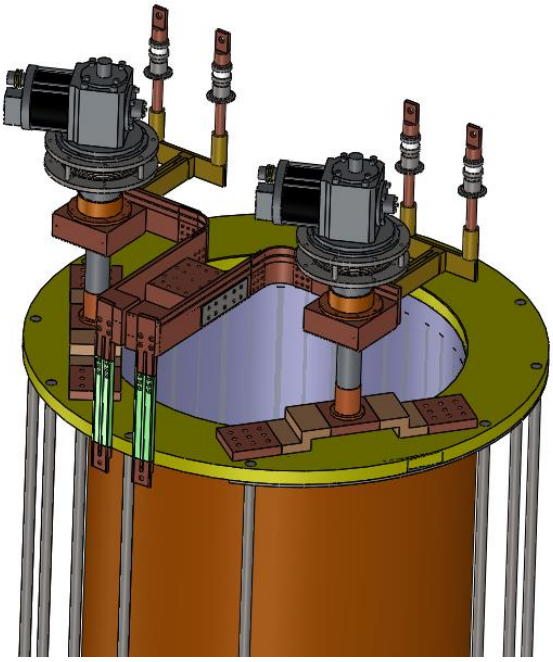

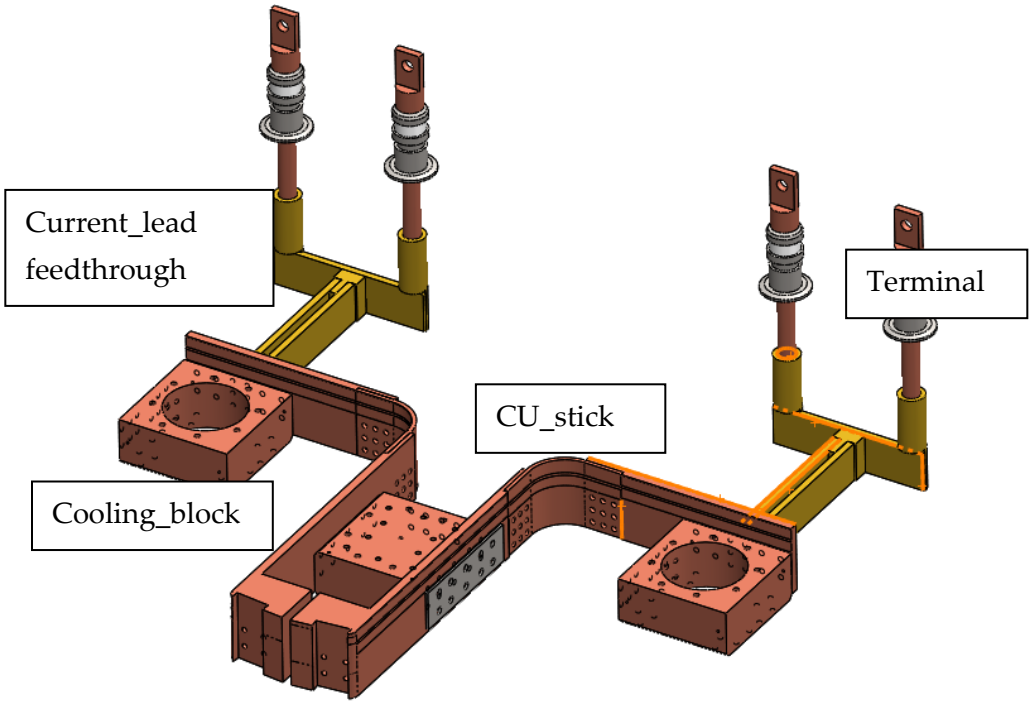

## A1.4 Copper cooling block for cryo-cooler

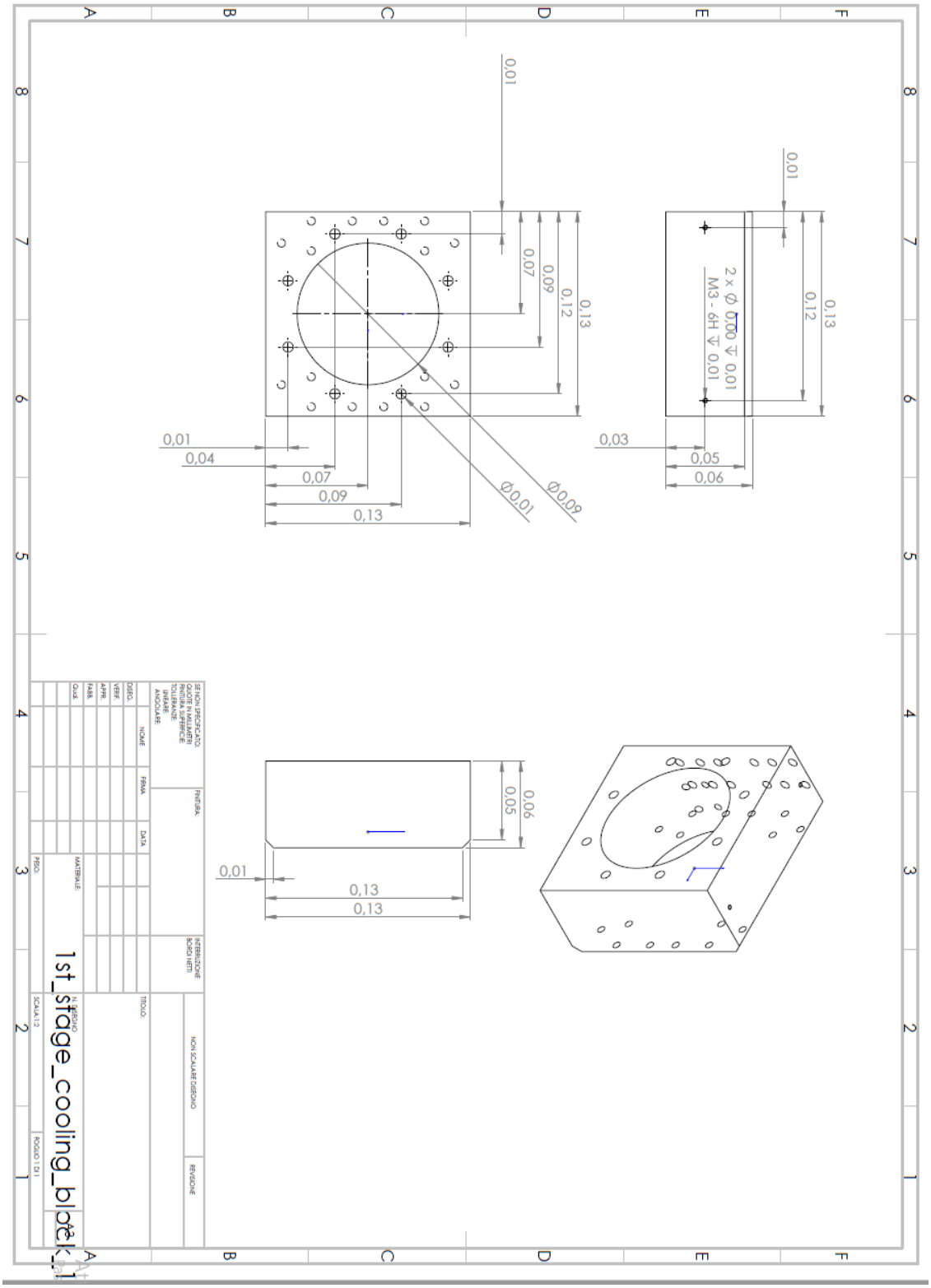

## A1.5 Copper cooling stick for HTS current-lead

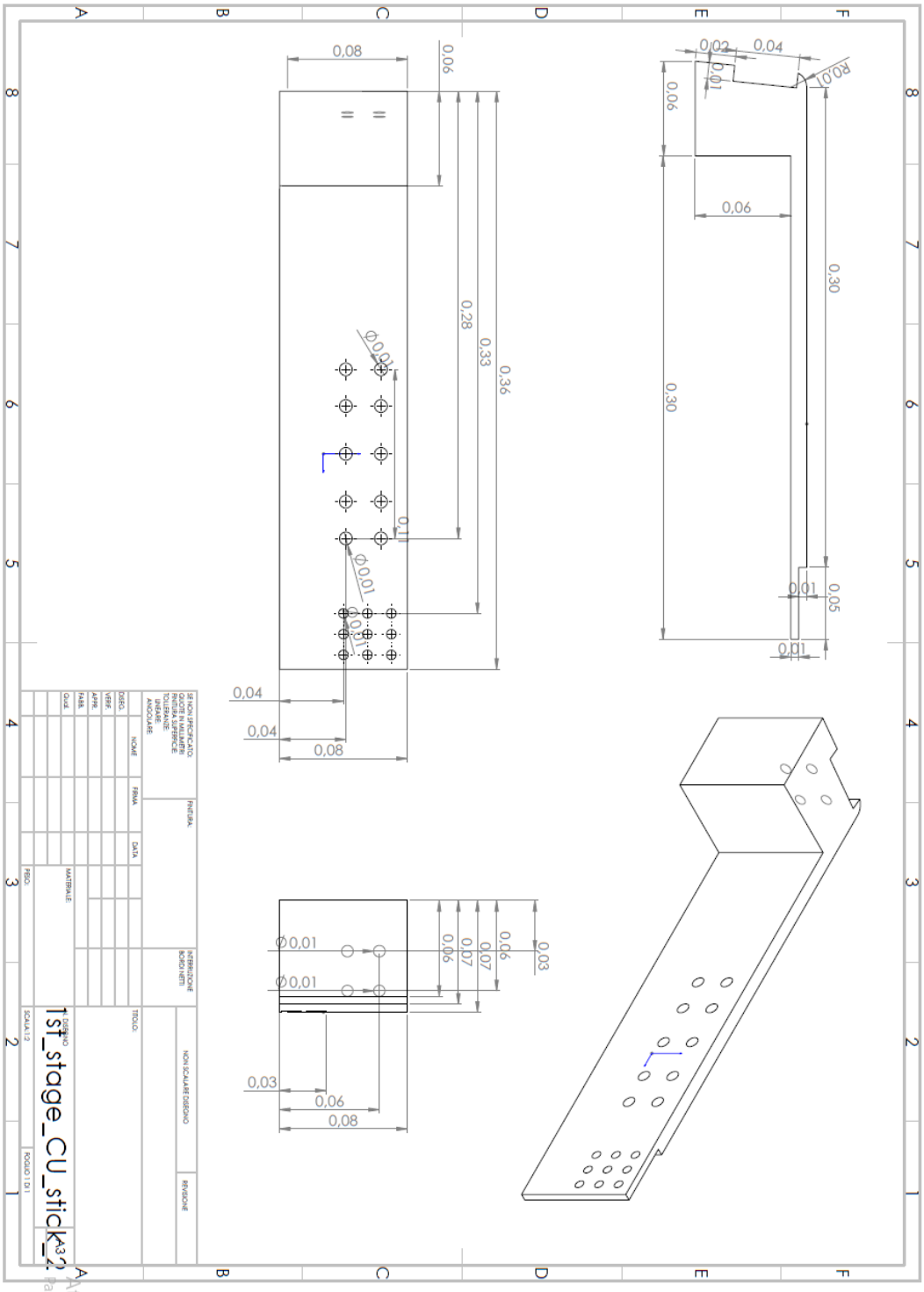

## A1.6 Brass section of the current lead following the terminals

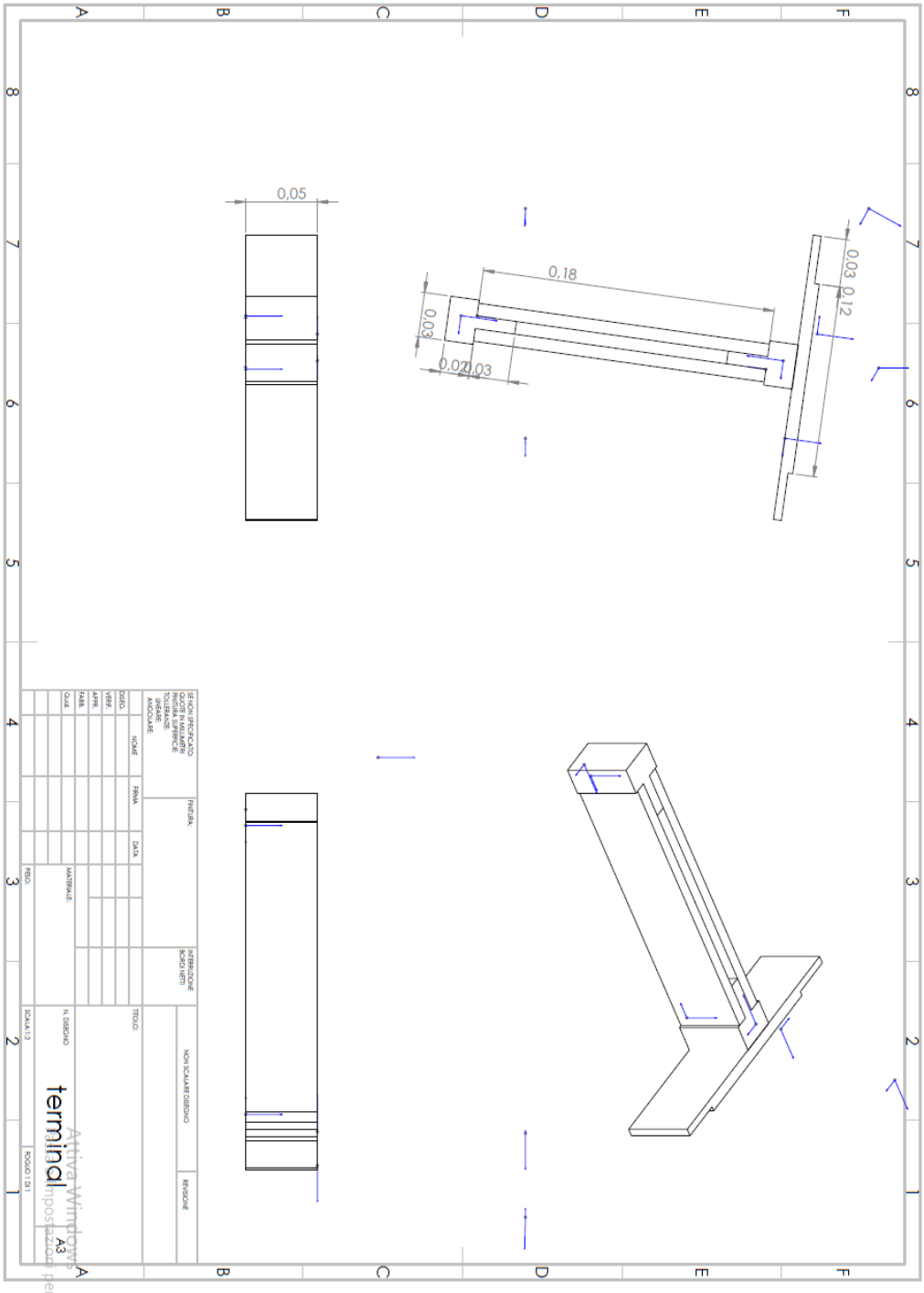

## A1.7 Current input terminals at ambient temperature,

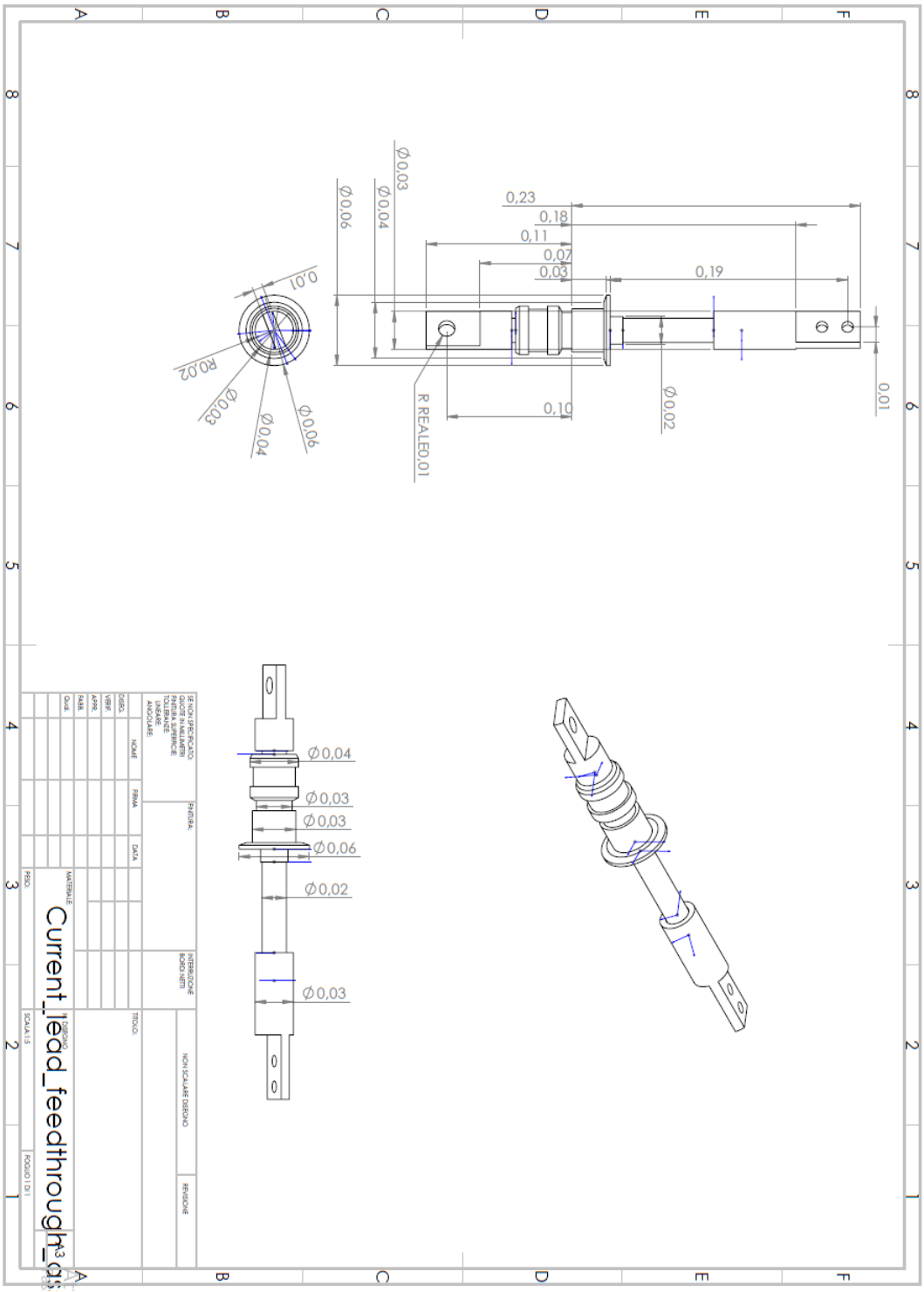

## A1.8 Upper flange with indication of cable and joint housings and holes for tie rods

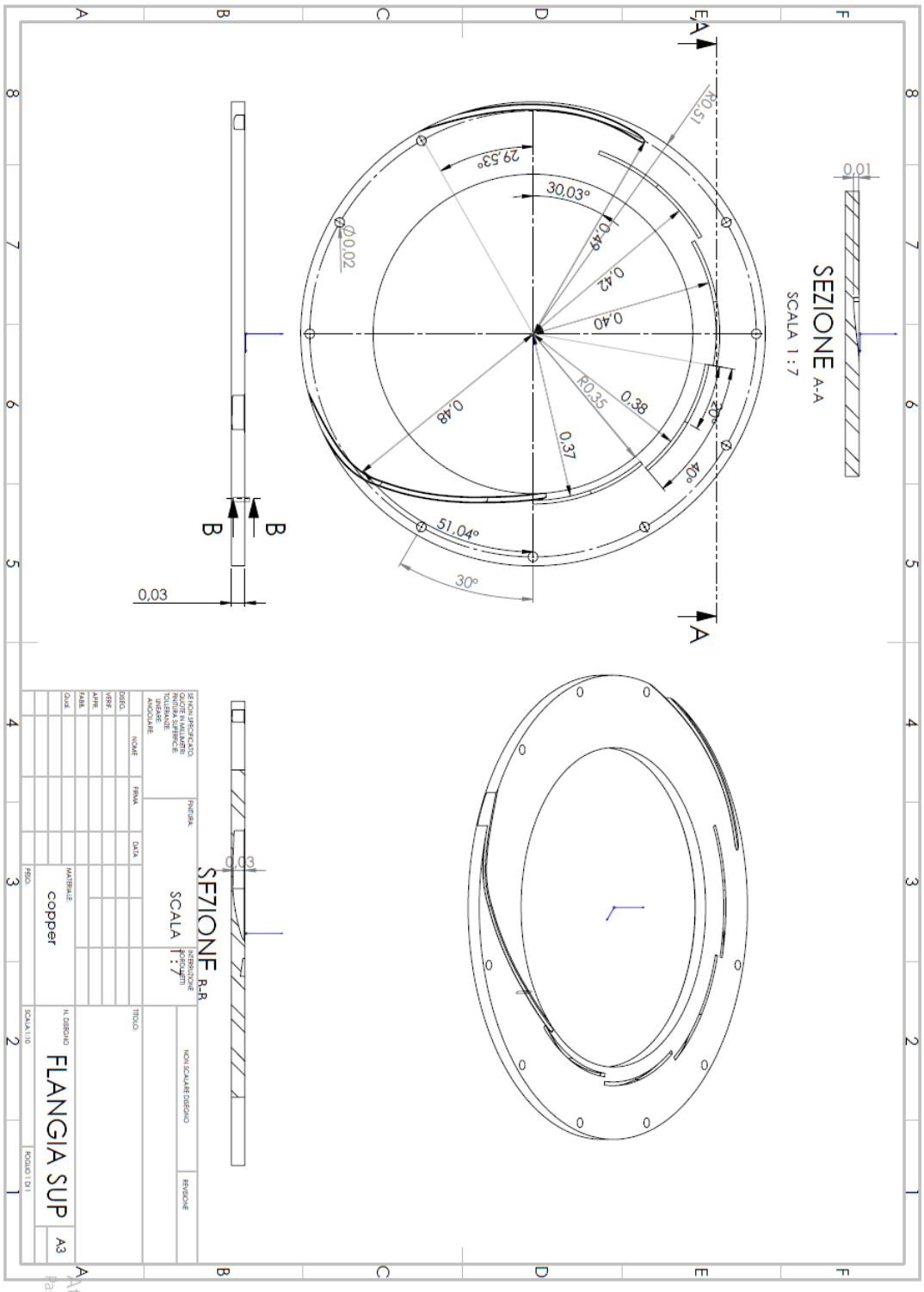

## A1.9 Cover for steel thermal shield with holes for cryocooler and access to the magnet for the current leads

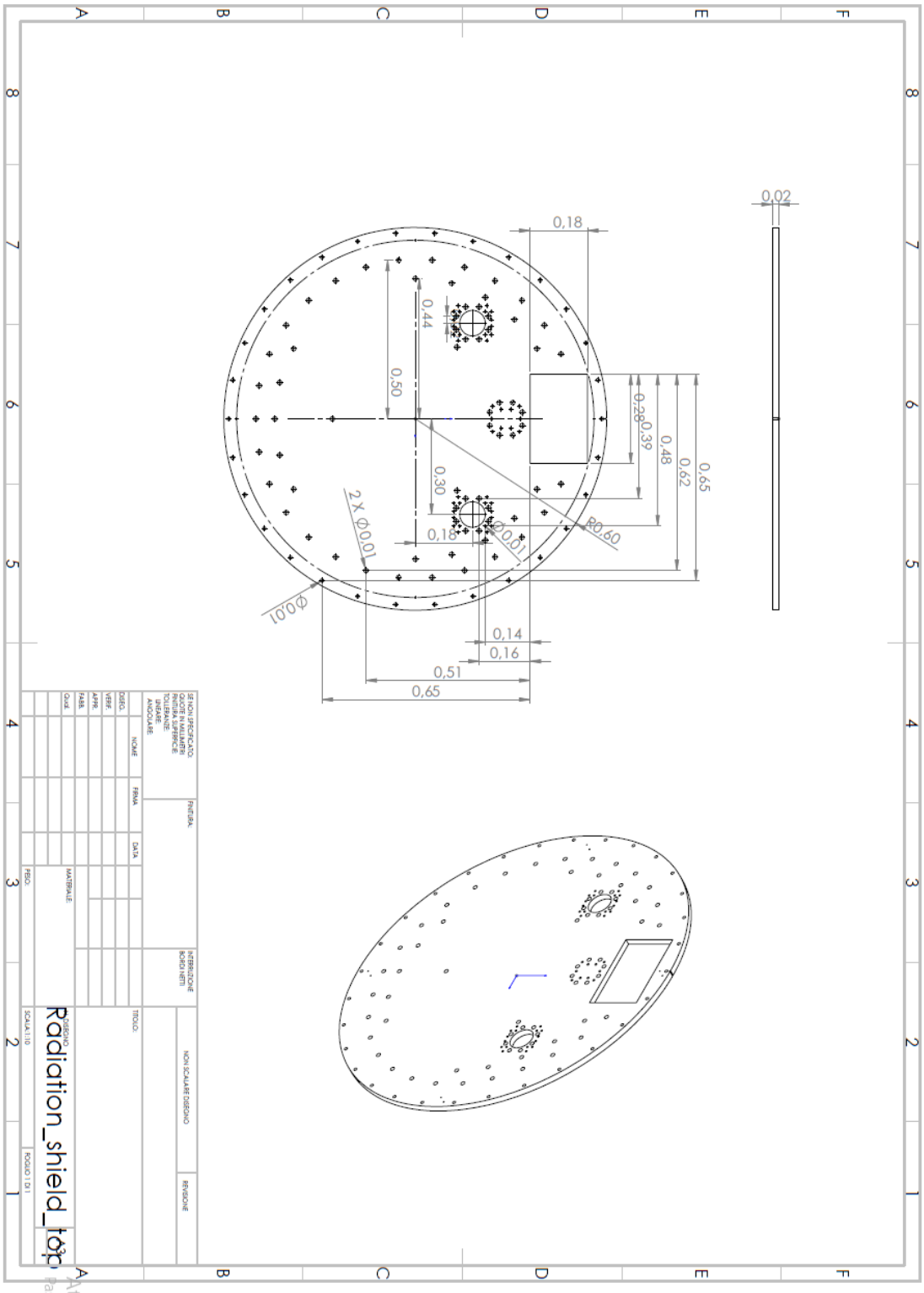

A1.10 External shield cover made of steel with holes for cryocooler

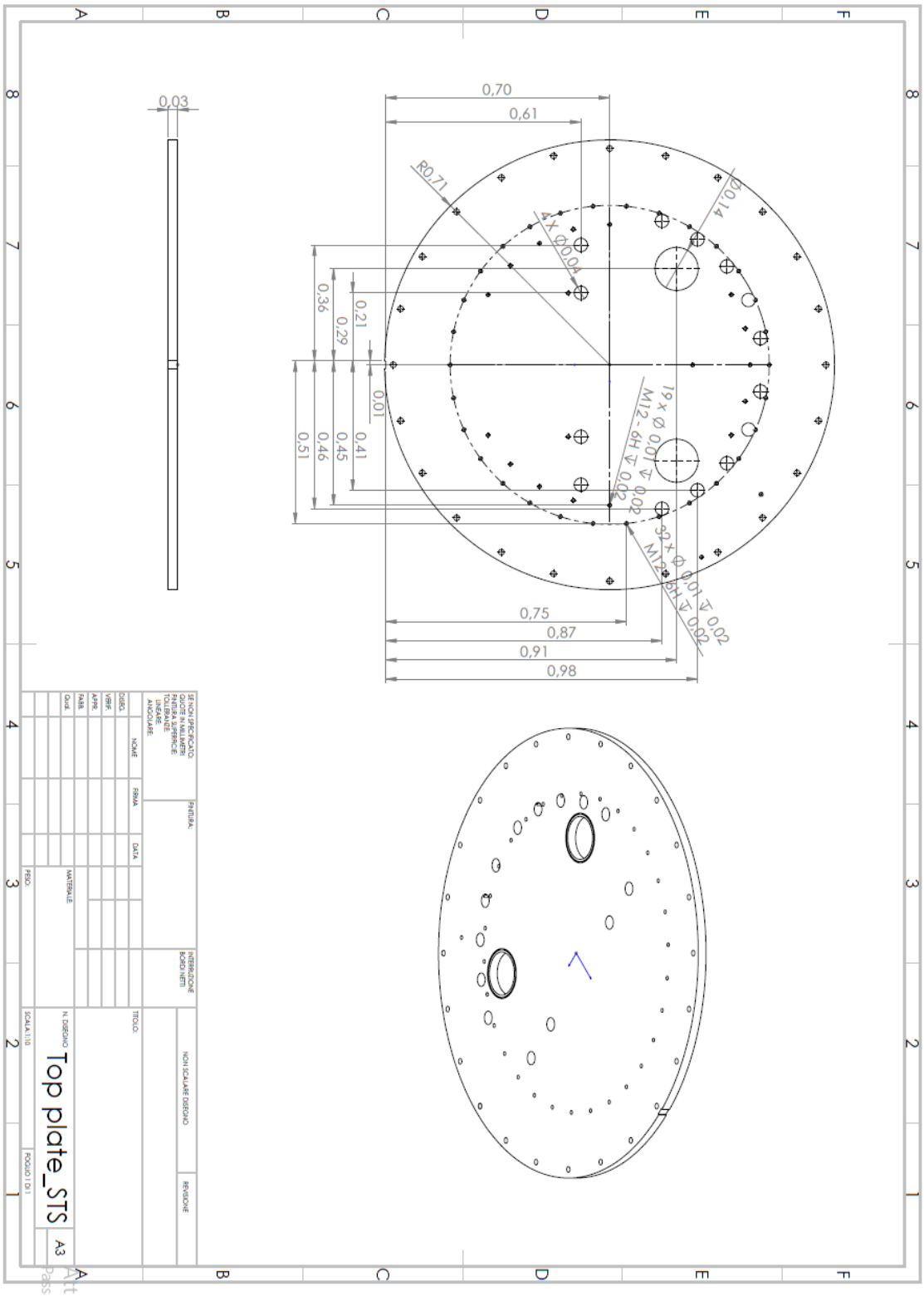

A1.11 Steel support of the cryocoolers on the external cover, consisting of two flanges and a shaped mandrel

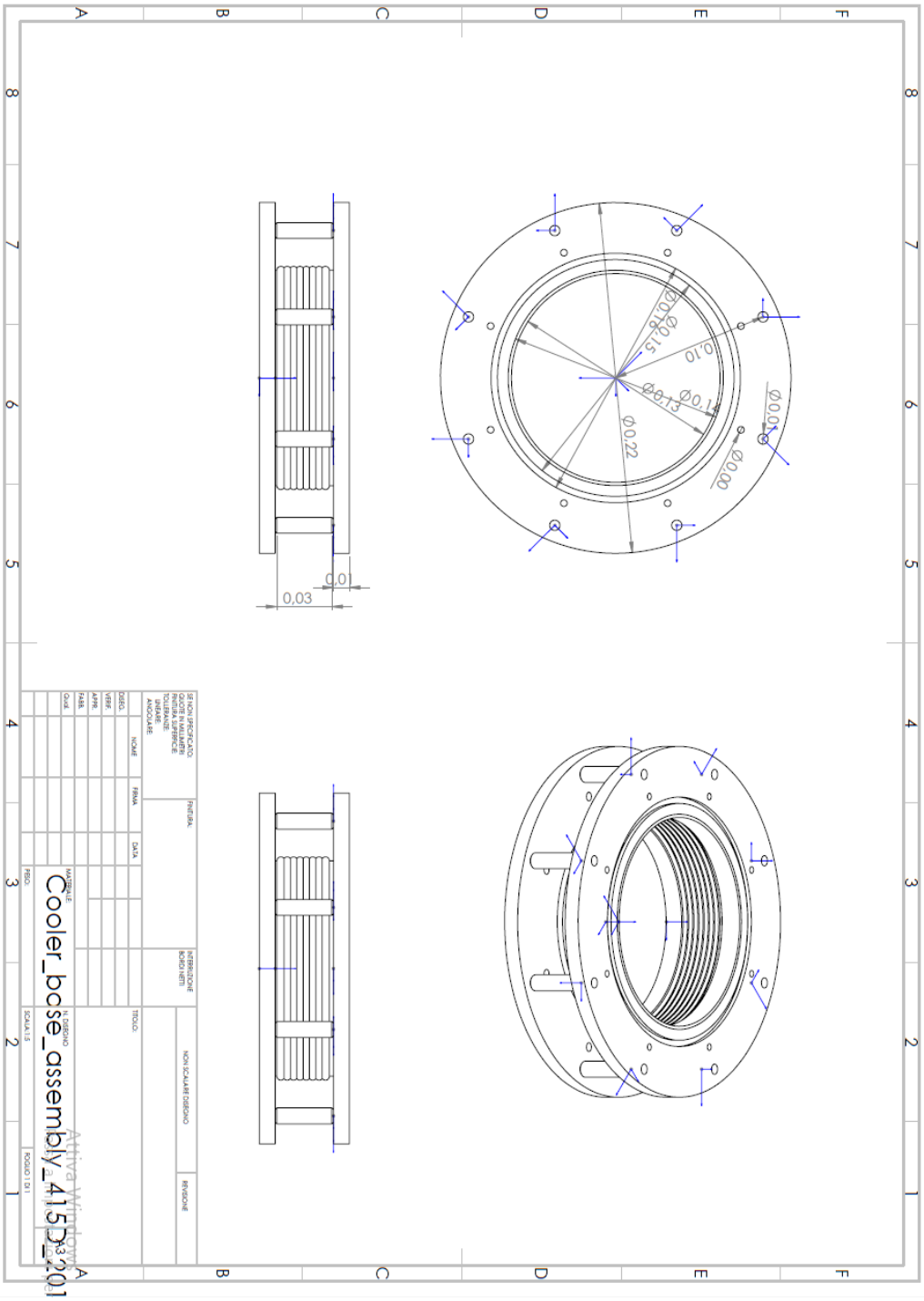

## A1.12 Copper joint